

International Advanced Researches and Engineering Journal

e-ISSN
2618-575X



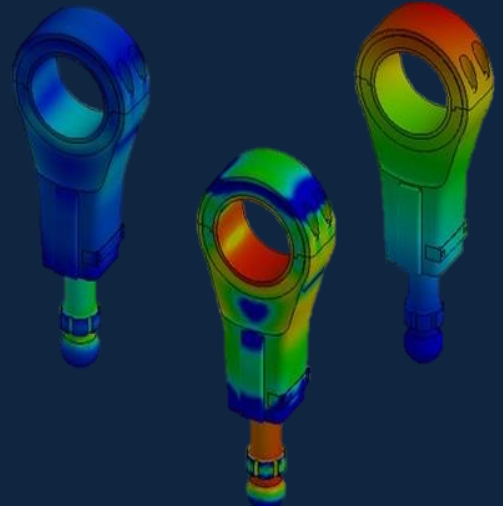
$$F=ma$$

$$E=mc^2$$

$$\int \frac{dy}{dx} dt$$

Volume	Issue
06	03

December, 2022





International Advanced Researches and Engineering Journal (IAREJ) is a double-blind peer-reviewed and publicly available online journal that has Editorial Board (<https://dergipark.org.tr/en/pub/iarej/board>). The editor in chief of IAREJ welcomes the submissions that cover theoretical and/or applied researches on **Engineering** and related science with Engineering. The publication language of the Journal is **English**. **Writing Rules** are given in Author Guidelines (<https://dergipark.org.tr/en/pub/iarej/writing-rules>). IAREJ publishes **original papers** that are research papers and technical review papers.

IAREJ publication, which is **open access**, is **free of charge**. There is no article submission and processing charges (APCs).

IAREJ is indexed & abstracted in:

Crossref (Doi prefix: 10.35860/iarej.)
Directory of Open Access Scholarly Researches (ROAD)
Directory of Research Journals Indexing (DRJI)
EBSCO
Google Scholar
Index Copernicus (ICI Journal Master List)
J-Gate
TUBITAK ULAKBIM TR Dizin (TR index)
WorldCAT

Authors are responsible from the copyrights of the figures and the contents of the manuscripts, accuracy of the references, quotations and proposed ideas and the Publication Ethics (<https://dergipark.org.tr/en/pub/iarej/page/4240>).

International Advanced Researches and Engineering Journal (IAREJ) allows the author(s) to hold the copyright of own articles.

©

IAREJ

15 December 2022



This is an open access issue under the CC BY-NC license (<http://creativecommons.org/licenses/by-nc/4.0/>).



e-ISSN: 2618-575X

Available online at www.dergipark.org.tr/en

INTERNATIONAL ADVANCED RESEARCHES
and
ENGINEERING JOURNAL

Journal homepage: www.dergipark.org.tr/en/pub/iarej

International
Open Access



Volume 06
Issue 03

December, 2022

Table of Contents

Research Articles	Pages
1. Synergistic effect of h-BN on thermal conductivity of polymer composites <i>Nilay KÜÇÜKDOĞAN ÖZTÜRK</i>	161-166
2. Production and characterization of activated carbon from Black Poplar (<i>Populus Nigra</i>) wood waste with different chemical activation methods <i>Mehmet Emin ERGÜN and Saban BULBUL</i>	167-175
3. Effect of baffle angles on flow and heat transfer in a circular duct with nanofluids <i>Selma AKÇAY and Ünal AKDAĞ</i>	176-185
4. Experimental analysis of a transcritical heat pump system with CO2 refrigerant <i>Ahmet ELBİR, Hilmi Cenk BAYRAKÇI, Arif Emre ÖZGÜR and Özdemir DENİZ</i>	186-193
5. A new approach to event- and model-based feature-driven software testing and comparison with similar approaches <i>Fevzi BELLİ, Tuğkan TUĞLULAR and Ekinan UFUKTEPE</i>	194-203
6. Reliability estimation for drone communications by using an MLP-based model <i>A F M Shahen SHAH and Muhammet Ali KARABULUT</i>	204-210
7. Effects of advanced oxidation process on greywater treatment: an optimization study <i>Özlem DEMİR and Ezgi Sühel AKTAŞ</i>	211-219
8. Improved endothelial cell proliferation on laminin-derived peptide conjugated nanofibrous microtubes using custom made bioreactor <i>Günnur ONAK PULAT, Asena Gülenay TATAR, Yusuf Hakan USTA and Ozan KARAMAN</i>	220-226

**Research Article****Synergistic effect of h-BN on thermal conductivity of polymer composites****Nilay Kucukdogan** ^{a,*} ^aDepartment of Mechatronics Engineering, Manisa Celal Bayar University, Manisa, Turkey

ARTICLE INFO

Article history:

Received 25 July 2022

Accepted 01 November 2022

Published 15 December 2022

Keywords:

Bruggeman model

Boron nitride

Multi walled carbon nanotube

Polymer composite

ABSTRACT

The conductivity characteristics of polymers and polymer composites have become more significant recently. Good heat dissipation is required in many applications, such as circuit boards and heat exchangers, so it is essential to develop the thermal conductivity characteristics of the materials. The micro-fillers have been replaced with nano or hybrid fillers to increase the low thermal conductivity of the polymer. Hexagonal boron nitride (h-BN) and multi-walled carbon nanotubes (MW-CNT), both of which have good conductivity properties, are two popular filling materials. The presence of hydroxyl and amino active groups at the corners of the hexagonal structure of BN improves the thermal conductivity properties of the polymer composite. In addition, it shows high thermal conductivity behavior in polymer composite structures with BN and MW-CNT. It is essential to demonstrate the effects of the volume fraction of additives on the thermal properties of composites with various approaches. In this study, the thermal conductivity behaviors of h-BN/high-density polyethylene and h-BN/MW-CNT/high-density polyethylene composites are demonstrated using the theoretical Bruggeman model, which is based on the assumption that there are constant infinitesimal changes in the material so that there is an interaction between particles. The coefficient of determination (R^2) between the thermal conductivity values of the composites and the predictions of the Bruggeman theoretical model is greater than 0.98. This way, the synergetic effect of h-BN and MW-CNT/h-BN additives on thermal conductivity has been theoretically proven.

1. Introduction

Due to their electrical insulation, corrosion resistance, lightweight, simple and low energy requirement manufacturing, and low cost, polymer composite, a material that is frequently used in electronic packages, has drawn growing interest. In addition, effective heat dissipation has emerged as a critical issue for the everyday operation of electronics due to the rapid growth of electronic devices toward downsizing, portability, and integration. Improvements are being made to polymer composites' thermal conductivity to better manage and control heat dissipation in electronic devices. One of the most popular methods is adding materials with high conductivity filling material into the polymer structure. However, it has also been demonstrated that adding these materials in various sizes as filler material contributes to increased heat conductivity. First, filling materials used in micron sizes were left to nano and hybrid additive materials [1, 2]. The thermal conductivity of polymer composites is related to the polymer, fillers, and their

interactions. Here, it can change with the morphology, size, shape, and orientation of the fillers in the polymer structure and the formation of the interface or interphase with the polymer. Many parameters should be considered in the design of polymer composites with thermal conductivity. Selecting suitable polymers and fillers alone is not enough. The morphology and interaction of polymers and fillers must also be considered [3].

Metals with high thermal conductivity (copper, silver, zinc) [4] or metal oxides (alumina) [5, 6] and carbon-based [7] fillers increase the thermal conductivity of polymer composites. Among these, it has been demonstrated that good mechanical properties are obtained in addition to excellent thermal conductivity, especially in additive materials such as MW-CNT, fullerene, graphene, and boron nitride [8]. These carbon-based filler materials rapidly transfer electrons and phonons in their direction with little scattering. For this reason, the thermal conductivity of the produced composites is presented in two ways: in-plane and through-plane. When investigated

* Corresponding author. Tel.: +90 236 314 1010; Fax: +90 236 314 2020.

E-mail addresses: nilay.ozturk@cbu.edu.tr (N. Kucukdogan)

ORCID: 0000-0003-4375-0752 (N. Kucukdogan)

DOI: [10.35860/iarej.1148320](https://doi.org/10.35860/iarej.1148320)© 2022, The Author(s). This article is licensed under the CC BY-NC 4.0 International License (<https://creativecommons.org/licenses/by-nc/4.0/>).

depending on the volume fraction, very different results have been revealed in polymer composites in both directions. Zhang et al. presented an easy method for producing polymer composites and used the PVA/h-BN additive. They compared the through-plane and in-plane thermal conductivities of the composites they made and reported that the in-plane thermal conductivity was higher than the through-plane [9]. Gou et al. produced 25% by volume randomly dispersed h-BN nanosheets/ Polyvinylidene fluoride-co-hexafluoropropylene (P(VDF-HFP)) nanocomposites and compared them with P(VDF-HFP) and the in-plane thermal conductivity of h-BN nanosheets/P(VDF-HFP) at 25% by volume-oriented increased by 249% and 3057%, respectively [10]. Sun et al. produced h-BN nanolayer-based epoxy nanocomposites. They emphasized that the thermal interface resistance is an essential factor preventing thermal conductivity along the plane and that the composites they produced have high xy/in-plane thermal conductivity and low thermal conductivity in z/plane [11]. Hu et al. reported that they obtained the highest through-plane thermal conductivity in the composite with 9.5% filler loading in the fluorinated h-BN nanolayers/graphene oxide elastomer composites they produced. Liu et al. simultaneously improved both in-plane and out-of-plane thermal conductivity in h-BN/polyimide composite films. They reported that the in-plane and out-of-plane thermal conductivity of the composite film with a filler content of 30% increased by 1233% and 150% compared to pure polyimide [12]. Zhang et al. achieved flexibility and high thermal conductivity in the through-plane direction in producing h-BN/polyethylene composites. They emphasized that they obtained mechanical properties and high thermal conductivity [13]. Hu et al. characterized oriented h-BN/Silicone rubber composites as the ideal thematic interface material. They stated that they managed to increase the thermal conductivity value of 7.62 W/mK while maintaining the flexibility of the composites they produced [14]. Su et al. produced composites with high thermal conductivity and good electrical insulation using multi-layer graphene and h-BN fillers with cycloaliphatic epoxy resin. Adding hybrid filler material to composite production has achieved high through-plane thermal conductivity [15]. Sun et al. calculate the effective thermal conductivity for in-plane and through-plane thermal conductivity for h-BN polymer composites modeled with the new anisotropic equation. The heat transfer is demonstrated by simulating the finite element method [16].

The process of gaining thermal conductivity characteristics and experimentally designing the desired high thermal conductivity composites, and researching the results is time-consuming and costly. However, since the phenomena that will occur at polymer composites'

interfaces and/or interphases cannot be fully demonstrated, the existing mechanism is investigated with theoretical and empirical models, numerical analyses, and simulations in the experimental study process [17]. Among the frequently preferred favorite models, the Russell model estimates the thermal conductivity of the composite structure by building a model on which the filling material is distributed in the matrix in the form of uniform cubes and in a regular manner. However, the Maxwell model [18] is particularly successful in predicting the thermal conductivity of composites with low-volume fractions. This model is because the model defined the filling material as spherical particles. Although the filling material could be in different geometries (shape factor n), it was the Hamilton-Crosser [19] who made improvements to the model. On the other hand, Nielsen's model [20] included more complex factors while creating the model structure with factors related to particle size and shape. For example, using the Einstein coefficient, he also included the factor related to the shape and orientation of the particles in the model structure. Agari [21], on the other hand, introduced two basic models, parallel and serial, in 1987 and predicted that existing models would be between these two basic models. While the parallel model determines the upper limit, the serial model determines the lower limit. Then, based on the hypothesis that the particles have a homogeneous distribution in the polymer, Agari added the C_1 constant, which is related to the crystallinity and crystalline size of the polymer, and the C_2 factor, in which the thermal conduction for the additive material is transmitted in the form of a network chain to the model. Among these models, Bruggeman's theoretical model [22] built a robust theoretical model based on the hypothesis that there is a mutual interaction between particles thanks to infinitesimal changes. Although it has a more complex structure than other models, unlike most theoretical models, it has high predictive power without including any factor or parameter in the model.

This study includes a mathematical prediction of thermal conductivity behavior of filled polymer composites. In this context, thermal conductivity behaviors of composites containing h-BN and MW-CNT fillers were investigated based on theoretical models. As a result, the Bruggeman model successfully predicted the thermal conductivity behavior of thermoplastic composites produced by selecting an interface compatibilizing agent between high-density polyethylene and filler materials in composite production.

2. Materials and Methods

2.1 Materials and Methods

For the current study, the thermal conductivity data of polymer composites were obtained from the reference paper

[23]. The volume fraction and thermal conductivity of the composites are given in Table 1. In experimental studies, 10-30% filling material by volume was added to high-density polyethylene composites. While h-BN is chosen as the primary filling material, it is seen that the synergy between h-BN and MW-CNT increases thermal conductivity by adding 3% MW-CNT for another group of composites.

2.2. Methods

2.2.1 Classical Theoretical Models

Many models based on macroscopic properties have been presented to predict the thermal behavior of materials with heterogeneous structures, such as filled polymer composites. Existing models are divided into theoretical and empirical models. Some famous theoretical models are given in Table 2 [24].

In the model equations in Table 2, the thermal conductivity of λ , λ_1 , and λ_2 composites are the thermal conductivity of a matrix (continuous phase) and filler (dispersive phase), respectively. v (%) is the volume fraction of particles. The Russell and Maxwell-Eucken models designed for low volume ratios are given in Equation 1 and 2, respectively. In addition, the Hamilton Crosser model (Eq.3) is represented by the shape factor n . All the theoretical models in Table 2 except the Bruggeman model (see Eq. 4) satisfy the λ equation. In the simplified version of the Bruggeman model, $(1-v)$ is located to the equation's left. Here, a simplified version of the current model has been made and reduced to its current form.

Table 1. Experimental data [23]

		Volume fractions (%)						
Fillers	CNT	-	-	-	3	3	3	-
	h-BN	10	20	30	7	17	27	-
Matrix	HDPE	90	80	70	90	80	70	100
Thermal conductivity (W/mK)		0.61	0.881	1.199	0.711	1.088	1.54	0.415

Table 2. Some theoretical models

Models	Equations	
Russell	$\lambda = \lambda_1 \frac{v^{\frac{2}{3}} + \frac{\lambda_1}{\lambda_2} (1 - v^{\frac{2}{3}})}{v^{\frac{2}{3}} - v + \frac{\lambda_1}{\lambda_2} (1 - v^{\frac{2}{3}})}$	(1)
Maxwell-Eucken	$\lambda = \lambda_1 \frac{2\lambda_1 + \lambda_2 + 2v(\lambda_2 - \lambda_1)}{2\lambda_1 + \lambda_2 - v(\lambda_2 - \lambda_1)}$	(2)
Hamilton-Crosser	$\lambda = \lambda_1 \left[\frac{\lambda_2 + (n-1)\lambda_1 + (n-1)v(\lambda_2 - \lambda_1)}{\lambda_2 + (n-1)\lambda_1 - v(\lambda_2 - \lambda_1)} \right]$	(3)
Bruggeman	$1 - v = \frac{\lambda_2 - \lambda}{\lambda_2 - \lambda_1} \left(\frac{\lambda_1}{\lambda} \right)^{1/3}$	(4)

However, the equation of the current model is in a rather lengthy form (in Appendix). When Appendix is examined, it is seen that there are 3 different solutions belonging to the Bruggeman model.

The first solution includes λ , λ_1 , λ_2 , and v in the Bruggeman model structure. At the same time, the imaginary number represented by i is also included in the other solutions. The current model has a very complex structure, which shows that it offers a strong structure among theoretical models. In addition, unlike models such as Hamilton-Crosser, Nielsen, and Agari, it is a model created in basic form without including various factors and parameters in its structure.

3. Results and Discussion

The thermal conductivity behaviors of H-BN/high-density polyethylene and h-BN/MW-CNT/high-density polyethylene composites were modeled with the theoretical Bruggeman model. It is essential to reduce agglomeration and provide the desired formation of the network structure in the production of composites in high-density polyethylene thermoplastic matrix with fillers such as BN and MW-CNT. For this, it is advantageous to add modifying maleic anhydride grafted high-density polyethylene, which is a famous compatibilizer agent in composite production [23]. In addition, the results of the measurements in the in-plane direction of the thermal conductivity of the composites are included in the study.

Figure 1 shows the model estimates of the thermal conductivity coefficient of the theoretical Bruggeman model for h-BN/high-density polyethylene composites. In addition, the average deviation values of the model are shown for each volume fraction in Table 3.

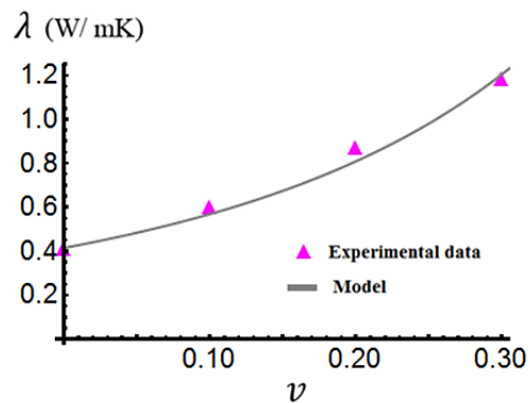


Figure 1. Bruggeman theoretical model prediction for h-BN/ high-density polyethylene composites

Table 3 The average deviation of the model estimate for h-BN/ high-density polyethylene composites

Volume fraction	Model
0.0	0.134
0.1	0.236
0.2	5.082
0.3	2.229

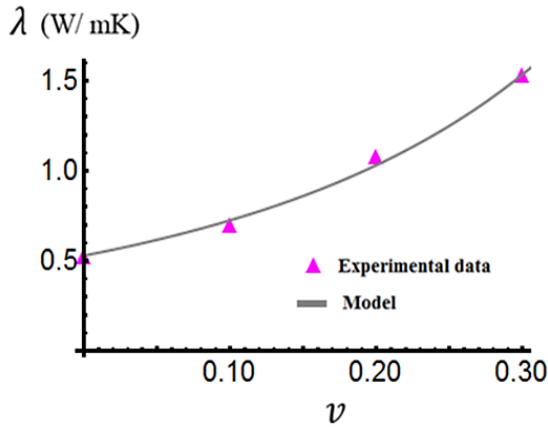


Figure 2. Bruggeman theoretical model prediction for h-BN/ MW-CNT/high-density polyethylene composites

Table 4 Average deviation of the model estimate for h-BN/MW-CNT/high-density polyethylene composites

Volume fraction	Model
0.0	0.134
0.1	2.136
0.2	3.082
0.3	0.229

The thermal conductivity of polyethylene composites increased together with the use of h-BN and MW-CNT fillers, which is attributed to the synergetic effect between the additives. The model estimates of the thermal conductivity coefficient of the theoretical Bruggeman model for h-BN/ MW-CNT/high-density polyethylene composites are shown in Figure 2. In addition, the mean deviation value of the model is presented in Table 4, including the data for all composites.

The Bruggeman model predicted the thermal conductivity behavior of h-BN/polyethylene and h-BN/MW-CNT/polyethylene composites with an accuracy of 97.8% and 99.4%, respectively. The average deviation values between the experimental data and the model predictions were calculated according to the volume fraction of each composite. The average deviation in filler ratios with 0, 10, 20, and 30 volume fractions are calculated as 0.134, 0.236, 5.082, and 2.229 for h-BN/polyethylene composites, and 0.134, 2.136, 3.082 for h-BN/MW-CNT/polyethylene composites. Model estimates gave better results for h-BN and h-BN/MW-CNT/polyethylene composites, especially at 0% and 30 volume fractions.

Figures 1 and 2 show a significant increase in thermal conductivity coefficient with additional MW-CNT in 20% and 30% by volume h-BN filled composites. This situation was interpreted as the synergistic effect between h-BN and MW-CNT. According to the experimental data, the thermal conductivity coefficients of the composites have a positive correlation. Additionally, the estimates of existing theoretical and empirical models have slopes that increase with increasing additive ratios.

3. Conclusion

In this study, the thermal conductivity of both h-BN and h-BN/MW-CNT filled composites was estimated using the Bruggeman theoretical model, and the strong prediction capability of the model was demonstrated. The Bruggeman theoretical model predicts the thermal conductivity of high-density polyethylene composites over $R^2 > 0.97$. The current model, which very well predicts the thermal conductivity of h-BN filled composites, perfectly predicts the thermal conductivity coefficients of h-BN/MW-CNT filled composites. However, since the phenomena that will occur at the interfaces and/or interphases of polymer composites cannot be fully revealed, it becomes essential to investigate the existing mechanism with theoretical and empirical models, numerical analyzes, and simulations in the experimental study process. Considering the long duration of the experimental process and the costs in the investigation of the thermal conductivity of composites, a numerical investigation utilizing theoretical models can give an idea about the existing mechanism.

Declaration

The author declared no potential conflicts of interest with respect to the research, authorship, and/or publication of this article. The author also declared that this article is original, was prepared in accordance with international publication and research ethics, and ethical committee permission or any special permission is not required.

Author Contributions

N. Kucukdogan developed the methodology, performed the analysis and wrote the whole article.

References

- Ruan, K., et al., *Interfacial thermal resistance in thermally conductive polymer composites: a review*. Composites Communications, 2020. **22**: p. 100518.
- Yang, X., et al., *A review on thermally conductive polymeric composites: classification, measurement, model and equations, mechanism and fabrication methods*. Advanced composites and hybrid materials, 2018. **1**(2): p. 207-230.
- Guo, Y., et al., *Factors affecting thermal conductivities of the polymers and polymer composites: A review*. Composites Science and Technology, 2020. **193**: p. 108134.
- Leung, S.N., *Thermally conductive polymer composites and nanocomposites: Processing-structure-property relationships*. Composites Part B: Engineering, 2018. **150**: p. 78-92.
- Liu, C., et al., *ZnO nanowire-decorated Al₂O₃ hybrids for improving the thermal conductivity of polymer composites*. Journal of Materials Chemistry C, 2020. **8**(16): p. 5380-5388.
- Cakmak, N.K., H.H. Durmazucar, and K. Yapici, *A numerical study of the natural convection of Al₂O₃-EG nanofluid in a square enclosure and impacts and a comparison of various viscosity and thermal conductivity*

models. International Advanced Researches and Engineering Journal, 2021. 5(2): p. 218-230.

7. Sanker, S.B. and R. Baby, *Phase change material based thermal management of lithium ion batteries: A review on thermal performance of various thermal conductivity enhancers*. Journal of Energy Storage, 2022. 50: p. 104606.
8. Jouni, M., et al., *A representative and comprehensive review of the electrical and thermal properties of polymer composites with carbon nanotube and other nanoparticle fillers*. Polymer International, 2017. 66(9): p. 1237-1251.
9. Zhang, J., et al., *A facile method to prepare flexible boron nitride/poly (vinyl alcohol) composites with enhanced thermal conductivity*. Composites Science and Technology, 2017. 149: p. 41-47.
10. Gou, B., et al., *Polymer-based nanocomposites with ultra-high in-plane thermal conductivity via highly oriented boron nitride nanosheets*. Polymer Composites, 2022. 43(4): p. 2341-2349.
11. Sun, Z., et al. *Large-scale production of boron nitride nanosheets-based epoxy nanocomposites with ultrahigh through-plane thermal conductivity for electronic encapsulation*. in 2022 IEEE 72nd Electronic Components and Technology Conference (ECTC). 2022. IEEE.
12. Liu, D., et al., *Improving in-plane and out-of-plane thermal conductivity of polyimide/boron nitride film with reduced graphene oxide by a moving magnetic field induction*. Composites Science and Technology, 2022. 220: p. 109292.
13. Zhang, R.C., et al., *Flexible and Ultrahigh Through-Plane Thermally-Conductive Polyethylene/Boron Nitride Nanocomposite Films*. Macromolecular Materials and Engineering, 2022. 307(1): p. 2100695.
14. Hu, Q., et al., *Oriented BN/Silicone rubber composite thermal interface materials with high out-of-plane thermal conductivity and flexibility*. Composites Part A: Applied Science and Manufacturing, 2022. 152: p. 106681.
15. Su, Z., et al., *Synergistic enhancement of anisotropic thermal transport flexible polymer composites filled with multi-layer graphene (mG) and mussel-inspired modified hexagonal boron nitride (h-BN)*. Composites Part A: Applied Science and Manufacturing, 2018. 111: p. 12-22.
16. Sun, Y., et al., *A new anisotropic thermal conductivity equation for h-BN/polymer composites using finite element analysis*. International Journal of Heat and Mass Transfer, 2020. 160: p. 120157.
17. Liu, B., et al., *Stochastic integrated machine learning based multiscale approach for the prediction of the thermal conductivity in carbon nanotube reinforced polymeric composites*. Composites Science and Technology, 2022. 224: p. 109425.
18. Maxwell, J.C., *A treatise on electricity and magnetism*. Vol. 1. 1881: Clarendon press.
19. Hamilton, R. and O. Crosser, *Thermal conductivity of heterogeneous two-component systems*. Industrial & Engineering chemistry fundamentals, 1962. 1(3): p. 187-191.
20. Nielsen, L.E., *Thermal conductivity of particulate-filled polymers*. Journal of applied polymer science, 1973. 17(12): p. 3819-3820.
21. Agari, Y., et al., *Thermal conductivity of a polymer composite filled with mixtures of particles*. Journal of Applied Polymer Science, 1987. 34(4): p. 1429-1437.
22. Bruggeman, V.D., *Berechnung verschiedener physikalischer Konstanten von heterogenen Substanzen. I. Dielektrizitätskonstanten und Leitfähigkeiten der*

Mischkörper aus isotropen Substanzen. Annalen der physik, 1935. 416(7): p. 636-664.

23. Feng, M., et al., *Largely improved thermal conductivity of HDPE composites by building a 3D hybrid fillers network*. Composites Science and Technology, 2021. 206: p. 108666.
24. Kucukdogan, N., L. Aydin, and M. Sutcu, *Theoretical and empirical thermal conductivity models of red mud filled polymer composites*. Thermochimica Acta, 2018. 665: p. 76-84.

Appendix

$$\{\lambda = \lambda_2 - (2^{1/3} (-9 \lambda_1^2 \lambda_2^2 + 3 \lambda_1 (\lambda_1^3 - 3 v \lambda_1^3 + 3 v^2 \lambda_1^3 - v^3 \lambda_1^3 - 3 \lambda_1^2 \lambda_2 + 9 v \lambda_1^2 \lambda_2 - 9 v^2 \lambda_1^2 \lambda_2 + 3 v^3 \lambda_1^2 \lambda_2 + 6 \lambda_1 \lambda_2^2 - 9 v \lambda_1 \lambda_2^2 + 9 v^2 \lambda_1 \lambda_2^2 - 3 v^3 \lambda_1 \lambda_2^2 - \lambda_2^3 + 3 v \lambda_2^3 - 3 v^2 \lambda_2^3 + v^3 \lambda_2^3)))/(3 \lambda_1 (-27 \lambda_1^5 \lambda_2 + 81 v \lambda_1^5 \lambda_2 - 81 v^2 \lambda_1^5 \lambda_2 + 27 v^3 \lambda_1^5 \lambda_2 + 81 \lambda_1^4 \lambda_2^2 - 243 v \lambda_1^4 \lambda_2^2 + 243 v^2 \lambda_1^4 \lambda_2^2 - 81 v^3 \lambda_1^4 \lambda_2^2 - 81 \lambda_1^3 \lambda_2^3 + 243 v \lambda_1^3 \lambda_2^3 - 243 v^2 \lambda_1^3 \lambda_2^3 + 81 v^3 \lambda_1^3 \lambda_2^3 + 27 \lambda_1^2 \lambda_2^4 - 81 v \lambda_1^2 \lambda_2^4 + 81 v^2 \lambda_1^2 \lambda_2^4 - 27 v^3 \lambda_1^2 \lambda_2^4 + \sqrt{((-27 \lambda_1^5 \lambda_2 + 81 v \lambda_1^5 \lambda_2 - 81 v^2 \lambda_1^5 \lambda_2 + 27 v^3 \lambda_1^5 \lambda_2 + 81 \lambda_1^4 \lambda_2^2 - 243 v \lambda_1^4 \lambda_2^2 + 243 v^2 \lambda_1^4 \lambda_2^2 - 81 v^3 \lambda_1^4 \lambda_2^2 - 81 \lambda_1^3 \lambda_2^3 + 243 v \lambda_1^3 \lambda_2^3 - 243 v^2 \lambda_1^3 \lambda_2^3 + 81 v^3 \lambda_1^3 \lambda_2^3 + 27 \lambda_1^2 \lambda_2^4 - 81 v \lambda_1^2 \lambda_2^4 + 81 v^2 \lambda_1^2 \lambda_2^4 - 27 v^3 \lambda_1^2 \lambda_2^4)^2 + (-9 \lambda_1^2 \lambda_2^2 + 3 \lambda_1 (\lambda_1^3 - 3 v \lambda_1^3 + 3 v^2 \lambda_1^3 - v^3 \lambda_1^3 - 3 \lambda_1^2 \lambda_2 + 9 v \lambda_1^2 \lambda_2 - 9 v^2 \lambda_1^2 \lambda_2 + 3 v^3 \lambda_1^2 \lambda_2 + 6 \lambda_1 \lambda_2^2 - 9 v \lambda_1 \lambda_2^2 + 9 v^2 \lambda_1 \lambda_2^2 - 3 v^3 \lambda_1 \lambda_2^2 - \lambda_2^3 + 3 v \lambda_2^3 - 3 v^2 \lambda_2^3 + v^3 \lambda_2^3))^3})^{1/3} + 1/(3 \cdot 2^{1/3} \lambda_1) (-27 \lambda_1^5 \lambda_2 + 81 v \lambda_1^5 \lambda_2 - 81 v^2 \lambda_1^5 \lambda_2 + 27 v^3 \lambda_1^5 \lambda_2 + 81 \lambda_1^4 \lambda_2^2 - 243 v \lambda_1^4 \lambda_2^2 + 243 v^2 \lambda_1^4 \lambda_2^2 - 81 v^3 \lambda_1^4 \lambda_2^2 - 81 \lambda_1^3 \lambda_2^3 + 243 v \lambda_1^3 \lambda_2^3 - 243 v^2 \lambda_1^3 \lambda_2^3 + 81 v^3 \lambda_1^3 \lambda_2^3 + 27 \lambda_1^2 \lambda_2^4 - 81 v \lambda_1^2 \lambda_2^4 + 81 v^2 \lambda_1^2 \lambda_2^4 - 27 v^3 \lambda_1^2 \lambda_2^4 + 4 (-9 \lambda_1^2 \lambda_2^2 + 3 \lambda_1 (\lambda_1^3 - 3 v \lambda_1^3 + 3 v^2 \lambda_1^3 - v^3 \lambda_1^3 - 3 \lambda_1^2 \lambda_2 + 9 v \lambda_1^2 \lambda_2 - 9 v^2 \lambda_1^2 \lambda_2 + 3 v^3 \lambda_1^2 \lambda_2 + 6 \lambda_1 \lambda_2^2 - 9 v \lambda_1 \lambda_2^2 + 9 v^2 \lambda_1 \lambda_2^2 - 3 v^3 \lambda_1 \lambda_2^2 - \lambda_2^3 + 3 v \lambda_2^3 - 3 v^2 \lambda_2^3 + v^3 \lambda_2^3))^3)^{1/3}\}$$

$$\{\lambda = \lambda_2 + ((1 + i \sqrt{3}) (-9 \lambda_1^2 \lambda_2^2 + 3 \lambda_1 (\lambda_1^3 - 3 v \lambda_1^3 + 3 v^2 \lambda_1^3 - v^3 \lambda_1^3 - 3 \lambda_1^2 \lambda_2 + 9 v \lambda_1^2 \lambda_2 - 9 v^2 \lambda_1^2 \lambda_2 + 3 v^3 \lambda_1^2 \lambda_2 + 6 \lambda_1 \lambda_2^2 - 9 v \lambda_1 \lambda_2^2 + 9 v^2 \lambda_1 \lambda_2^2 - 3 v^3 \lambda_1 \lambda_2^2 - \lambda_2^3 + 3 v \lambda_2^3 - 3 v^2 \lambda_2^3 + v^3 \lambda_2^3)))/(3 \cdot 2^{2/3} \lambda_1 (-27 \lambda_1^5 \lambda_2 + 81 v \lambda_1^5 \lambda_2 - 81 v^2 \lambda_1^5 \lambda_2 + 27 v^3 \lambda_1^5 \lambda_2 + 81 \lambda_1^4 \lambda_2^2 - 243 v \lambda_1^4 \lambda_2^2 + 243 v^2 \lambda_1^4 \lambda_2^2 - 81 v^3 \lambda_1^4 \lambda_2^2 - 81 \lambda_1^3 \lambda_2^3 + 243 v \lambda_1^3 \lambda_2^3 - 243 v^2 \lambda_1^3 \lambda_2^3 + 81 v^3 \lambda_1^3 \lambda_2^3 + 27 \lambda_1^2 \lambda_2^4 - 81 v \lambda_1^2 \lambda_2^4 + 81 v^2 \lambda_1^2 \lambda_2^4 - 27 v^3 \lambda_1^2 \lambda_2^4 + \sqrt{((-27 \lambda_1^5 \lambda_2 + 81 v \lambda_1^5 \lambda_2 - 81 v^2 \lambda_1^5 \lambda_2 + 27 v^3 \lambda_1^5 \lambda_2 + 81 \lambda_1^4 \lambda_2^2 - 243 v \lambda_1^4 \lambda_2^2 + 243 v^2 \lambda_1^4 \lambda_2^2 - 81 v^3 \lambda_1^4 \lambda_2^2 - 81 \lambda_1^3 \lambda_2^3 + 243 v \lambda_1^3 \lambda_2^3 - 243 v^2 \lambda_1^3 \lambda_2^3 + 81 v^3 \lambda_1^3 \lambda_2^3 + 27 \lambda_1^2 \lambda_2^4 - 81 v \lambda_1^2 \lambda_2^4 + 81 v^2 \lambda_1^2 \lambda_2^4 - 27 v^3 \lambda_1^2 \lambda_2^4)^2 + 4 (-9 \lambda_1^2 \lambda_2^2 + 3 \lambda_1 (\lambda_1^3 - 3 v \lambda_1^3 + 3 v^2 \lambda_1^3 - v^3 \lambda_1^3 - 3 \lambda_1^2 \lambda_2 + 9 v \lambda_1^2 \lambda_2 - 9 v^2 \lambda_1^2 \lambda_2 + 3 v^3 \lambda_1^2 \lambda_2 + 6 \lambda_1 \lambda_2^2 - 9 v \lambda_1 \lambda_2^2 + 9 v^2 \lambda_1 \lambda_2^2 - 3 v^3 \lambda_1 \lambda_2^2 - \lambda_2^3 + 3 v \lambda_2^3 - 3 v^2 \lambda_2^3 + v^3 \lambda_2^3))^3})^{1/3} - 1/(6 \cdot 2^{1/3} \lambda_1) (1 - i \sqrt{3}) (-27 \lambda_1^5 \lambda_2 + 81 v \lambda_1^5 \lambda_2 - 81 v^2 \lambda_1^5 \lambda_2 + 27 v^3 \lambda_1^5 \lambda_2 + 81 \lambda_1^4 \lambda_2^2 - 243 v \lambda_1^4 \lambda_2^2 + 243 v^2 \lambda_1^4 \lambda_2^2 - 81 v^3 \lambda_1^4 \lambda_2^2 - 81 \lambda_1^3 \lambda_2^3 + 243 v \lambda_1^3 \lambda_2^3 - 243 v^2 \lambda_1^3 \lambda_2^3 + 81 v^3 \lambda_1^3 \lambda_2^3 + 27 \lambda_1^2 \lambda_2^4 - 81 v \lambda_1^2 \lambda_2^4 + 81 v^2 \lambda_1^2 \lambda_2^4 - 27 v^3 \lambda_1^2 \lambda_2^4 + \sqrt{((-27 \lambda_1^5 \lambda_2 + 81 v \lambda_1^5 \lambda_2 - 81 v^2 \lambda_1^5 \lambda_2 + 27 v^3 \lambda_1^5 \lambda_2 + 81 \lambda_1^4 \lambda_2^2 - 243 v \lambda_1^4 \lambda_2^2 + 243 v^2 \lambda_1^4 \lambda_2^2 - 81 v^3 \lambda_1^4 \lambda_2^2 - 81 \lambda_1^3 \lambda_2^3 + 243 v \lambda_1^3 \lambda_2^3 - 243 v^2 \lambda_1^3 \lambda_2^3 + 81 v^3 \lambda_1^3 \lambda_2^3 + 27 \lambda_1^2 \lambda_2^4 - 81 v \lambda_1^2 \lambda_2^4 + 81 v^2 \lambda_1^2 \lambda_2^4 - 27 v^3 \lambda_1^2 \lambda_2^4)^2 + 4 (-9 \lambda_1^2 \lambda_2^2 + 3 \lambda_1 (\lambda_1^3 - 3 v \lambda_1^3 + 3 v^2 \lambda_1^3 - v^3 \lambda_1^3 - 3 \lambda_1^2 \lambda_2 + 9 v \lambda_1^2 \lambda_2 - 9 v^2 \lambda_1^2 \lambda_2 + 3 v^3 \lambda_1^2 \lambda_2 + 6 \lambda_1 \lambda_2^2 - 9 v \lambda_1 \lambda_2^2 + 9 v^2 \lambda_1 \lambda_2^2 - 3 v^3 \lambda_1 \lambda_2^2 - \lambda_2^3 + 3 v \lambda_2^3 - 3 v^2 \lambda_2^3 + v^3 \lambda_2^3))^3})^{1/3}\}$$

$$\{\lambda = \lambda_2 + ((1 - i \sqrt{3}) (-9 \lambda_1^2 \lambda_2^2 + 3 \lambda_1 (\lambda_1^3 - 3 v \lambda_1^3 + 3 v^2 \lambda_1^3 - v^3 \lambda_1^3 - 3 \lambda_1^2 \lambda_2 + 9 v \lambda_1^2 \lambda_2 - 9 v^2 \lambda_1^2 \lambda_2 + 3 v^3 \lambda_1^2 \lambda_2 + 6 \lambda_1 \lambda_2^2 - 9 v \lambda_1 \lambda_2^2 + 9 v^2 \lambda_1 \lambda_2^2 - 3 v^3 \lambda_1 \lambda_2^2 - \lambda_2^3 + 3 v \lambda_2^3 - 3 v^2 \lambda_2^3 + v^3 \lambda_2^3)))/(3 \cdot 2^{2/3} \lambda_1 (-27 \lambda_1^5 \lambda_2 + 81 v \lambda_1^5 \lambda_2 - 81 v^2 \lambda_1^5 \lambda_2 + 27 v^3 \lambda_1^5 \lambda_2 + 81 \lambda_1^4 \lambda_2^2 - 243 v \lambda_1^4 \lambda_2^2 + 243 v^2 \lambda_1^4 \lambda_2^2 - 81 v^3 \lambda_1^4 \lambda_2^2 - 81 \lambda_1^3 \lambda_2^3 + 243 v \lambda_1^3 \lambda_2^3 - 243 v^2 \lambda_1^3 \lambda_2^3 + 81 v^3 \lambda_1^3 \lambda_2^3 + 27 \lambda_1^2 \lambda_2^4 - 81 v \lambda_1^2 \lambda_2^4 + 81 v^2 \lambda_1^2 \lambda_2^4 - 27 v^3 \lambda_1^2 \lambda_2^4 + \sqrt{((-27 \lambda_1^5 \lambda_2 + 81 v \lambda_1^5 \lambda_2 - 81 v^2 \lambda_1^5 \lambda_2 + 27 v^3 \lambda_1^5 \lambda_2 + 81 \lambda_1^4 \lambda_2^2 - 243 v \lambda_1^4 \lambda_2^2 + 243 v^2 \lambda_1^4 \lambda_2^2 - 81 v^3 \lambda_1^4 \lambda_2^2 - 81 \lambda_1^3 \lambda_2^3 + 243 v \lambda_1^3 \lambda_2^3 - 243 v^2 \lambda_1^3 \lambda_2^3 + 81 v^3 \lambda_1^3 \lambda_2^3 + 27 \lambda_1^2 \lambda_2^4 - 81 v \lambda_1^2 \lambda_2^4 + 81 v^2 \lambda_1^2 \lambda_2^4 - 27 v^3 \lambda_1^2 \lambda_2^4)^2 + 4 (-9 \lambda_1^2 \lambda_2^2 + 3 \lambda_1 (\lambda_1^3 - 3 v \lambda_1^3 + 3 v^2 \lambda_1^3 - v^3 \lambda_1^3 - 3 \lambda_1^2 \lambda_2 + 9 v \lambda_1^2 \lambda_2 - 9 v^2 \lambda_1^2 \lambda_2 + 3 v^3 \lambda_1^2 \lambda_2 + 6 \lambda_1 \lambda_2^2 - 9 v \lambda_1 \lambda_2^2 + 9 v^2 \lambda_1 \lambda_2^2 - 3 v^3 \lambda_1 \lambda_2^2 - \lambda_2^3 + 3 v \lambda_2^3 - 3 v^2 \lambda_2^3 + v^3 \lambda_2^3))^3})^{1/3} - 1/(6 \cdot 2^{1/3} \lambda_1) (1 - i \sqrt{3}) (-27 \lambda_1^5 \lambda_2 + 81 v \lambda_1^5 \lambda_2 - 81 v^2 \lambda_1^5 \lambda_2 + 27 v^3 \lambda_1^5 \lambda_2 + 81 \lambda_1^4 \lambda_2^2 - 243 v \lambda_1^4 \lambda_2^2 + 243 v^2 \lambda_1^4 \lambda_2^2 - 81 v^3 \lambda_1^4 \lambda_2^2 - 81 \lambda_1^3 \lambda_2^3 + 243 v \lambda_1^3 \lambda_2^3 - 243 v^2 \lambda_1^3 \lambda_2^3 + 81 v^3 \lambda_1^3 \lambda_2^3 + 27 \lambda_1^2 \lambda_2^4 - 81 v \lambda_1^2 \lambda_2^4 + 81 v^2 \lambda_1^2 \lambda_2^4 - 27 v^3 \lambda_1^2 \lambda_2^4 + \sqrt{((-27 \lambda_1^5 \lambda_2 + 81 v \lambda_1^5 \lambda_2 - 81 v^2 \lambda_1^5 \lambda_2 + 27 v^3 \lambda_1^5 \lambda_2 + 81 \lambda_1^4 \lambda_2^2 - 243 v \lambda_1^4 \lambda_2^2 + 243 v^2 \lambda_1^4 \lambda_2^2 - 81 v^3 \lambda_1^4 \lambda_2^2 - 81 \lambda_1^3 \lambda_2^3 + 243 v \lambda_1^3 \lambda_2^3 - 243 v^2 \lambda_1^3 \lambda_2^3 + 81 v^3 \lambda_1^3 \lambda_2^3 + 27 \lambda_1^2 \lambda_2^4 - 81 v \lambda_1^2 \lambda_2^4 + 81 v^2 \lambda_1^2 \lambda_2^4 - 27 v^3 \lambda_1^2 \lambda_2^4)^2 + 4 (-9 \lambda_1^2 \lambda_2^2 + 3 \lambda_1 (\lambda_1^3 - 3 v \lambda_1^3 + 3 v^2 \lambda_1^3 - v^3 \lambda_1^3 - 3 \lambda_1^2 \lambda_2 + 9 v \lambda_1^2 \lambda_2 - 9 v^2 \lambda_1^2 \lambda_2 + 3 v^3 \lambda_1^2 \lambda_2 + 6 \lambda_1 \lambda_2^2 - 9 v \lambda_1 \lambda_2^2 + 9 v^2 \lambda_1 \lambda_2^2 - 3 v^3 \lambda_1 \lambda_2^2 - \lambda_2^3 + 3 v \lambda_2^3 - 3 v^2 \lambda_2^3 + v^3 \lambda_2^3))^3})^{1/3}\}$$

$$\begin{aligned}
& \lambda_2^3)) / (3 \cdot 2^{2/3} \lambda_1 (-27 \lambda_1^5 \lambda_2 + 81 v \lambda_1^5 \lambda_2 - 81 v^2 \lambda_1^5 \lambda_2 + 27 v^3 \lambda_1^5 \\
& \lambda_2 + 81 \lambda_1^4 \lambda_2^2 - 243 v \lambda_1^4 \lambda_2^2 + 243 v^2 \lambda_1^4 \lambda_2^2 - 81 v^3 \lambda_1^4 \lambda_2^2 - 81 \\
& \lambda_1^3 \lambda_2^3 + 243 v \lambda_1^3 \lambda_2^3 - 243 v^2 \lambda_1^3 \lambda_2^3 + 81 v^3 \lambda_1^3 \lambda_2^3 + 27 \lambda_1^2 \lambda_2^4 \\
& - 81 v \lambda_1^2 \lambda_2^4 + 81 v^2 \lambda_1^2 \lambda_2^4 - 27 v^3 \lambda_1^2 \lambda_2^4 + \sqrt{((-27 \lambda_1^5 \lambda_2 + 81 v \\
& \lambda_1^5 \lambda_2 - 81 v^2 \lambda_1^5 \lambda_2 + 27 v^3 \lambda_1^5 \lambda_2 + 81 \lambda_1^4 \lambda_2^2 - 243 v \lambda_1^4 \lambda_2^2 + 243 \\
& v^2 \lambda_1^4 \lambda_2^2 - 81 v^3 \lambda_1^4 \lambda_2^2 - 81 \lambda_1^3 \lambda_2^3 + 243 v \lambda_1^3 \lambda_2^3 - 243 v^2 \lambda_1^3 \lambda_2^3 \\
& + 81 v^3 \lambda_1^3 \lambda_2^3 + 27 \lambda_1^2 \lambda_2^4 - 81 v \lambda_1^2 \lambda_2^4 + 81 v^2 \lambda_1^2 \lambda_2^4 - 27 v^3 \lambda_1^2 \\
& \lambda_2^4)^2 + 4 (-9 \lambda_1^2 \lambda_2^2 + 3 \lambda_1 (\lambda_1^3 - 3 v \lambda_1^3 + 3 v^2 \lambda_1^3 - v^3 \lambda_1^3 - 3 \lambda_1^2 \\
& \lambda_2 + 9 v \lambda_1^2 \lambda_2 - 9 v^2 \lambda_1^2 \lambda_2 + 3 v^3 \lambda_1^2 \lambda_2 + 6 \lambda_1 \lambda_2^2 - 9 v \lambda_1 \lambda_2^2 + 9 \\
& v^2 \lambda_1 \lambda_2^2 - 3 v^3 \lambda_1 \lambda_2^2 - \lambda_2^3 + 3 v \lambda_2^3 - 3 v^2 \lambda_2^3 + v^3 \lambda_2^3))^3})^{1/3} - \\
& 1 / (6 \cdot 2^{1/3} \lambda_1) (1 + i \sqrt{3}) (-27 \lambda_1^5 \lambda_2 + 81 v \lambda_1^5 \lambda_2 - 81 v^2 \lambda_1^5 \lambda_2 + 27 \\
& v^3 \lambda_1^5 \lambda_2 + 81 \lambda_1^4 \lambda_2^2 - 243 v \lambda_1^4 \lambda_2^2 + 243 v^2 \lambda_1^4 \lambda_2^2 - 81 v^3 \lambda_1^4 \lambda_2^2 \\
& - 81 \lambda_1^3 \lambda_2^3 + 243 v \lambda_1^3 \lambda_2^3 - 243 v^2 \lambda_1^3 \lambda_2^3 + 81 v^3 \lambda_1^3 \lambda_2^3 + 27 \lambda_1^2 \\
& \lambda_2^4 - 81 v \lambda_1^2 \lambda_2^4 + 81 v^2 \lambda_1^2 \lambda_2^4 - 27 v^3 \lambda_1^2 \lambda_2^4 + \sqrt{((-27 \lambda_1^5 \lambda_2 + \\
& 81 v \lambda_1^5 \lambda_2 - 81 v^2 \lambda_1^5 \lambda_2 + 27 v^3 \lambda_1^5 \lambda_2 + 81 \lambda_1^4 \lambda_2^2 - 243 v \lambda_1^4 \lambda_2^2 \\
& + 243 v^2 \lambda_1^4 \lambda_2^2 - 81 v^3 \lambda_1^4 \lambda_2^2 - 81 \lambda_1^3 \lambda_2^3 + 243 v \lambda_1^3 \lambda_2^3 - 243 v^2 \\
& \lambda_1^3 \lambda_2^3 + 81 v^3 \lambda_1^3 \lambda_2^3 + 27 \lambda_1^2 \lambda_2^4 - 81 v \lambda_1^2 \lambda_2^4 + 81 v^2 \lambda_1^2 \lambda_2^4 - 27 \\
& v^3 \lambda_1^2 \lambda_2^4)^2 + 4 (-9 \lambda_1^2 \lambda_2^2 + 3 \lambda_1 (\lambda_1^3 - 3 v \lambda_1^3 + 3 v^2 \lambda_1^3 - v^3 \lambda_1^3 - 3 \\
& \lambda_1^2 \lambda_2 + 9 v \lambda_1^2 \lambda_2 - 9 v^2 \lambda_1^2 \lambda_2 + 3 v^3 \lambda_1^2 \lambda_2 + 6 \lambda_1 \lambda_2^2 - 9 v \lambda_1 \lambda_2^2 + \\
& 9 v^2 \lambda_1 \lambda_2^2 - 3 v^3 \lambda_1 \lambda_2^2 - \lambda_2^3 + 3 v \lambda_2^3 - 3 v^2 \lambda_2^3 + v^3 \lambda_2^3))^3})^{1/3} \}
\end{aligned}$$

**Research Article**

Production and characterization of activated carbon from Black Poplar (*Populus Nigra*) wood waste with different chemical activation methods

Mehmet Emin Ergun^{a,*}  and Saban Bulbul^b 

^aAlanya Alaadim Keykubat University, Akseki Vocational High School, Antalya, 07630, Turkey

^bNecmettin Erbakan University, Faculty of Seydişehir Ahmet Cengiz Engineering Faculty, Konya, 42370, Turkey

ARTICLE INFO**Article history:**

Received 12 August 2022

Accepted 23 November 2022

Published 15 December 2022

Keywords:

Activated carbon

Black Poplar

Chemical activation

Wood waste

ABSTRACT

In this study, the producibility of activated carbon from wood waste by using the chemical activation method was investigated and the produced activated carbon was compared with commercial activated carbon. Activated carbon was produced from black poplar wood waste using zinc chloride and phosphoric acid. The density values of the produced activated carbons were determined by the picometer method. Field Emission Scanning Electron Microscopy (FESEM) was used to analyze the microstructure and perform the elemental mapping. To determine the chemical content of activated carbon, it was also characterized by Fourier-transform infrared spectroscopy (FTIR) and energy dispersion spectroscopy (EDS). Based on the density and FESEM results, it was determined that the produced activated carbon had a lower density and porous structure. In addition, EDS analysis showed that the activated carbon produced from black poplar wood waste was purer than commercial activated carbon.

1. Introduction

Materials obtained by increasing the internal surface area and pore volume through activation of organic and inorganic substances, the majority of which consist of carbon, by chemical and physical methods are called activated carbon [1]. This type of carbon can be distinguished from elemental carbon by the fact that its outer and inner surfaces have oxygenated functional groups. In the high and environmental area, it is microporous, and the total pore volume is greater than 0.2 mL/g, and the BET (Brunauer–Emmett–Teller) surface area is wider than 400 m². The pore diameter varies between 3 Å and a few 1000 Å [1,2].

Activated carbon is mostly used in water treatment to adsorb organic compounds [3], oils [4], and toxic substances [5]. It is often applied due to its high surface area and adsorption capacity. The increasing demand for water treatment all over the world due to the exhausting natural resources [6–8] and the increasing amount of pollutants lead to the activated carbon sector growth [9]. Moreover, strict rules and regulations related to the treatment of industrial wastewater promote the further production of activated carbon [10]. In the food and beverage sectors, activated carbon is also used to remove

pollutants such as heavy metals, odor and color-giving substances, amino acids, and toxic components [11]. Due to the fact that customers pay more attention to food safety and quality, the consumption of activated carbon is increasing day by day [12]. Furthermore, activated carbon has industrial uses for removal CO₂ [13–15], recovering different solvents [16,17], and controlling mercury vapor emissions [18,19] and waste gases [20,21]. The activated carbons are utilized in the manufacture of the special chemicals, metal recovery [22], and energy storage [23]. The current increasing energy demand has led to an increase in battery consumption, which has led to an improvement in the manufacture of energy storage devices [24–26]. As a result of the emergence of new usage areas of activated carbon every year and the corresponding increase in production capacity, the global activated carbon market size reached \$2.96 billion in 2020. The market is expected to grow from \$3.12 billion in 2021 to \$4.50 billion in 2028 [27].

It is known that there are different manufacturing methods in activated carbon production; the most commonly used of these methods are physical and chemical activation methods. Physical activation consists of two complementary stages as degradation of organic

* Corresponding author. Tel.: +90 242 510 60 60 / 6562; Fax: +90 242 510 61 72.

E-mail addresses: mehmet.ergun@alanya.edu.tr (M.E. Ergun), sabanbulbul42@hotmail.com (S. Bulbul)

ORCID: 0000-0002-9938-7561 (M.E. Ergun), 0000-0002-9268-1469 (S. Bulbul)

DOI: [10.35860/iarej.1161044](https://doi.org/10.35860/iarej.1161044)

© 2022, The Author(s). This article is licensed under the CC BY-NC 4.0 International License (<https://creativecommons.org/licenses/by-nc/4.0/>).

substances and activation of the carbonized structure. In the first place, hydrogen and oxygen are removed from the raw material and the main skeleton is formed. In the second stage, the activation process is carried out by using water vapor or CO₂ gas at a temperature of 800-1000 °C or by using both gases, and activated carbon is produced [28]. Because the efficiency of chemical activation is higher and it is produced at low temperatures, it is preferred more compared to physical activation.

The surface areas of the activated carbons obtained as a result of chemical activation are larger and the pore volumes are bigger. Depending on the chemical activation agent used, the chemical and physical properties of the resulting activated carbon may vary. Activated carbon is obtained by bringing the starting material to the appropriate dimensions and reacting with the chemical substance at 400-1000°C, or by reacting the carbonized starting material with the chemical substance. When the literature is examined, it is seen that activation agents with different properties are used in this method. Some of them are boric acid, calcium hydroxide, calcium chloride, phosphoric acid, sulfuric acid, zinc chloride, iron (III) chloride, potassium carbonate, potassium hydroxide, manganese (II) chloride, nitric acid, sodium chloride, and sodium sulphate [29,30]. Some studies related to this issue in the literature are as follows.

In a study conducted by Hajati et al. [31], activated carbon was produced using the chemical activation method. As an activation agent, they used nitric acid. They conducted investigations on the surface characterization and adsorption of the obtained activated carbon. They observed that the obtained activated carbon expanded the surface area and increased the absorption rate [31].

In a study conducted on eucalyptus wood waste, KOH and NaOH were used as activation agents and the obtained activated carbon was compared with activated carbon obtained from lignite. Adsorption capacity and porosity distribution of activated carbons obtained by the chemical activation method were investigated. Based on the data obtained, scholars reported that the microporosity distribution of activated carbon produced by the NaOH activation agent was larger than that of KOH. They also observed that its adsorption capacity was higher than that of lignite [32].

Acharya et al. successfully produced activated carbon from the activation of tamarind wood with zinc chloride. They investigated the usability of activated carbon in the treatment of wastewater (removal of lead) and in agricultural fields. They emphasized that the surface area of the produced activated carbon enlarged, the lead contained in the wastewater could be adsorbed, and it was a cheaper method compared to other methods [33].

The aim of this study is to investigate the physical and chemical properties of activated carbons obtained from

black poplar wood waste by using two different methods with ZnCl₂ and H₃PO₄ chemical activation agents. In addition, today, it is aimed to increase a sustainable economy and environmental awareness and to obtain products with a higher added value.

2. Material and Method

The black poplar (*Populus nigra*) wood waste used in this study was obtained in the form of powder and free of charge from an enterprise located in Konya Seydişehir Carpenters Industry. Commercial activated carbon was purchased from Aromel Chemical (Konya, Turkey) in order to compare it with the activated carbon which produced in this study. Zinc chloride (ZnCl₂) and phosphoric acid (H₃PO₄) were used in the activation process, while hydrochloric acid (HCl) and potassium hydroxide (KOH) were used during the washing of the produced activated carbon. ZnCl₂, H₃PO₄, HCl and KOH were of analytical purity, and they were obtained from Merk (Darmstadt, Germany) or Fluka (Jul, Switzerland) companies.

In this study, activated carbon production was carried out using black poplar wood (*Populus nigra*) with the help of acid (phosphoric acid) and salt (zinc chloride) activation agents (Figure 1).

2.1 Production of Activated Carbon with Phosphoric Acid

3 kg of black poplar wood waste in powder form was mixed by adding 3 liters of phosphoric acid (50% wt) and 3 liters of pure water. In order to react wood waste with phosphoric acid, it was treated at 110°C for two hours. Then the mixture was dried by waiting in the drying-oven at 80°C for 24 hours. For the activation process, the dried material was cooled at room temperature after keeping it for 1.5 hours at 600° under argon gas (50 milliliters/min). It was washed first with 0.5 M KOH, then with hot deionized water until the pH value was 6-6.5. After the washed activated carbon was dried at 100°C for 6 hours, it was ground and become ready for use [34].

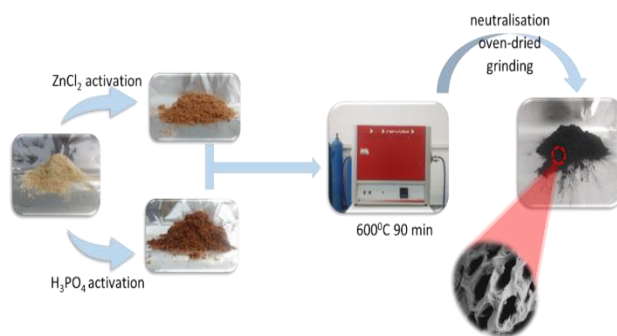


Figure 1. Production of activated carbon from black poplar

2.2 Production of Activated Carbon with Zinc Chloride

For the production of activated carbon with zinc chloride, 3 kg of powdered black poplar wood waste was made into a dough by adding 1.5 kg of zinc chloride and 3.75 liters of purified water and kneaded. In order for the raw material to react with zinc chloride, it was treated at room temperature for 24 hours. Then the mixture was dried by keeping it in the drying-oven at 80°C for 24 hours. The dried material was kept for 1.5 hours at 600° under argon gas (50 milliliters/min) for the activation process and then cooled at room temperature. It was first washed with 0.5 M HCl, then with hot deionized water until the pH value was 6-6.5. The washed activated carbon was dried at 100°C for 6 hours and then ground and become ready for use [35].

2.3 Characterization

The densities of the produced activated carbons were determined by helium pycnometer (Micromeritics–Accupyc2 1340). On the other hand, the morphologies of activated carbons were examined using Field Emission Scanning Electron Microscopy (FE-SEM) (ZEISS GeminiSEM 500). To increase their conductivity, activated carbons were coated with iridium with a thickness of 5 nm. During the examination of the microstructure images, the operating voltage of the microscope was selected as 2.00 kV. In addition, the functional groups of the activated carbons and their changes during the exposure process were determined by identifying the absorbance values whose FTIR (Thermo Scientific - Nicolet iS20) spectrums were determined at the range of 400 – 4000 cm^{-1} and the groups corresponding to these in the literature.

3. Result and Discussion

The FTIR spectra of commercial activated carbon (O) and zinc chloride (WWS) and phosphoric acid (WWA) based activated carbons between 400 and 4000 cm^{-1} are shown in Figure 2.

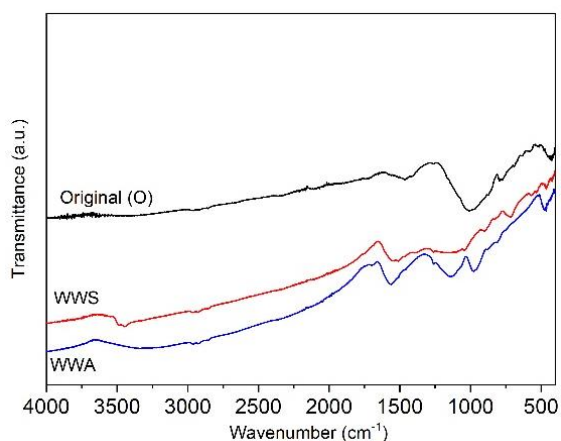


Figure 2. FT-IR results of commercial and produced activated carbon

The spectra of commercial activated carbon (O) samples displayed the following band: 1460 cm^{-1} could be assigned to C–H group. The presence of bands in the 1012 cm^{-1} wave number ranges could be due to C–O stretching vibrations. When the activated carbon peaks produced by zinc chloride activation (WWS) are examined, the peak at 3480 cm^{-1} shows the -OH peak and the peak at 1543 cm^{-1} shows the presence of carboxylic acid and/or lactone groups. When the peaks of activated carbon produced by phosphoric acid activation (WWA) are examined, it is seen that the peaks observed in the range of 3340 cm^{-1} bands are hydroxyl (O-H) groups. In addition, the peak observed in the 1400 cm^{-1} band indicates the presence of phenol in activated carbon. Peaks seen in the range of 2855-3000 cm^{-1} bands indicate the presence of aliphatic structures. These peaks were observed in activated carbon samples produced by both activations. Peaks seen in the band range of 1550-1800 cm^{-1} indicate a C=O bond structure; ketones, aldehydes, esters, and carboxylic acids are organic groups with this type of bond structure. Peaks were observed in this band range in the activated carbon samples produced by both activation agents. In particular, the peak seen in the 1600 cm^{-1} band indicates the presence of aromatic structures (C=C) and it was observed in both samples. The peaks observed in the band range of 950-1300 cm^{-1} indicate the presence of C-O, P=O, C-O-P, and P=O-OH groups. In both samples, there are peaks in this band range, but it is rather difficult to determine to which group these peaks belong. In the literature, it has been stated that the 1216-1196 cm^{-1} band corresponds to C-O, the 1085-1240 cm^{-1} band corresponds to P=O, and the 1180 cm^{-1} peak corresponds to P=O-OH groups [36,37]. Especially in activated carbon samples produced by chemical activation, peaks in the band range of 1080-1185 cm^{-1} are more evident. The reason for this is that there are P=O and P=O-OH groups due to the phosphoric acid used for activation [38].

Although activated carbons are known as materials with a large specific surface area and high porosity, it seems that many commercial activated carbons do not fully fit this definition [39]. In Figure 3 (a, b), FE-SEM images of commercial activated carbon taken with different magnifications are given. When the images were examined, it was seen that there were heterogeneously distributed pits on the surface of activated carbons rather than pores. In particular, in the FE-SEM images taken with 10 k magnification, the presence of small pores surrounding the pits is observed. Figure 3 (c, d) shows the surface physical morphology of WWA-encoded activated carbon obtained from wood waste by the chemical activation method using phosphoric acid and the FE-SEM images of the obtained activated carbon samples. When the images are examined, it is possible to say that compared to the commercial activated carbon with O code, pores are formed more clearly, and the pore volume is larger. Moreover, it is clearly seen that

compared to HA activated carbon, it is distributed not in the form of dimples, but in hollow spherical pores form and more homogeneously. In addition, it was found that the specified activated carbon had smooth walls and identified edges, and there was a distance between the gaps. It was also observed that the gaps were of different sizes. This situation suggests that the structure of wood waste is reorganized during activation [34,40]. FE-SEM images of WWS-coded activated carbon obtained from wood waste by chemical activation method using Zinc chloride ($ZnCl_2$) are given in Figure 3 (e, f).

When the FE-SEM images were examined, the formations of pore morphologies were detected relatively clearly compared to commercial activated carbon. Especially in the FE-SEM examination including high magnification, it was observed that the pores occurred in a larger number and almost all of them appeared in the ellipse shape morphology. It is thought that the $ZnCl_2$ chemical impregnation method leads to carbonization of the carbon skeleton after activation by causing the decomposition of cellulosic material and increases pore formation by undergoing aromatization. The formation of gaps was also caused by the evaporation of zinc chloride during the activation, and as a result of the

evaporation and separation of zinc chloride from the places it originally occupied, the number of gaps increased [41]. In this case, it can be clearly seen that the shape morphologies of activated carbons produced by the chemical activation method are more efficient and in desirable pore morphologies compared to commercial materials. Also, it was observed that the activated carbons obtained using the activation mechanism have different pore sizes and shapes depending on the activation agents [42]. In the study, to be able to compare activated Mapping and EDS analyses.

Mapping and EDS elemental analysis results of the commercial activated carbon (O) which have C, O, Si, Al and Fe elements were given in Figure 4a and Figure 4b. It was found that all elements, except Fe, were distributed homogeneously. As can be seen both in the EDS results (Figure 4b) and in the Mapping images (Figure 4c and Figure 4d), since activated carbons are mostly produced from organic raw materials or wastes, the intensive presence of C and O is an expected result [10]. In a study conducted by Park et al. (2020), it was reported that activated carbon produced from coconut fiber has C and O contents, similar to our study [43].

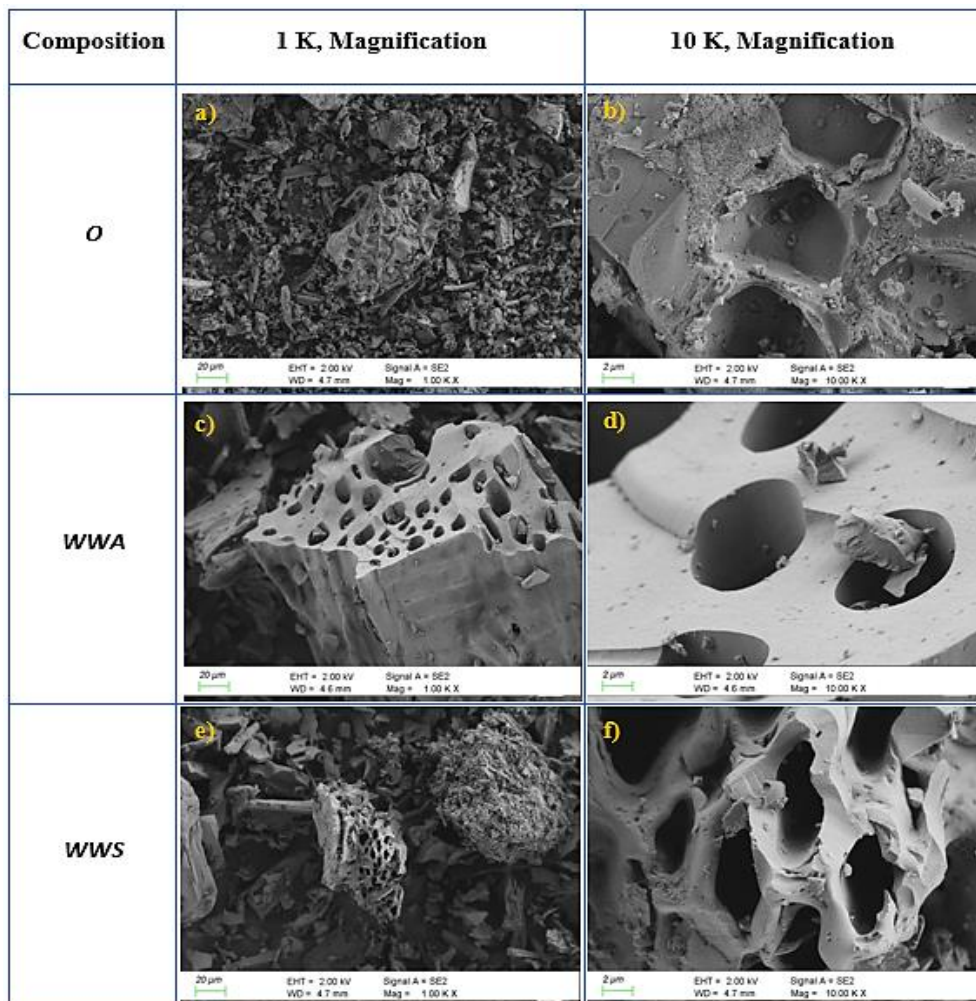


Figure 3. FE-SEM images for different type of activated carbons

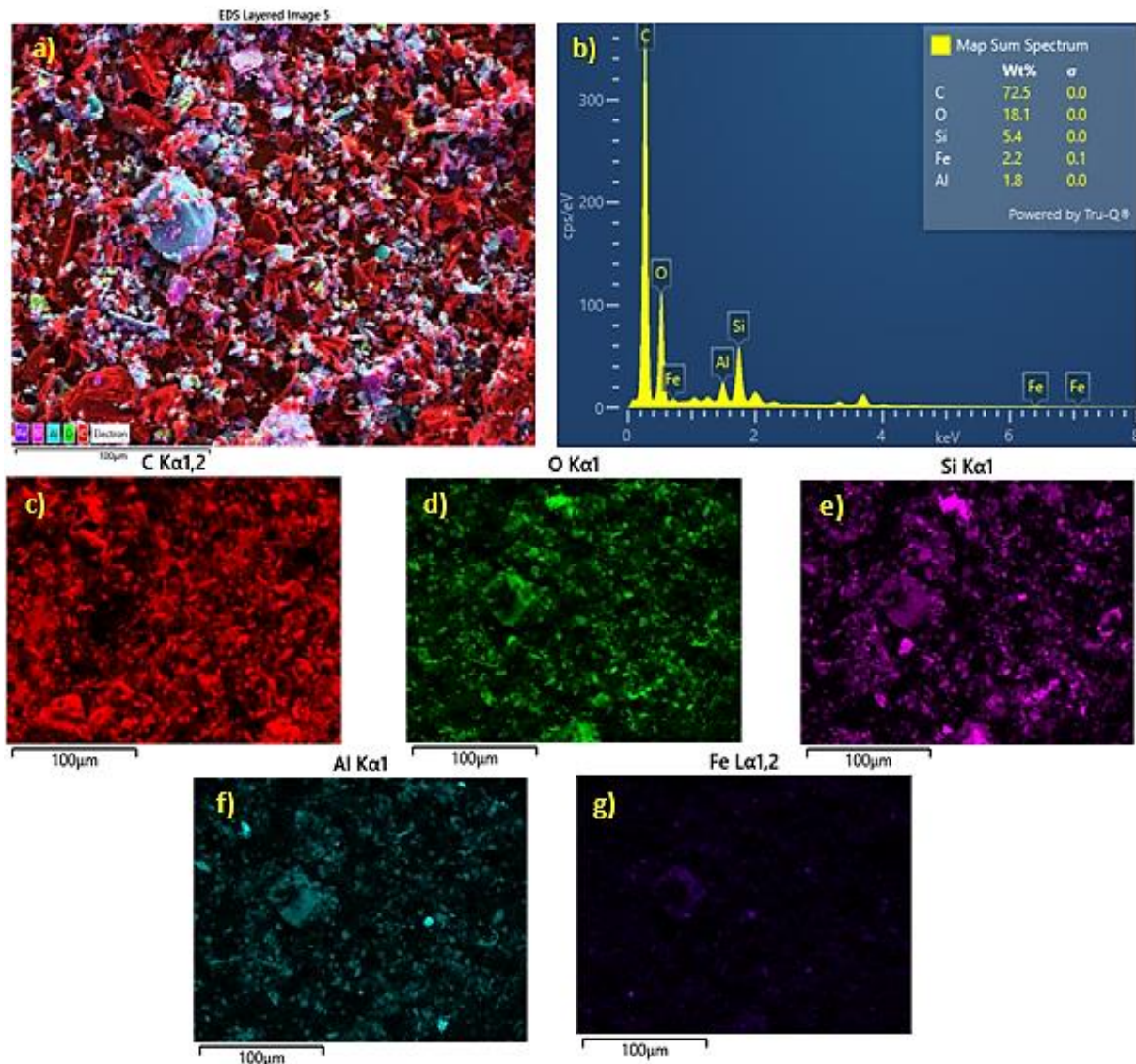


Figure 4. FE-SEM Mapping and EDS analyses of commercial activated carbon

In this study, the Al and Si elements found in commercial activated carbon produced from coconut fiber are homogeneously distributed as seen in Figure 4e and Figure 4f. Monteiro et al. (2005) revealed the presence of Al and Si elements in coconut fibers by EDS analysis [44]. In addition, the Fe element, whose distribution is seen in Figure 4g, is present at a rate of 2.2% in commercial activated carbon. It is believed that the element Fe is an impurity that occurs during production or arises from the environment in which production is carried out.

Figure 5 shows the EDS and Mapping analyses of activated carbon produced from black poplar wood waste with a zinc chloride activation agent.

As can be seen in Figure 5a and Figure 5b, activated carbon produced from black poplar wood waste contains C, O, Zn, and Cl elements. It was determined that all the elements contained in activated carbon were distributed homogeneously. Since black poplar wood contains about 49% C and 42% O [45], the fact that C and O elements were

found intensively after pyrolysis was an expected result as can be seen both in the EDS results (Figure 5b) and in the Mapping images (Figures 5c, d). On the other hand, due to the activation process carried out at a high temperature, the amount of C in activated carbon increased and the amount of O decreased. In the study conducted by Fernandez et al. (2014), it was determined that the used raw material contained 43% C and 50.2% O elements before the production of activated carbon, while it contained 82.5% C and 14.1% O after the production of activated carbon [34]. In addition, it was observed that there were Zn and Cl elements in the environment due to the $ZnCl_2$ activation agent used (Figures 5e and f). In the literature, activated carbons produced from different raw materials with the $ZnCl_2$ activation agent also have similar results [35,46]. Figure 6 shows the EDS and Mapping analyses of activated carbon produced from black poplar wood waste with the phosphoric acid activation agent.

Table 1. Densities of activated carbons

Activated Carbons	Density (g/cm ³)
O	2.14
WWA	1.37
WWS	2.08

As can be seen in Figures 6a and 6b, there are C, O, and P elements in the activated carbon produced from black poplar wood waste. As mentioned above, it was found that the activated carbon produced as a result of pyrolysis of black poplar wood waste contains 69.1% C and 23.2% O. In addition, the distribution of C and O elements homogeneously in the material is seen in Figure 6c and Figure 6d. In the study conducted by Danish et al. (2013), as a result of EDS analysis, it was determined that the activated carbon produced from the Acacia mangium tree by using phosphoric acid activation contained 76.22% C, 17.8% oxygen, and 5.98% P [47]. On the other hand, it is seen in Figure 6e that the P element in the produced activated carbon is homogeneously distributed and the PO_4^3 ions are successfully modified to the activated carbon surface [48]. Since phosphoric acid is used as a chemical activation agent in the production of activated carbon, it is observed that carbon contains the P element. In their studies where they used phosphoric acid in the production of activated carbon, Vázquez et al. (2012) detected the presence of the P element in EDS and Mapping analyses [49].

Table 1 shows the densities of activated carbon obtained from black poplar wood waste and commercial activated carbon. The density of HA-coded activated carbon is 2.14 g/cm³, while the densities of activated carbons obtained in salt (WWS) and acid (WWA) media are 2.09 and 1.37 g/cm³, respectively. The slightly increased surface area and pore volume are mainly due to the formation of micropores by the breakdown of oxygen-enriched WWA activated carbon [50]. The EDS analysis results of activated carbons confirm this situation. Whereas WWA activated carbon has 23.2% O, WWS activated carbon has 10.2% O. In general, the large pore volume contradicts with the high density. The well-developed porous structure of activated carbons usually implies a very low material density [51]. When the FE-SEM images are examined, it is possible to say that some large-sized pores are formed as a result of inhomogeneous distributions of loose carbon precursors, and this also causes a low density.

4. Conclusions

In this study, it was seen that activated carbon could be produced from black poplar wood waste with the chemical activation method by using phosphoric acid and zinc chloride activation agents. FTIR analyses performed at absorbance values determined in the range of 400-4000 cm⁻¹ showed that activated carbons were successfully

synthesized. When the FE-SEM images were examined, it was seen that the density of activated carbon obtained by using phosphoric acid is higher than that of other activated carbons used in the study. The fact that this condition reduces the density was also confirmed by the results of density experiments. The EDS results showed that commercial activated carbon is not pure, that is, there are different elements in it. On the other hand, it was found that the obtained activated carbons (WWA and WWS) were pure, no other elements were found in them, and the main skeleton was formed correctly. As a result, it was understood from the experiments and analyses that activated carbon production was carried out successfully.

Declaration

The author(s) declared no potential conflicts of interest with respect to the research, authorship, and/or publication of this article. The author(s) also declared that this article is original, was prepared in accordance with international publication and research ethics, and ethical committee permission or any special permission is not required.

Author Contributions

M. E. Ergun developed the methodology. S. Bulbul performed the analysis. M. E. Ergun and S. Bulbul wrote the manuscript and proofread the manuscript together.

Acknowledgment

This work supported by Scientific Research Project at Necmettin Erbakan University (project no: 211231003), Turkey.

References

1. Çiftçi, H., *Aktif karbonla topraktan tuz adsorpsiyonu yolu ile tuzlanmış tarım arazilerinin ıslah edilebileceğinin araştırılması*, Msc Thesis, Harran Üniversitesi, Fen Bilimleri Enstitüsü (2013).
2. Baytar, O., *İğde çekirdeği ve kayın ağacından üretilen aktif karbonun ağır metal ve boyarmadde gideriminde kullanılması*, Doktora Tezi, Selçuk Üniversitesi, Fen Bilimleri Enstitüsü (2015).
3. Quinlivan, P.A., L. Li and D.R.U. Knappe, *Effects of activated carbon characteristics on the simultaneous adsorption of aqueous organic micropollutants and natural organic matter*. Water Research, 2005. **39**(8): p.1663–1673.
4. Okiel, K., M. El-Sayed and M.Y. El-Kady, *Treatment of oil-water emulsions by adsorption onto activated carbon, bentonite and deposited carbon*. Egyptian Journal of Petroleum, 2011. **20**(2): p.9–15.
5. Kantarli, I.C. and J. Yanik, *Activated carbon from leather shaving wastes and its application in removal of toxic materials*. Journal of Hazardous Materials, 2010. **179**(1): p.348–356.
6. Bülbül, Ş. and N. Akcakale, *The Production and mechanical properties of carburized corn cob ash added rubber compounds*. KGK-Kautschuk Gummi Kunststoffe, 2019. **72**(4/19): p.30–35.

7. Bülbül, Ş., N. Akçakale, M. Yaşar and H. Gökmeşe, *The effect of wood ash on the mechanical properties of rubber compounds*. *Materiali in Tehnologije*, 2019. **53**(3): p.333–339.
8. Bulbul, S., M. Yasar and N. Akcakale, *Effect of Changing of Filling Materials in NR-SBR Type Elastomer Based Rubber Materials on Mechanical Properties*. *Polymer(Korea)*, 2014. **38**(5): p.664–670.
9. Naji, S.Z. and C.T. Tye, *A review of the synthesis of activated carbon for biodiesel production: Precursor, preparation, and modification*. *Energy Conversion and Management: X*, 2022. **13**: p.100152.
10. González-García, P., *Activated carbon from lignocellulosics precursors: A review of the synthesis methods, characterization techniques and applications*. *Renewable and Sustainable Energy Reviews*, 2018. **82**: p.1393–1414.
11. Roy, G.M., *Activated Carbon Applications in the Food and Pharmaceutical Industries*. 1994. CRC Press.
12. Amine, A., H. Mohammadi, I. Bourais and G. Palleschi, *Enzyme inhibition-based biosensors for food safety and environmental monitoring*. *Biosensors and Bioelectronics*, 2006. **21**(8): p.1405–1423.
13. Sha, Y., J. Lou, S. Bai, D. Wu, B. Liu and Y. Ling, *Facile preparation of nitrogen-doped porous carbon from waste tobacco by a simple pre-treatment process and their application in electrochemical capacitor and CO₂ capture*. *Materials Research Bulletin*, 2015. **64**: p.327–332.
14. David, E. and J. Kopac, *Activated carbons derived from residual biomass pyrolysis and their CO₂ adsorption capacity*. *Journal of Analytical and Applied Pyrolysis*, 2014. **110**: p.322–332.
15. Rashidi, N.A., S. Yusup, A. Borhan and L.H. Loong, *Experimental and modelling studies of carbon dioxide adsorption by porous biomass derived activated carbon*. *Clean Technologies and Environmental Policy*, 2014. **16**(7): p.1353–1361.
16. Chen, Y., F. Zi, X. Hu, P. Yang, Y. Ma, H. Cheng, Q. Wang, X. Qin, Y. Liu, S. Chen and C. Wang, *The use of new modified activated carbon in thiosulfate solution: A green gold recovery technology*. *Separation and Purification Technology*, 2020. **230**: p. 115834.
17. Soleimani, M. and T. Kaghazchi, *Gold recovery from loaded activated carbon using different solvents*. *Journal of the Chinese Institute of Chemical Engineers*, 2008. **39**(1): p. 9–11.
18. Graydon, J.W., X. Zhang, D.W. Kirk and C.Q. Jia, *Sorption and stability of mercury on activated carbon for emission control*. *Journal of Hazardous Materials*, 2009. **168**(2): p. 978–982.
19. Yan, R., D.T. Liang and J.H. Tay, *Control of mercury vapor emissions from combustion flue gas*. *Environmental Science and Pollution Research*, 2003. **10**(6): p. 399.
20. Sreńscek-Nazzal, J., W. Kamińska, B. Michalkiewicz and Z.C. Koren, *Production, characterization and methane storage potential of KOH-activated carbon from sugarcane molasses*. *Industrial Crops and Products*, 2013. **47**: p. 153–159.
21. Martínez de Yuso, A., M.T. Izquierdo, R. Valenciano and B. Rubio, *Toluene and n-hexane adsorption and recovery behavior on activated carbons derived from almond shell wastes*. *Fuel Processing Technology*, 2013. **110**: p. 1–7.
22. Volesky, B., *Biosorbents for metal recovery*. *Trends in Biotechnology*, 1987. **5**(4): p. 96–101.
23. Sevilla, M. and R. Mokaya, *Energy storage applications of activated carbons: supercapacitors and hydrogen storage*. *Energy & Environmental Science*, 2014. **7**(4): p. 1250–1280.
24. Faraji, S. and F.N. Ani, *The development supercapacitor from activated carbon by electroless plating—A review*. *Renewable and Sustainable Energy Reviews*, 2015. **42**: p. 823–834.
25. Béguin, F., V. Presser, A. Balducci and E. Frackowiak, *Carbons and Electrolytes for Advanced Supercapacitors*. *Advanced Materials*, 2014. **26**(14): p. 2219–2251.
26. Chmiola, J., G. Yushin, Y. Gogotsi, C. Portet, P. Simon and P.L. Taberna, *Anomalous Increase in Carbon Capacitance at Pore Sizes Less Than 1 Nanometer*. *Science*, 2006. **313**(5794): p. 1760–1763.
27. <https://www.fortunebusinessinsights.com/activated-carbon-market-102175>. Accessed March 24, 2022.
28. Yunus, Z.M., Y. G., A. Al-Gheethi, N. Othman, R. Hamdan and N.N. Ruslan, *Advanced methods for activated carbon from agriculture wastes; a comprehensive review*. *International Journal of Environmental Analytical Chemistry*, 2022. **102**(1): p. 134–158.
29. Wigmans, T., *Industrial aspects of production and use of activated carbons*. *Carbon*, 1989. **27**(1): p. 13–22.
30. Gündoğdu, A., *Fabrika çay atıklarından aktif karbon üretimi, karakterizasyonu ve adsorpsiyon özelliklerinin incelenmesi*. Doktora Tezi, Karadeniz Teknik Üniversitesi (2018).
31. Hajati, S., M. Ghaedi and S. Yaghoubi, *Local, cheap and nontoxic activated carbon as efficient adsorbent for the simultaneous removal of cadmium ions and malachite green: Optimization by surface response methodology*. *Journal of Industrial and Engineering Chemistry*, 2015. **21**: p. 760–767.
32. Lillo-Ródenas, M.A., J.P. Marco-Lozar, D. Cazorla-Amorós and A. Linares-Solano, *Activated carbons prepared by pyrolysis of mixtures of carbon precursor/alkaline hydroxide*. *Journal of Analytical and Applied Pyrolysis*, 2007. **80**(1): p. 166–174.
33. Acharya, J., J.N. Sahu, C.R. Mohanty and B.C. Meikap, *Removal of lead(II) from wastewater by activated carbon developed from Tamarind wood by zinc chloride activation*. *Chemical Engineering Journal*, 2009. **149**(1): p. 249–262.
34. Fernandez, M.E., G.V. Nunell, P.R. Bonelli and A.L. Cukierman, *Activated carbon developed from orange peels: Batch and dynamic competitive adsorption of basic dyes*. *Industrial Crops and Products*, 2014. **62**: p. 437–445.
35. El Nemr, A., R.M. Aboughaly, A. El Sikaily, S. Ragab, M.S. Masoud and M.S. Ramadan, *Microporous nano-activated carbon type I derived from orange peel and its application for Cr(VI) removal from aquatic environment*. *Biomass Conversion and Biorefinery*. 2020. 1-19
36. Puziy, A.M., O.I. Poddubnaya, A. Martínez-Alonso, F. Suárez-García and J.M.D. Tascón, *Surface chemistry of phosphorus-containing carbons of lignocellulosic origin*. *Carbon*, 2005. **43**(14): p. 2857–2868.
37. Guo, Y. and D.A. Rockstraw, *Activated carbons prepared from rice hull by one-step phosphoric acid activation*. *Microporous and Mesoporous Materials*, 2007. **100**(1): p. 12–19.
38. Örkün, Y., *Fındık kabuğundan fiziksel ve kimyasal aktivasyonla aktif karbon üretimi ve karakterizasyonu*, Ms Thesis, İstanbul Teknik Üniversitesi, Enerji Enstitüsü (2011).

39. Rahim, Y.A., S.N. Aqmar and D.R. Dewi. *ESR study of electron trapped on activated carbon by KOH and ZnCl₂ activation*. *Journal of Materials Science and Engineering*, 2010. **4**(3):1-10
40. Valizadeh, S., H. Younesi and N. Bahramifar. *Preparation and Characterization of Activated Carbon from the Cones of Iranian Pine Trees (Pinus eldarica) by Chemical Activation with H₃PO₄ and Its Application for Removal of Sodium Dodecylbenzene Sulfonate Removal from Aqueous Solution*. *Water Conservation Science and Engineering*, 2018. **3**(4): p. 253–265.
41. Shrestha, L.K., M. Thapa, R.G. Shrestha, S. Maji, R.R. Pradhananga and K. Ariga. *Rice Husk-Derived High Surface Area Nanoporous Carbon Materials with Excellent Iodine and Methylene Blue Adsorption Properties*. *C — Journal of Carbon Research*, 2019. **5**(1): p. 10.
42. Liang, Y., H. Liu, Z. Li, R. Fu and D. Wu. *In situ polydopamine coating-directed synthesis of nitrogen-doped ordered nanoporous carbons with superior performance in supercapacitors*. *Journal of Materials Chemistry A*, 2013. **1**(48): p. 15207–15211.
43. Park, J.H., H. Ur Rasheed, K.H. Cho, H.C. Yoon and K.B. Yi. *Effects of magnesium loading on ammonia capacity and thermal stability of activated carbons*. *Korean Journal of Chemical Engineering*, 2020. **37**(6): p. 1029–1035.
44. Monteiro, S.N., L.A.H. Terrones, F.P. Lopes and J.R.M. d'Almeida. *Mechanical strength of polyester matrix composites reinforced with coconut fiber wastes*. *Revista Matéria*, 2005. **10**(4): p. 571–576.
45. Jasinskas, A., G. Šiaudinis, M. Martinkus, D. Karčiauskienė, R. Repšienė, N. Pedišius and T. Vonžodas. *Evaluation of Common Osier (Salix viminalis L.) and Black Poplar (Populus nigra L.) Biomass Productivity and Determination of Chemical and Energetic Properties of Chopped Plants Produced for Biofuel*. *Baltic Forestry*, 2017. **23**(3): p. 666-672.
46. Bal Altuntaş, D., V. Nevruzoğlu, M. Dokumacı and Ş. Cam. *Synthesis and characterization of activated carbon produced from waste human hair mass using chemical activation*. *Carbon Letters*, 2020. **30**(3): p. 307–313.
47. Danish, M., R. Hashim, M.N.M. Ibrahim and O. Sulaiman. *Effect of acidic activating agents on surface area and surface functional groups of activated carbons produced from Acacia mangium wood*. *Journal of Analytical and Applied Pyrolysis*, 2013. **104**: p. 418–425.
48. Liu, X., C. He, X. Yu, Y. Bai, L. Ye, B. Wang and L. Zhang. *Net-like porous activated carbon materials from shrimp shell by solution-processed carbonization and H₃PO₄ activation for methylene blue adsorption*. *Powder Technology*, 2018. **326**: p. 181–189.
49. Vázquez-Santos, M.B., F. Suárez-García, A. Martínez-Alonso and J.M.D. Tascón. *Activated Carbon Fibers with a High Heteroatom Content by Chemical Activation of PBO with Phosphoric Acid*. *Langmuir*, 2012. **28**(13): p. 5850–5860.
50. Zhang, S., J. Zhu, Y. Qing, L. Wang, J. Zhao, J. Li, W. Tian, D. Jia and Z. Fan. *Ultramicroporous Carbons Puzzled by Graphene Quantum Dots: Integrated High Gravimetric, Volumetric, and Areal Capacitances for Supercapacitors*. *Advanced Functional Materials*, 2018. **28**(52): p. 1805898.
51. Jiang, Y., J. Li, Z. Jiang, M. Shi, R. Sheng, Z. Liu, S. Zhang, Y. Cao, T. Wei and Z. Fan. *Large-surface-area activated carbon with high density by electrostatic densification for supercapacitor electrodes*. *Carbon*, 2021. **175**: p. 281–288.

**Research Article****Effect of baffle angles on flow and heat transfer in a circular duct with nanofluids****Selma Akçay^{a,*} and Unal Akdag^b** ^aMechanical Engineering Department, Çankırı Karatekin University, Çankırı, 18100, Turkey^bMechanical Engineering Department, Aksaray University, Aksaray, 68100, Turkey

ARTICLE INFO

Article history:

Received 27 June 2022

Accepted 01 October 2022

Published 15 December 2022

*Keywords:*Baffle
Friction factor
Heat transfer
Nanofluid

ABSTRACT

This work numerically analyzes the hydraulic and thermal performance of CuO-water nanofluid in a circular duct with different baffle angles. In the numerical work, governing equations are discretized with the finite volume method, and the simulations are solved with SIMPLE algorithm. The surfaces of the duct containing baffles are kept at 340 K. In the analysis, the effects of different Reynolds numbers ($200 \leq Re \leq 1000$), nanoparticle volume fractions ($1\% \leq \phi \leq 3\%$), and baffle angles ($30^\circ \leq \alpha \leq 150^\circ$) on the thermal enhancement factor (η) and the friction factor are investigated. In addition, the flow and temperature contours are presented for different parameters within the duct. From those contours, it is observed that the baffles cause flow oscillation and recirculation zones are formed. The numerical results show that baffles and nanofluid flow contribute significantly to the thermal enhancement. The Nusselt number (Nu) and relative friction factor (r) increase as the Reynolds number and nanoparticle volume fraction increase. While the highest thermal enhancement factor and relative friction factor are obtained at $\alpha = 90^\circ$ baffle angle, the best performance evaluation criterion (PEC) value is found at $\alpha = 150^\circ$ baffle angle.

1. Introduction

Heat transfer improvement is an important research topic in many engineering fields. Passive methods used to increase the heat transfer of thermal devices provide significant advantages and cost savings. These methods include the applications such as baffles, twisted tapes, wire coil inserts, swirl generators, and the use of wavy/ribbed surfaces. Passive methods may have simplicity and require less or no additional system components, but they increase pressure drop significantly. These methods are preferred in various fields such as solar air ducts, heating/cooling applications, heat exchangers, cooling processing of gas turbine blade, nuclear reactors, transportation, food and chemical industry, etc. [1-4]. Flow and heat transfer in wavy channels have been examined theoretically and experimentally by many researchers and it was reported that the wavy surface geometry has an important potential on the heat transfer improvement due to both increasing the surface area and providing fluctuation in flow. However, it was declared these surfaces rise the pressure loss compared to straight ducts [5-7]. For this, flat ducts with relatively less pressure drop are preferred and it is

aimed to increase the thermal performance with the baffles added to the duct surfaces. It was reported that the baffles, which act similar to turbulators, increase heat transfer by improving flow mixing [8-15].

Menni et al. [16] numerically examined the flow and thermal performance of solar air ducts with different baffles. Menni et al. [17] examined the aerodynamic and thermal properties of multiple V fins in solar air ducts. In their work was changed in the fin attack-angle, length, and separation length, at different the flow rate. They reported that an optimum thermal enhancement factor was yielded for a 40° attack angle at $Re = 2163$. Salhi et al. [18] theoretically studied the effects of longitudinal baffles on hydraulic and thermal performance in tubular heat exchangers. In another study, Salhi et al. [19] analyzed the heat and mass transfer of partially inclined baffles in different arrangements in a straight duct for turbulent air flow. The results indicated that the thermal performance improved by 32.37% for the triangular baffles, and by 44.37% for the rectangular baffles. Nedunchezhiyan et al. [20] conducted a theoretic work examining the effects of baffles on flow and heat transfer. Razavi et al. [21] examined the effects on hydraulic and thermal improvement of the inclination angle of perforated

* Corresponding author. Tel.: +90-376-218-9532; Fax: +90-376-218-9536.

E-mail addresses: selmaakçay@karatekin.edu.tr (S. Akçay), uakdag@aksaray.edu.tr (U. Akdag)

ORCID: 0000-0003-2654-0702 (S. Akçay), 0000-0002-1149-7425 (U. Akdag)

DOI: [10.35860/iarej.1136354](https://doi.org/10.35860/iarej.1136354)© 2022, The Author(s). This article is licensed under the CC BY-NC 4.0 International License (<https://creativecommons.org/licenses/by-nc/4.0/>).

baffles in a rectangular channel under laminar flow conditions. Al Habet et al. [22] analyzed the thermal and hydraulic performance of perforated baffles in an inline and staggered arrangement in a rectangular duct. These studies indicated that thermal and hydraulic behaviors changed depending on the flow structure, channel geometry, baffle shape, baffle arrangement, and baffle angle.

Manca et al. [23] analyzed the thermal improvement of Al_2O_3 -water nanofluid for $20000 \leq \text{Re} \leq 60000$ at particle volume ratios of $0.00 \leq \phi \leq 0.04$ in a channel with different rib heights. They reported that heat transfer improved as the Re and ϕ increased, and an increment in pressure drop was also observed. Sriromreun et al. [24] experimentally and numerically analyzed the effects of Z-type baffle turbulators on thermal performance in a rectangular duct and indicated that the presence of Z-baffles has an important potential on thermal performance when compared to straight channels. Turgut and Kızılırmak [25] theoretically studied the thermal and flow properties of baffles with different angles ($30^\circ \leq \alpha \leq 150^\circ$) in a channel with a constant heat flux for turbulent flow. They declared that the maximum thermal improvement was found at $\alpha = 150^\circ$ baffle angle. Promvong et al. [26] stated in their experimental studies that Nu increased by about 92-208% compared to straight channels, and the pressure loss rose by 1.76-6.37 times in a channel using inclined horseshoe baffles. Kumar et al. [27] examined the thermal improvement of multiple V-type baffles in the solar air duct. Sahel et al. [28] declared in a numerical study that baffles in a rectangular duct enhanced heat transfer by 65%.

Fluids such as ethylene glycol, propylene glycol, water, and oil, commonly used in engineering fields, have low thermal features. To improve the thermophysical properties of such traditional liquids, nano-sized particles with high thermal conductivity are added. More than one method is used together to obtain a higher heat transfer coefficient. Some works were examined nanofluids with passive methods [29-32]. Heshmati et al. [33] studied the thermal performance of Al_2O_3 , CuO , ZnO and SiO_2 nanofluids at particle volume ratios of $0.00 \leq \phi \leq 0.04$, in the range of $50 \leq \text{Re} \leq 400$ on a backward step with corrugated baffles in different geometries. As a result, it was shown that nanofluids with high particle volume fractions provided high heat transfer rate. They also reported that the inclined baffles have the highest average Nusselt number with high pressure drop. Alnak [34] analyzed the thermal enhancement and friction factor of rectangular baffles with different angles in corrugated triangular channels for the k - ϵ turbulence model. As a result of the study, the results showed that for $\text{Re} = 6000$, the Nusselt number at 90° baffle angle is 52.8% higher than at 60° baffle angle. Ajeel et al. [35] carried out a theoretic work investigating the hydraulic and thermal

performance of ZnO -water nanofluid in a curved corrugated duct with L-shaped baffles for turbulent flow and analyzed the thermohydraulic performance for different Reynolds numbers, baffle angles, blocking rates, and nanoparticle volume ratios for constant temperature conditions. They reported that the baffles caused the thermal enhancement by increasing the eddy formation in the flow. Menni et al. [36] examined the effects of different angles of baffles and nanofluids on hydraulic and thermal enhancement in a heat exchanger for turbulent flow. They declared that the maximum thermal enhancement was found with high Reynolds number and vertical baffles.

In the literature, there are many studies examining thermal and hydraulic behaviours in ducts with different baffle configurations. However, due to the many parameters, new studies continue to find the optimum parameters. The fact that the investigated parameters such as channel and baffle shapes, baffle angles, flow and fluid parameters, nanofluid parameters are quite large, expanded the research to find the best parameters. The main purpose in these studies is to achieve the parameters that ensuring the highest heat transfer with the least pressure drop. In the literature, no definite parameter has been reported that provides the highest thermal enhancement with the lowest friction factor. Therefore, new studies are needed. To date, the effect of baffles angles on the flow of CuO -water nanofluid at varying particle volume ratios in a circular duct has not been investigated. In present study, the flow and thermal enhancement of CuO -water nanofluid at different particle volume fractions ($1\% \leq \phi \leq 3\%$) in a circular duct with different baffle angles ($30^\circ \leq \alpha \leq 150^\circ$) for $200 \leq \text{Re} \leq 1000$ are theoretically analyzed.

2. Material and Method

2.1 Schematic of the Numerical Model

Figure 1 indicates the schematic of the numerical model used in this study. The diameter of the circular duct (D) is 19 mm. At the duct entrance and exit, there is an unheated straight part $L_1 = 0.4$ m ($= 21 D$). The length of the channel consisting of baffles is $L_2 = 0.635$ m ($= 33 D$). The distance between the two baffles is considered as $S = 2D$. The length of the baffles (H) is $0.5D$ and the thickness of the baffles (t) is 0.5 mm. The baffles are placed on the walls of the duct with three different angles (α : 30° , 90° and 150°). The working fluid is the CuO -water nanofluid. Three different particle volume fractions are considered (ϕ : 1%, 2% and 3%). The diameters of the nanoparticles used in the study are considered $d = 20$ -50 nm. The solutions are performed for $200 \leq \text{Re} \leq 1000$ under laminar flow conditions.

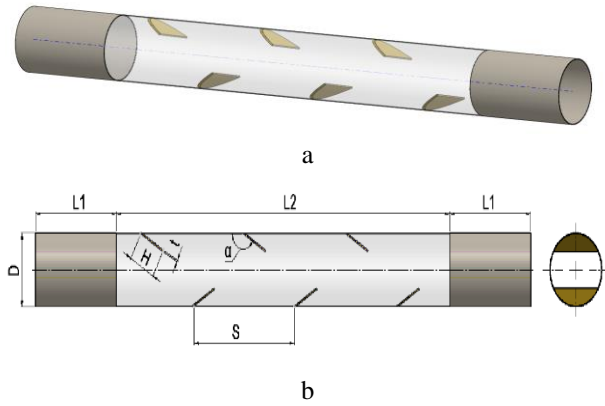


Figure 1. Geometry of the numerical model, a-3d solid model, b-2d scheme

2.2 Numerical Study

In the channel, the nanofluid flows in two-dimensional, laminar and steady conditions. The fluid is Newtonian type, single-phase and incompressible. Body forces and heat transfer by radiation are ignored. According to these assumptions, the governing equations are given by Equations (1) - (3) [37].

$$\nabla(\rho u) = 0 \quad (1)$$

$$\frac{\partial(u_i u_j)}{\partial x_i} = -\frac{\partial P}{\partial x_i} + \frac{1}{\text{Re}} \nabla^2 u_j \quad (2)$$

$$u_i \frac{\partial T}{\partial x_i} = \frac{1}{\text{RePr}} \nabla^2 T \quad (3)$$

The parameters used in the study were determined as Reynolds number (Re), Nusselt number (Nu), thermal enhancement factor (η), friction coefficient (f), and performance evaluation criterion (PEC). The equations for the relevant parameters are presented below.

The Reynolds number (Re) is calculated by Equation (4).

$$\text{Re} = \frac{\rho u D}{\mu} \quad (4)$$

The local Nusselt number (Nu_x) (Eq. 5) and the average Nusselt number (Nu) (Eq. 6) are described as follows [14]:

$$\text{Nu}_x = \frac{q'' D}{k_f (\bar{T}_{w,x} - \bar{T}_{b,x})} \quad (5)$$

$$\text{Nu} = \frac{1}{L} \int_0^L \text{Nu}_x dx \quad (6)$$

Here, q'' is the heat flux, k_f is the thermal conductivity of the fluid, D is the duct diameter, L is the duct length. T_w is the wall temperature of the duct and T_b is the film temperature of the fluid.

The film temperature of the fluid, T_b is computed by Equation (7).

$$T_b = \frac{(T_{in} + T_{out})}{2} \quad (7)$$

The thermal enhancement factor (η) calculated depending on the Nusselt number is defined by Equation (8) [14].

$$\eta = \frac{\text{Nu}_b}{\text{Nu}_s} \quad (8)$$

Here, Nu_b is Nu for the nanofluid in the channel with baffles, and Nu_s is the Nu for the base fluid in the channel with baffles.

The friction factor (f) is found by Equation (9) [14].

$$f = \frac{\Delta P D}{0.5 \rho u^2 L} \quad (9)$$

Here, ΔP denotes the pressure difference between the inlet and outlet of the duct.

The relative friction factor (r) calculated depending on the friction factor is obtained by Equation (10) [14]:

$$r = \frac{f_b}{f_s} \quad (10)$$

Here, f_b is friction factor calculated for the nanofluid in the channel with baffles, and f_s is the friction factor for the basic fluid in the channel with baffles.

The ratio of thermal enhancement to the relative friction factor is defined as the performance evaluation criterion (PEC) and is represented by Equation (11) [4, 14].

$$\text{PEC} = \frac{(\text{Nu}_b/\text{Nu}_s)}{(f_b/f_s)^{1/3}} \quad (11)$$

The numerical model and mesh structure were created by the Gambit software and the element structure of the numerical model with different baffle angles is presented in Figure 2.

Numerical solutions were performed with FLUENT 15.0 [38] solver and iterations were solved with SIMPLE (Semi-Implicit Method for Pressure-Linked Equations) algorithm. A second-order upwind scheme was used to discretize the convection and diffusion terms. The convergence criterion was set as 10^{-6} for all equations. No problem was observed during the calculations for the accepted convergence criterion.

To determine that the solutions are not affected by the number of elements, grid independence testing was applied and Nusselt numbers were calculated for different element numbers. The element numbers 104298, 162864, 198974, 235724, and 284168 were applied to the numerical model at $\text{Re}=600$ and $\text{Re}=1000$ for $\alpha = 150^\circ$ and base fluid. As a result of the grid independence testing, 198974 element numbers were adapted to the numerical model. The variation of the Nusselt numbers with the element numbers is shown in Figure 3 at different Reynolds number ($\text{Re}=600$ and $\text{Re}=1000$).

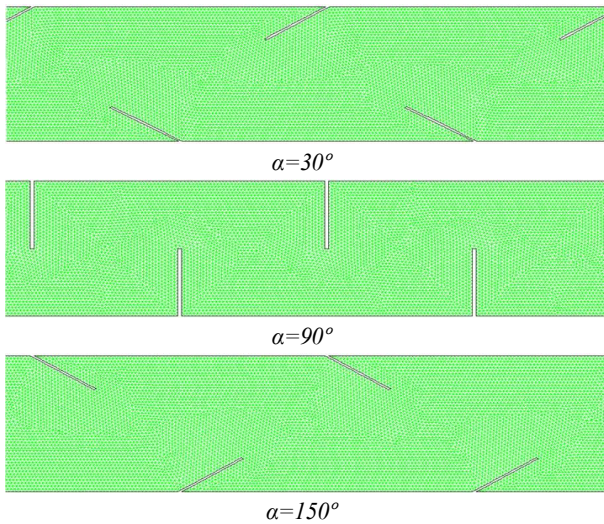
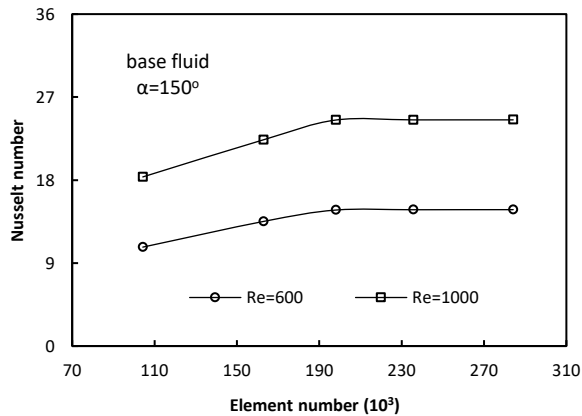


Figure 2. Mesh structures of the numerical model

Figure 3. Variation of Nusselt numbers with element numbers for base fluid at Re=600 and Re=1000 ($\alpha=150^\circ$)

2.3 Thermophysical Properties of Nanofluid

It is assumed that the nanoparticles are homogeneously dispersed in the base fluid. From the thermophysical properties of CuO-water nanofluid, the density was calculated by Equation (12) and the specific heat by Equation (13) [39], the thermal conductivity was calculated by Equation (14) and the viscosity by Equation (15) [40]. The basic fluid is water. Thermo-physical properties of CuO nanoparticle and H₂O are showed in Table 1 [6]. The thermophysical properties were considered constant.

$$\rho_{nf} = (1 - \phi)\rho_{bf} + \phi\rho_{pt} \quad (12)$$

$$C_{nf} = \frac{(1 - \phi)\rho_{bf}C_{bf} + \phi\rho_{pt}C_{pt}}{\rho_{nf}} \quad (13)$$

$$k_{nf} = k_{bf} \frac{[k_{pt} + 2k_{bf} - 2\phi(k_{bf} - k_{pt})]}{[k_{pt} + 2k_{bf} + \phi(k_{bf} - k_{pt})]} \quad (14)$$

$$\mu_{nf} = \mu_{bf}[123\phi^2 + 7.3\phi + 1] \quad (15)$$

Table 1. Thermo-physical properties of CuO nanoparticle and water

	Density [kg/m ³]	Specific heat [J/kgK]	Thermal conductivity [W/mK]	Viscosity [kg/ms]
H ₂ O	998	4182	0.613	0.001003
CuO	6500	533	17.65	-

2.4 Boundary Conditions

The inlet temperature of the nanofluid to the channel is $T_{in} = 293K$. The “velocity inlet” and “outflow” boundary conditions are used at the entrance and exit of the duct, respectively. The walls of the duct containing the baffles are protected at $T_w = 340K$. The adiabatic and non-slip boundary conditions are applied for the baffles. The non-slip and adiabatic boundary conditions are defined for the straight sections at the inlet of the duct and the walls of duct consisting baffles.

3. Result and Discussion

The numerical results of the present study were compared to the results of the experimental work realized by Meyer and Abolarin [41]. For this purpose, the heat transfer coefficient, h (W/m²K) were calculated along x/D distances in a straight duct with circular cross section of $D = 19$ mm diameter for $Re = 1331$ and $q'' = 2kW$ constant heat flux. The results of both studies were given in Figure 4.

In this section, the friction factor and heat transfer of CuO-water nanofluid at different particle volume fractions in a circular cross-section duct in which baffles are placed at different angles are investigated for the range of $200 \leq Re \leq 1000$. To determine the impacts of these parameters on friction factor and thermal performance, the velocity structures, vorticity magnitudes and temperature contours in the duct were obtained.

Figure 5 presents the velocity structures (a), temperature fields (b), and vorticity contours (c) obtained for different Re at $\alpha = 30^\circ$ baffle angle and a constant particle volume fraction ($\phi = 0.03$).

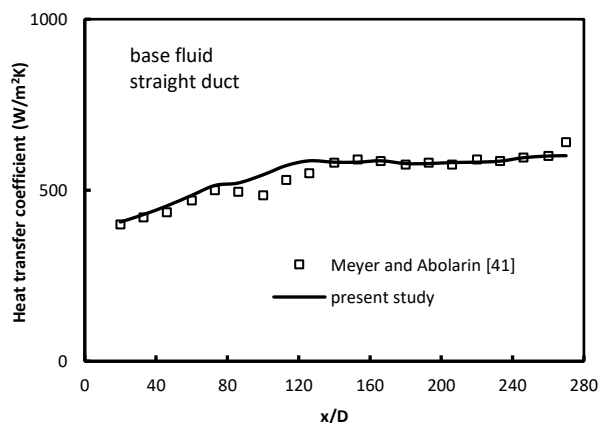


Figure 4. Validity of the numerical solutions (for base fluid)

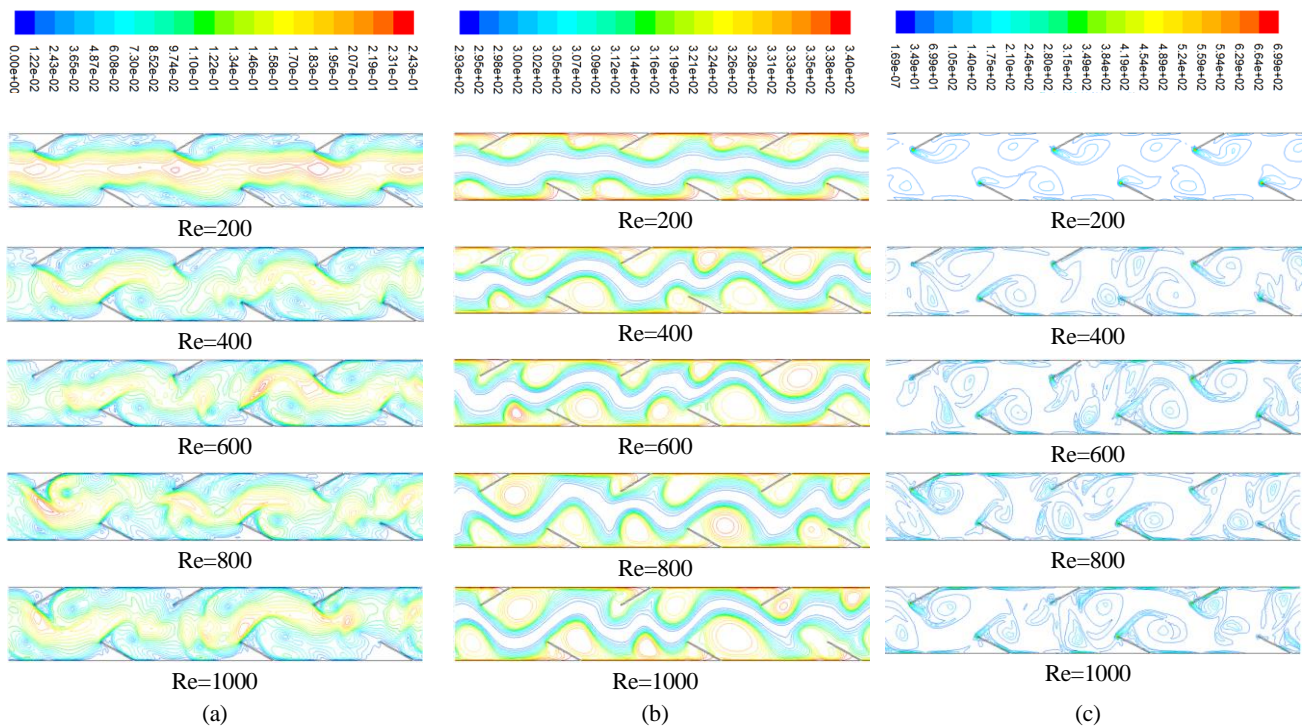


Figure 5. The velocity fields (a), the temperature contours (b), the vorticity magnitudes (c) with different Re at $\phi = 0.03$, $\alpha = 30^\circ$

The velocity fields (Figure 5a) indicate that an oscillation has occurred in the flow due to baffles within the channel. It is seen that the main stream flows as a whole at low Reynolds number, and the separations happen in the flow with the increment in Re. It is indicated that the flow loops occur between each baffle. Increasing the channel inlet velocity causes the flow loops formed in the channel and these structures improve the flow mixing (Figure 5c). Periodic

repetition of this situation after each baffle ensures constant contact of the cold fluid layer in the center of the duct with the warmer fluid layer near the duct walls. Thus, the temperature of the channel surfaces that is in more contact with the cold fluid decreases. With increasing Reynolds numbers, the temperature of the channel surfaces decreased considerably and the heat transfer improved (Figure 5b).

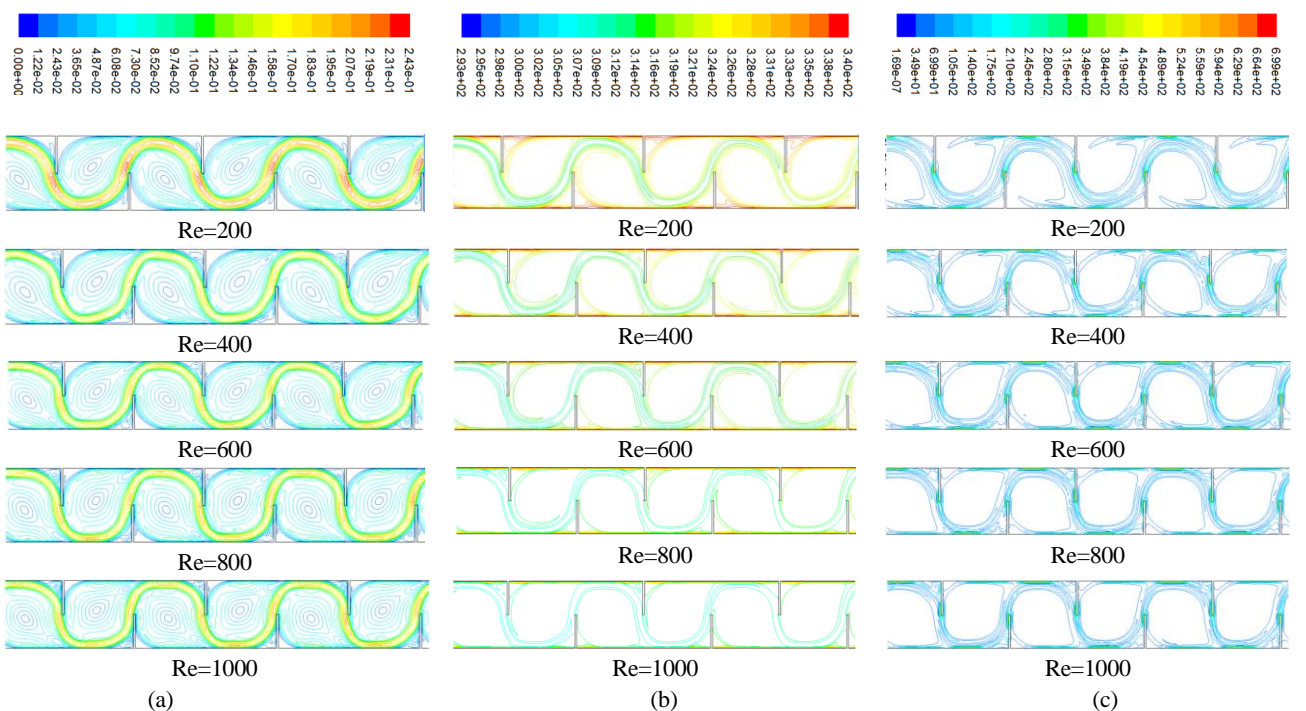


Figure 6. The velocity structures (a), the temperature contours (b), the vorticity fields (c) with different Re at $\phi = 0.03$ and $\alpha = 90^\circ$

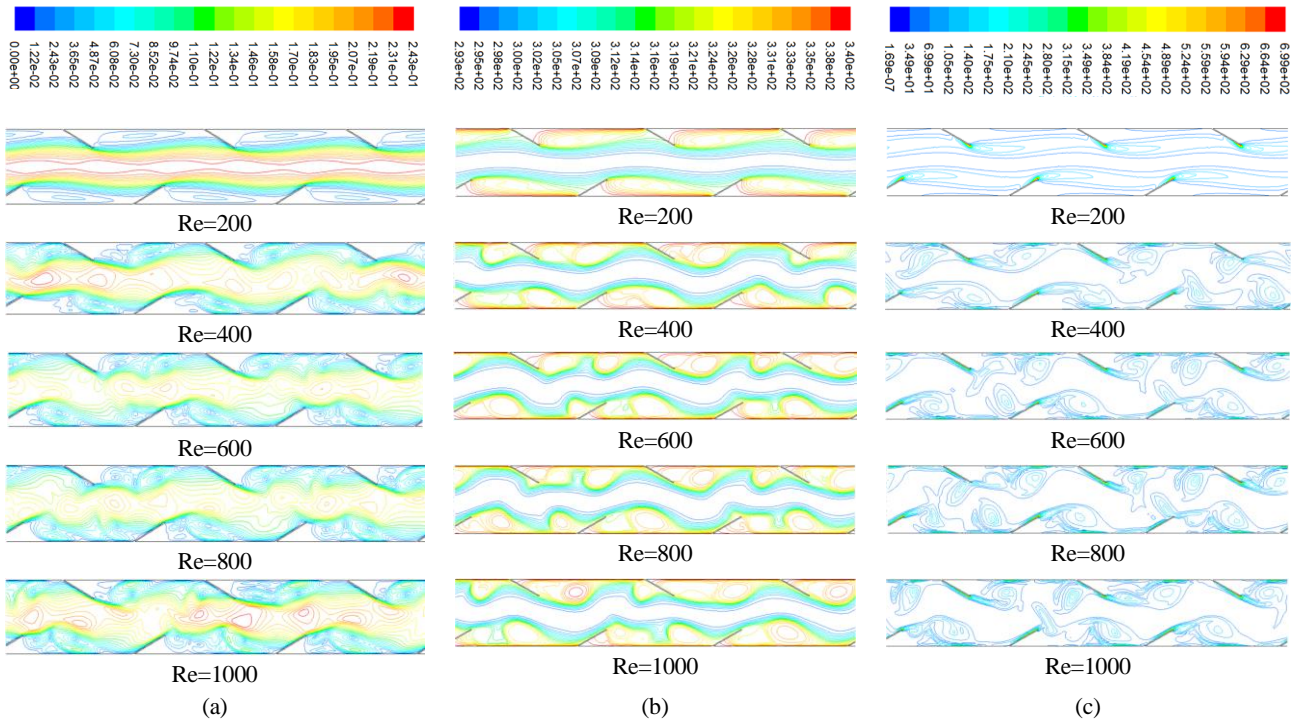


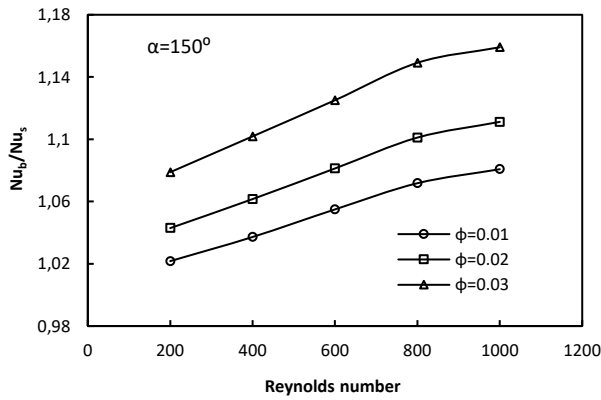
Figure 7. The velocity structures (a), the temperature fields (b), the vorticity contours (c) with different Re at $\phi = 0.03$, $\alpha = 150^\circ$

Figure 6 shows the velocity structures (a), temperature fields (b), and vorticity contours (c) obtained for different Re at $\phi = 0.03$ and $\alpha = 90^\circ$ baffle angle. It is observed that the flow and temperature structures are quite different according to $\alpha=30^\circ$ baffle angle. The flow structure maintains its integrity in all studied Re. Due to the vertical baffles, the main flow contacts the walls of the duct (Figure 6a). Large recirculation zones are formed between each vertical baffle (Figure 6c). With these cycles, the fluid layer close to the hot channel surfaces is transported to the channel center. Thus, the cold fluid layer replacing the hot fluid layer causes the channel surfaces to cool. The heat transfer rate will increase due to increasing inertia forces and mass flow rate with increasing channel velocity. It is observed that the temperature gradient on the channel surfaces decreases significantly with increasing Re (Figure 6b).

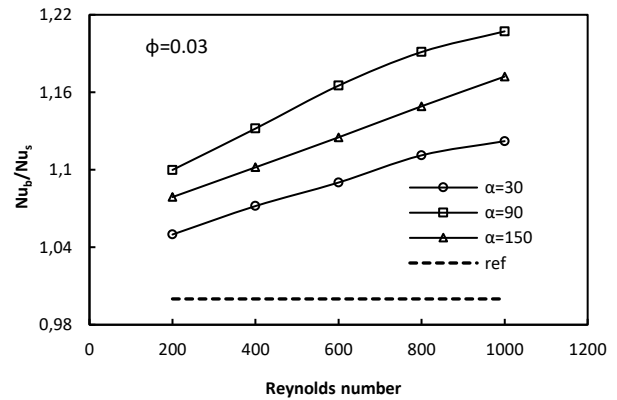
Figure 7 shows the velocity contours (a), temperature fields (b), and vorticity magnitudes (c) obtained for different Re at $\phi = 0.03$ and $\alpha = 150^\circ$ baffle angle. It is seen that the integrity of the main flow structure is not disturbed in all studied Re. The main flow flows as a whole and shows that there are no breaks in the stream. The flow oscillations increase with increasing Re (Figure 7a). It is observed that the flow loops formed longitudinally in the flow direction at low Re, grow transversely between both baffles at high Re and become concentrated all over the channel (Figure 7c). The deterioration of the velocity and thermal boundary layers formed on the channel surfaces due to the baffles diminish the thermal resistance and thus heat transfer is improved. As with other baffle angles,

increasing Re at $\alpha = 150^\circ$ baffle angle increases the heat transfer by decreasing the surface temperature (Figure 7b).

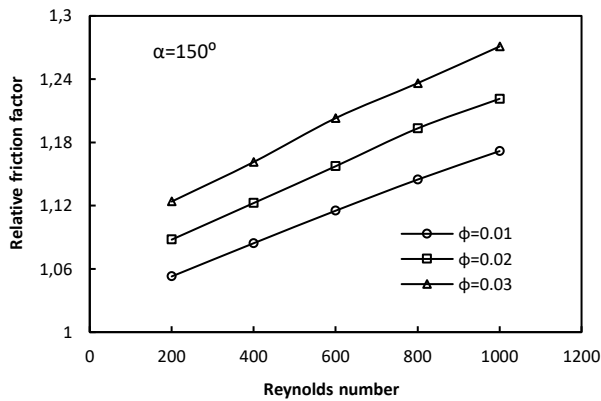
Figure 8 shows the variation of thermal enhancement factor, η (a), relative friction factor, r (b), and performance evaluation criterion (PEC) (c) with Re at different particle volume fractions for $\alpha = 150^\circ$ baffle angle. Thermal enhancement factor increases with increasing the ϕ and Re. It was observed that thermal enhancement factor increased faster in the range of $200 \leq Re \leq 800$ for all tested ϕ , and increased more slowly after $Re \geq 800$. Because the Nu_s value also increases at high Re ($Re \geq 800$). The highest thermal enhancement factor for $\alpha = 150^\circ$ baffle angle was obtained to be about 1.16 at $Re = 1000$ and $\phi = 0.03$. At $Re=1000$, the thermal enhancement factors for $\phi = 0.02$ and $\phi = 0.01$, were found to be approximately 1.11 and 1.08 respectively (Figure 8a). The relative friction factor increases with increasing ϕ and Re. Pressure loss increases due to the fact that the viscosity of the nanofluid is higher than the base fluid. Moreover, the baffles added to the duct surfaces restrict the flow area. This case increases friction loss. The highest relative friction factor for $\alpha = 150^\circ$ baffle angle was obtained as 1.28 at $Re = 1000$ and $\phi = 0.03$. At $\alpha = 150^\circ$ and $Re = 1000$, the relative friction factor for $\phi = 0.02$ and $\phi = 0.01$, were found to be about 1.22 and 1.17, respectively (Figure 8b). The PEC increases with increasing Re and ϕ . A slight peak occurred at $Re = 800$ for all particle volume fraction. Because after $Re = 800$, the thermal enhancement factor increases more slowly and the friction factor increases more.



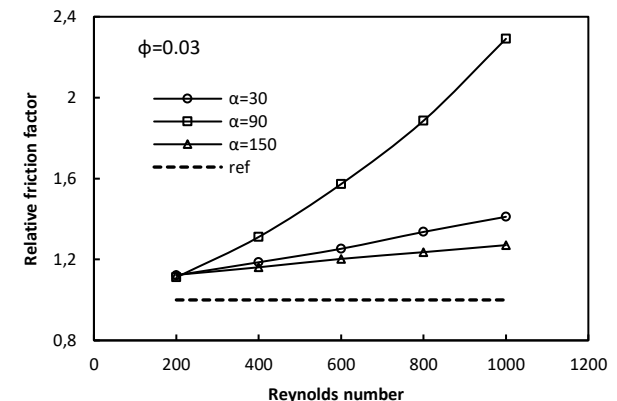
(a)



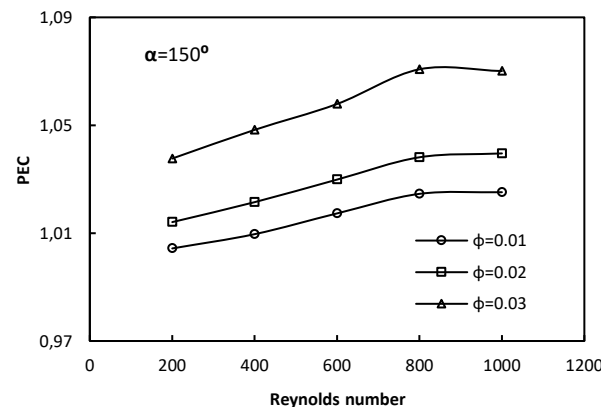
(a)



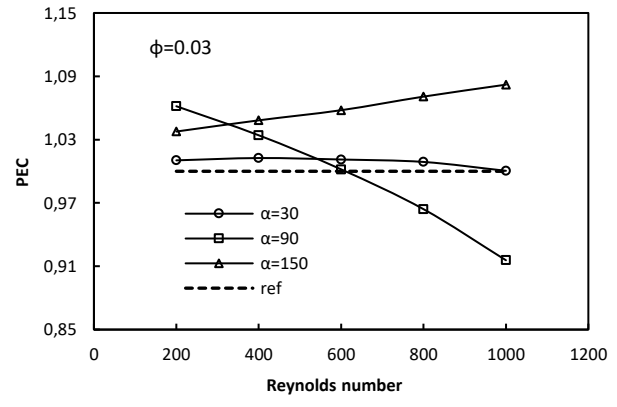
(b)



(b)



(c)



(c)

Figure 8. Thermal enhancement factor (a), relative friction factor (b), and PEC (c) with Re and different particle volume fractions at $\alpha = 150^\circ$

Figure 9. Thermal enhancement factor (a), relative friction factor (b), and PEC (c) with Re and different baffle angles at $\phi = 0.03$.

The highest PEC for $\alpha = 150^\circ$ baffle angle was found to be 1.07 at $Re = 800$ and $\phi = 0.03$. At $\alpha = 150^\circ$ and $Re = 1000$, the PEC for $\phi = 0.02$ and $\phi = 0.01$, were acquired to be about 1.04 and 1.00, respectively (Figure 8c). Due to the nanosized particles added to the basic fluid and the baffles added to the channel surface, significant improvement in heat transfer is achieved, but an acceptable increase in surface friction is also observed.

Figure 9 shows the variation of thermal enhancement factor (a), relative friction factor (b), and PEC (c) with Reynolds numbers at different baffle angles for $\phi = 0.03$.

The dashed straight line represents the base fluid flow in the duct with baffles at the same geometry and is taken as a reference. Thermal enhancement increases with increasing Re. The highest thermal enhancement factor occurs at $\alpha = 90^\circ$ baffle angle, followed by $\alpha = 150^\circ$ and $\alpha = 30^\circ$ baffle angles. The highest thermal enhancement was found to be 1.21 at $Re = 1000$ and $\phi = 0.03$ for $\alpha = 90^\circ$. At $Re = 1000$, the thermal enhancement for $\alpha = 30^\circ$ and $\alpha = 150^\circ$ were found to be about 1.16 and 1.12, respectively (Figure 9a). The relative friction factor increases with increasing Re. It is seen that the lowest friction factor is obtained at $\alpha = 150^\circ$ baffle angle, followed by $\alpha = 30^\circ$ and $\alpha = 90^\circ$ baffle angles. Relative friction factor increases dramatically with increasing Re at $\alpha = 90^\circ$ baffle

angle compared to other angles. This is because vertical baffles highly restrict the flow area. The highest relative friction factor was found to be 2.29 at $Re = 1000$ and $\phi = 0.03$ for $\alpha = 90^\circ$. At $\phi = 0.03$ and $Re = 1000$, the relative friction factor for $\alpha = 30^\circ$ and $\alpha = 150^\circ$ were obtained to be about 1.41 and 1.27, respectively (Figure 9b). The PEC variation differs in all three baffle angles for $\phi = 0.03$. The PEC values were obtained close to the reference value in all studied Re at $\alpha = 30^\circ$ baffle angle. At $\alpha = 150^\circ$ baffle angle, the PEC increases with increasing Re . The reason for this is that the relative friction factor increases less at $\alpha = 150^\circ$ baffle angle than at other angles. At $\alpha = 90^\circ$ baffle angle, the PEC values decrease dramatically with increasing Re . The reason for this is that the relative friction factor increases more than the thermal enhancement at the $\alpha = 90^\circ$ baffle angle. The best PEC was acquired to be about 1.08 at $Re = 1000$ and $\phi = 0.03$ for $\alpha = 150^\circ$ (Figure 9c).

This study summarizes that due to nanoparticles added to the base fluid and baffles added to the duct surface, significant improvement in heat transfer is achieved, but an acceptable increase in friction factor is observed.

4. Conclusions

In present study, the flow and thermal improvement of CuO-water nanofluid were numerically investigated for different particle volume fractions in a circular duct in which baffles were placed at different angles. The effects of baffle angles, particle volume fractions and Re on friction factor and thermal enhancement factor were examined. The velocity structures, vorticity contours and temperature fields were obtained for different parameters in the duct. In numerical simulations, it has been observed that the flow structure and temperature contours were significantly affected by the baffle angles and Re . It was determined that nanoparticle volume fractions and baffle angles have a significant potential in heat transfer improvement according to laminar flow regime. The findings indicated that the thermal enhancement factor increased considerably with a slight friction factor with increasing Re and ϕ . It was determined that the baffle angles have different effects in terms of friction factor and heat transfer. The highest thermal enhancement factor and relative friction factor were obtained at $\alpha = 90^\circ$ baffle angle. The best performance evaluation criteria value was acquired at $\alpha = 150^\circ$. This study shows that baffles inserted into duct have an important potential to improve heat transfer under nanofluid flow if an appropriate baffle angle is used.

Declaration

The authors declared no potential conflicts of interest with respect to the research, authorship, and/or publication of this article. The authors also declared that this article is original, was prepared in accordance with international publication and research ethics, and ethical committee

permission or any special permission is not required.

Author Contributions

S. Akçay studied on methodology, analysis, verification, writing and review of the manuscript. U. Akdag supervised, reviewed and edited the study.

Nomenclature

C	: Specific heat [J/kgK]
D	: Duct diameter [m]
H	: Baffle length [m]
k	: Thermal conduction [W/mK]
L_1	: Unheated channel length [m]
L_2	: Baffled channel length [m]
Nu	: Nusselt number [$Nu = hL/k$]
P	: Pressure [Pa]
Pr	: Prandtl number [$Pr = \mu C_p/k$]
r	: Relative friction factor [$r = f_b/f_s$]
Re	: Reynolds number [$Re = uD/\nu$]
S	: Distance between baffles [m]
t	: Thickness of the baffles [m]
T_{in}	: Inlet temperature of fluid [K]
T_{out}	: Outlet temperature of fluid [K]
T_w	: Surface temperature of the duct [K]
u, v	: Velocity components [m/s]
η	: Thermal enhancement factor [$\eta = Nu_b/Nu_s$]
μ	: Dynamic viscosity [Pas]
ρ	: Fluid density [kg/m^3]
ν	: Kinematic viscosity [m^2/s]
ϕ	: Nanoparticle volume fraction [%]
b	: nanofluid flow in the duct with baffles
bf	: base fluid
nf	: nanofluid
pt	: particle
s	: base fluid flow in the duct with baffles
w	: wall

References

- Menni, Y., A. Azzi, and A. Chamkha, *Enhancement of convective heat transfer in smooth air channels with all-mounted obstacles in the flow path: A review*. Journal of Thermal Analysis and Calorimetry, 2019. **135**: p. 1951-1976.
- Ekiciler, R., M.S.A. Çetinkaya, and K. Arslan, *Effect of shape of nanoparticle on heat transfer and entropy generation of nanofluid-jet impingement cooling*. International Journal of Green Energy, 2020. **17**(10): p. 555-567.
- Husain, S., S.A. Khan, and M.A. Siddiqui, *Wall boiling of Al_2O_3 -water nanofluid: Effect of nanoparticle concentration*. Progress in Nuclear Energy, 2021. **133**: p. 103614.
- Altun, A. H., H. Nacak, and E. Canli, *Effects of trapezoidal and twisted trapezoidal tapes on turbulent heat transfer in tubes*. Applied Thermal Engineering, 2022. **211**: p. 118386.
- Akdag, U., S. Akçay, and D. Demiral, *Heat transfer enhancement with laminar pulsating nanofluid flow in a wavy channel*. International Communications in Heat and

- Mass Transfer, 2014. 59: p. 17–23.
6. Arslan, K. and R. Ekiciler, *Effects of SiO₂/water nanofluid flow in a square cross-sectioned curved duct*. European Journal of Engineering and Natural Sciences, 2019. 3(2): p. 101-109.
 7. Akdag, U., S. Akçay, and D. Demiral, *Heat transfer in a triangular wavy channel with CuO-water nanofluids under pulsating flow*. Thermal Science, 2019. 23(1): p. 191-205.
 8. El Habet, M.A., S.A. Ahmed, and M.A. Saleh, *The effect of using staggered and partially tilted perforated baffles on heat transfer and flow characteristics in a rectangular channel*. International Journal of Thermal Sciences, 2022. 174: p. 107422.
 9. Kilic, M., M. Yavuz, and I.H., Yilmaz, *Numerical investigation of combined effect of nanofluids and impinging jets on heated surface*. International Advanced Researches and Engineering Journal, 2018. 2(1): p. 14-19.
 10. Li, Z. and Y. Gao, *Numerical study of turbulent flow and heat transfer in cross corrugated triangular ducts with delta-shaped baffles*. International Journal of Heat and Mass Transfer, 2017. 108: p. 658–670.
 11. Sriromreun, P., *Numerical study on heat transfer enhancement in a rectangular duct with incline shaped baffles*. Chemical Engineering Transactions, 2017. 57: p. 1243–1248.
 12. Mellal, M., R. Benzeguir, D. Sahel, and H. Ameer, *Hydro-thermal shell-side performance evaluation of a shell and tube heat exchanger under different baffle arrangement and orientation*. International Journal of Thermal Sciences, 2017. 121: p. 138-149.
 13. Ekiciler, R. and M.S.A. Çetinkaya, *A comparative heat transfer study between monotype and hybrid nanofluid in a duct with various shapes of ribs*. Thermal Science and Engineering Progress, 2021. 23: p. 100913.
 14. Akçay, S., *Numerical analysis of heat transfer improvement for pulsating flow in a periodic corrugated channel with discrete V-type winglets*. International Communications in Heat and Mass Transfer, 2022. 134: p. 105991.
 15. Ameer, H., *Effect of Corrugated Baffles on the Flow and Thermal Fields in a Channel Heat Exchanger*. Journal of Applied and Computational Mechanics, 2020. 6(2): p. 209-218.
 16. Menni, Y., A. Azzi, and A. Chamkha, *Modeling and analysis of solar air channels with attachments of different shapes*. International Journal of Numerical Methods for Heat & Fluid Flow, 2019. 29(5): p. 1815-1845.
 17. Menni, Y., M. Ghazvini, H. Ameer, M.H. Ahmadi, M. Sharifpur, and M. Sadeghzadeh, *Numerical calculations of the thermal-aerodynamic characteristics in a solar duct with multiple V-baffles*. Engineering Application of Computational Fluid Mechanics, 2020. 14(1): p. 1173–1197.
 18. Salhi, J.E., T. Zarrouk, N. Hmidi, M. Salhi, N. Salhi, and M. Chennaif, *Three-dimensional numerical analysis of the impact of the orientation of partially inclined baffles on the combined mass and heat transfer by a turbulent convective airflow*. International Journal of Energy and Environmental Engineering, Published online 01 June 2022. <https://doi.org/10.1007/s40095-022-00505-5>.
 19. Salhi, J.E., T. Zarrouk, and N. Salhi, *Numerical study of the thermo-energy of a tubular heat exchanger with longitudinal baffles*. Materials Today: Proceedings, 2021. 45: p. 7306–7313.
 20. Nedunchezhiyan, M., R. Karthikeyan, S. Ramalingam, D. Damodaran, J. Ravikumar, S. Sampath, and G. Kaliyaperumal, *Influence of baffles in heat transfer fluid characteristics using CFD evaluation*. International Journal of Ambient Energy, 2022. p. 1–29 <https://doi.org/10.1080/01430750.2022.2063175>.
 21. Razavi, S.E., T. Adibi, and S. Faramarzi, *Impact of inclined and perforated baffles on the laminar thermo-flow behavior in rectangular channels*. SN Applied Sciences, 2020. 2:284, <http://doi.org/10.1007/s42452-020-2078-8>.
 22. El Habet, M.A., S.A. Ahmed, and M.A. Saleh, *Thermal/hydraulic characteristics of a rectangular channel with inline/staggered perforated baffles*. International Communications in Heat Mass Transfer, 2021. 128: p. 105591.
 23. Manca O., S. Nardini, and D. Ricci, *A numerical study of nanofluid forced convection in ribbed channels*. Applied Thermal Engineering, 2012. 37: p. 280-297.
 24. Sriromreun, P., C. Thianpong, and P. Promvong, *Experimental and numerical study on heat transfer enhancement in a channel with Z-shaped baffles*. International Communications in Heat and Mass Transfer, 2012. 39(7): p. 945–952.
 25. Turgut, O. and E. Kızıllırmak, *Effects of Reynolds number, baffle angle, and baffle distance on 3-d turbulent flow and heat transfer in a circular pipe*. Thermal Science, 2015. 19(5): p. 1633-1648.
 26. Promvong, P., S. Tamna, M. Pimsarn, and C. Thianpong, *Thermal characterization in a circular tube fitted with inclined horseshoe baffles*. Applied Thermal Engineering, 2015. 75: p. 1147–1155.
 27. Kumar, R., A. Kumar, R. Chauhan, and M. Sethi, *Heat transfer enhancement in solar air channel with broken multiple V-type baffle*. Case Studies Thermal Engineering, 2016. 8: p. 187–197.
 28. Sahel, D., H. Ameer, R. Benzeguir, and Y. Kamla, *Enhancement of heat transfer in a rectangular channel with perforated baffles*. Applied Thermal Engineering, 2016. 101: p. 156–164.
 29. Jung, S.Y. and H. Park, *Experimental investigation of heat transfer of Al₂O₃ nanofluid in a microchannel heat sink*. International Journal of Heat and Mass Transfer, 2021. 179: p. 121729.
 30. Akdag, U., S. Akçay, and D. Demiral, *Heat transfer enhancement with nanofluids under laminar pulsating flow in a trapezoidal-corrugated channel*. Progress in Computational Fluid Dynamics, An International Journal, 2017. 17(5): p. 302-312.
 31. Akçay, S. *Investigation of thermo-hydraulic performance of nanofluids in a zigzag channel with baffles*. Adiyaman University Engineering Sciences Journal, 2021. 15: p. 525-534.
 32. Akçay, S. *Numerical Analysis of Hydraulic and Thermal Performance of Al₂O₃-Water Nanofluid in a Zigzag Channel with Central Winglets*. Gazi University Journal of Science, 2023. 36(2): in press.
 33. Heshmati, A., H.A. Mohammed, and A.N. Darus, *Mixed convection heat transfer of nanofluids over backward facing step having a slotted baffle*. Applied Mathematics and Computation, 2014. 240: p. 368–386.
 34. Alnak, D.E., *Thermohydraulic performance study of different square baffle angles in cross-corrugated channel*. Journal of Energy Storage, 2020. 28: p. 101295.
 35. Ajeel, R.K., K. Sopian, and R. Zulkifli, *Thermal-hydraulic performance and design parameters in a curved-corrugated*

- channel with L-shaped baffles and nanofluid*. Journal of Energy Storage, 2021. **34**: p. 101996.
36. Menni, Y., A.J. Chamkha, M. Ghazvini, M.H. Ahmadi, H. Ameer, A. Issakhov, and M. Inc, *Enhancement of the turbulent convective heat transfer in channels through the baffling technique and oil/multiwalled carbon nanotube nanofluids*. Numerical Heat Transfer, Part A: Applications, 2021. **79**(4): p. 311-351.
 37. Canli, E., Ates, A. and Bilir, S. Derivation of *dimensionless governing equations for axisymmetric incompressible turbulent flow heat transfer based on standard k-ε model*. Afyon Kocatepe University Journal of Science and Engineering, 2020; **20**(6): p. 1096-1111.
 38. ANSYS Fluent user guide & theory guide-Release 15.0, 2015, USA: Fluent Ansys Inc.
 39. Pak, B. and Y.I. Cho, *Hydrodynamic and heat transfer study of dispersed fluids with submicron metallic oxide particles*. Experimental Heat Transfer, 1998. **11**(2): p. 151–170.
 40. Kakac, S. and A. Pramuanjaroenkij, *Review of convective heat transfer enhancement with nanofluids*. International Journal of Heat and Mass Transfer, 2009. **52**: p. 3187–3196.
 41. Meyer, J.P. and S.M. Abolarin, *Heat transfer and pressure drop in the transitional flow regime for a smooth circular tube with twisted tape inserts and a square-edged inlet*. International Journal of Heat and Mass Transfer, 2018. **117**: p. 11-29.



Research Article

Experimental analysis of a transcritical heat pump system with CO₂ refrigerant

Ahmet ELBİR ^{a,*} , Hilmi Cenk BAYRAKÇI ^b , Arif Emre ÖZGÜR ^b  and
Özdemir DENİZ ^b 

^aSüleyman Demirel University, Renewable Energy Resources Research Center, 32260, Isparta/Turkey

^bIsparta University of Applied Sciences, Faculty of Technology, 32260, Isparta/Turkey

ARTICLE INFO

Article history:

Received 20 June 2022

Accepted 23 November 2022

Published 15 December 2022

Keywords:

Capillary tube

CO₂

Energy efficiency

EPC

Exergy efficiency

Heat pump

Transcritical

ABSTRACT

Today, it is seen that increasing environmental pollution is getting ahead of the increasing energy need. Therefore, more environmentally friendly and more economical refrigerants are needed. In this context, carbon dioxide appears as a natural refrigerant in cooling systems and heat pump (HP) systems, and it has been widely used in recent years. In this study, a single-stage heat pump system with a CO₂ refrigerant, with a transcritical cycle, has been experimentally studied. The system is designed as a water-to-water heat pump. The performance of the system has been determined experimentally. In the system, capillary pipes with a diameter of 2.00 mm and two different lengths are used. It is aimed to create different evaporation pressures with two capillary tubes. The first capillary tube is 2.40 m long and the second is 1.20 m long. Gas cooler pressures, gas cooler and evaporator cooling water mass flow rates were kept the same for both cases. A certain gas charge was made and measurements were made for both cases. Thermodynamic analysis and comparison of the system were made. In the short capillary tube system, it was observed that the COP_{HP} value was 7.2% higher, the CO₂ mass flow rate increased by 9.1% to achieve the same gas refrigerant pressure value, and the power consumption in the compressor decreased by 1.8%. In addition, the gas cooler outlet temperature, the evaporator outlet temperature and the change in ambient temperatures, as well as the exergetic destruction and exergetic efficiencies in the system and system components are presented in figures with EES.

1. Introduction

Heat pump systems, which have become very competitive in domestic uses, needed alternative, innovative and most importantly environmentally friendly refrigerants that do not harm the ozone layer. In line with these needs, the depletion potential of the ozone layer (ODP=0) and global warming potential (GWP=1), and carbon dioxide (CO₂), a natural refrigerant, have inspired our studies in recent years. In our studies, a capillary tube was used for the expansion valve, which is one of the main components used in a heat pump system. Many elements such as electronic valve, thermostatic valve and capillary pipe are used in the expansion process. The most important reason why we chose the capillary tube in this study is that it is cheap and easy to find. In this context, it is important to determine the operating temperature and conditions of

the systems to be installed and to choose the appropriate capillary tube according to the need.

Some studies in the literature; Elbir et al., They presented with graphics and pictures how the test results will change according to the thermodynamic rules in the same system and with which elements they will change when the gas cooler pressure of 75 bar is increased to 100 bar gas cooler pressure and the mass flow rate of the water providing cooling from water to water is increased [1]. Jadhav and Agrawal., calculated the effect of various geometric parameters such as tube diameter, length, roughness and slope on mass flow rate, cooling capacity and COP [2]. Jadhav and Agrawal., found that the percentage decrease in mass flow rate increased as the pipe diameter and the length of the helical capillary pipe increased [3]. Rocha et al., investigated the effect of surface roughness on mass flow rate from adiabatic capillary tubes in their study [4]. Wang et al., stated that

* Corresponding author. Tel.: +90-246-2111529.

E-mail addresses: ahmetelbir@sdu.edu.tr (A.Elbir), cenkbayrakci@isparta.edu.tr (H. C. Bayrakci), emreozgur@isparta.edu.tr (A. E. Özgür), ozdemirdeniz@isparta.edu.tr (Ö. Deniz)

ORCID: 0000-0001-8934-7665 (A.Elbir), 0000-0001-5064-7310 (H. C. Bayrakci), 0000-0001-6382-5462 (A. E. Özgür), 0000-0002-8168-9668 (Ö. Deniz)

DOI: [10.35860/iarej.1132994](https://doi.org/10.35860/iarej.1132994)

© 2022, The Author(s). This article is licensed under the CC BY-NC 4.0 International License (<https://creativecommons.org/licenses/by-nc/4.0/>).

the refrigerant charge plays an important role in optimizing the system performance [5]. Andres et al., experimentally investigated the optimum operating conditions of the COP value of the subcooled transcritical CO₂ system at different operating pressures. From the experimental data, only two general expressions as a function of the evaporation level and the gas cooler outlet temperature are specified to determine the optimum pressure and subcooling [6]. Song et al., In their work, they experimentally incorporated the variation of the gas refrigerant outlet in a transcritical CO₂ heat pump system using an electronic expansion valve (EEV) and a capillary tube. In terms of performance, they said that the transcritical CO₂ heat pump using capillary tube is promising. [7]. Agrawal et al., studied optimum diameter length and diameter correlation. They said the pressure gradient is significantly higher for CO₂ than with conventional refrigerants, with a shorter capillary tube length [8]. Wang et al., They calculated the optimal combination of capillary tube size and refrigerant charge and made the experimental comparison in their study. In the experiment, they said that the length of the capillary tube was shortened by 8.77% and the optimum refrigerant charge increased by about 5%. In the experimental study, they focused on how the reduction of refrigerant charge can affect the coefficient of heating performance [9]. Agrawal and Bhattacharyya, Instead of an expansion valve, a capillary tube was proposed, and optimum operating conditions were investigated. Optimal conditions of gas refrigerant pressure were investigated, and their effect on COP value was investigated. They made recommendations on the most appropriate diameter and length [10]. Song et al., In the system they designed, they compared the transcritical CO₂ heat pump system, which is dependent on the gas cooler outlet temperature, using both an electronic expansion valve (EEV) and a capillary tube. They said that the results obtained with the capillary tube obtained close results in the heat pump system using EEV[11]. Agrawal and Bhattacharyya, Parameters that affect system performance have been identified. They emphasized that the temperature of the water entering the gas cooler as a coolant source is more important than the flow rate. They emphasized the effect on system performance by determining the optimum gas charge and optimum capillary tube [12]. Wang and Lu, In their work, they conducted experimental and theoretical studies on the optimization of capillary tube dimensions with gas charge. In the results they determined, it was emphasized that the shortening of the capillary tube length increased the amount of refrigerant. In addition, they made calculations on how the decrease in the amount of refrigerant could reduce the performance of the system [13]. Date et al., In their study, they presented studies on optimum system pressure values and refrigerant amounts in the system using EEV [14]. Jadhav and Agrawal, Thermodynamic

analyses of an adiabatic spiral and a helical capillary tube in a CO₂ transcritical system were performed with the subcritical R22 fluid. They said that the decrease in the mass flow rate of the refrigerant is more pronounced in the spiral capillary tube than in the spiral capillary tube effect [15]. Rocha et al., They developed an algebraic equation and dimensionless correlation for straight capillaries. An algebraic solution for helical capillary tubes in the transcritical CO₂ cycle is highlighted in the literature [16]. Anka et al., They developed alternative methods by using the average of the refrigerant charge amounts in optimum summer and winter conditions and the outdoor temperature that gives the same COP of the IDC (internet data center) cooling system in the refrigerant charge amounts in optimum summer and winter conditions, and made calculations to determine the annual optimum charge of the system [17]. Jadhav et al., In their study, a thermodynamic analysis was carried out for a system with CO₂ refrigerant using straight, spiral, and spiral capillary tubes. It is said that the reduction in mass in the helical capillary tube is less than that in the straight capillary tube. They show that there is a mass reduction in the spiral tube compared to the straight capillary tube. calculated the reduction in mass in a spiral tube compared to a helical capillary tube. The reduction in length in a straight capillary tube and a spiral tube gave the percentage changes presented the relationships between reductions in length in a spiral tube compared to a helical capillary tube [18]. Freegah et al., In their study, they investigated the effect of capillary tube diameter and mass flow rate of the refrigerant on the physical properties of the refrigerant in the capillary tube. They stated that there was a very good agreement between their experimental and numerical results. The results of the first comparison between the physical properties of the capillary tube and the mass flow are emphasized. An increase in the diameter will result in an increase in the length of the capillary tube, and an increase in the mass flow rate will result in a decrease in the length [19]. El Achkar et al., In their work, they designed a system for the analysis of a cooling system working with conventional throttling and capillary injection. They stated that the cooling system is more stable in capillary injection mode, which will reduce the steady-state time and increase the COP value [20]. The purpose of the study is to replace an expansion valve with a capillary tube. It is to reveal how the capillary tubes of different lengths change in the thermodynamic side of the system at constant gas refrigerant pressure.

2. Transcritical Cycle

The refrigerants used today have high critical temperatures, but some of the fluids we use frequently (such as R404A 72°C, R410A 72.13°C and R407C 86.74°C) are higher than that of Carbon Dioxide (R744

31°C). For example, the critical temperature for R134A is 101.1°C, which means that condensation, as well as heat removal from the system, can be at 101.1°C. This temperature is higher than that required for heat dissipation to the atmosphere for almost any refrigeration application. For R744 it means that condensation heat removal can only occur at temperatures up to 31°C. This temperature is much lower than required to evacuate heat to the atmosphere for many refrigeration applications [22].

In conventional heat pump cycles, the heat rejection occurs below the critical point. Cycles that occur below the critical point are called subcritical cycles. It is provided with a condenser in subcritical systems. Due to the critical temperature of CO₂, the heat dissipation process takes place above the critical point. CO₂ performs the heating process above the critical point with a gas cooler. Since the evaporation process takes place below the critical point and the condensation process takes place above the critical point, these cycles are called transcritical cycles. Subcritical and transcritical cycles are shown in Figure 1 [21].

3. Assumptions and Equations

Since the second law of thermodynamics examines the quality of energy as well as its quantity, it is known that it generally gives reliable results in energy analysis. The increase in the efficient use of energy has been made possible by the transition to the concept of exergy. The main purpose of exergy analysis is to use energy in the most efficient way and to see where and how losses occur on system components.

The following assumptions were taken into account while making the thermodynamic analysis of the system.

- Pure substance is used in the system.
- The compression in the compressor is adiabatic.
- The pipes between the system components are well insulated and the internal and external loss of heat transfer from the evaporator and gas cooler is neglected.
- Pressure drops in system components and on the pipeline and the heat transfer process are also neglected.
- The heat exchangers used as evaporators and gas coolers are counter flowing.
- System performance is assumed to be constant and regular.
- It is assumed that the enthalpy is constant throughout the pressure reduction process in the capillary tube.
- The electrical frequency in the system is 50 Hz and the voltage is 220 volts.
- The kg/minute in the refrigerant flow meter is converted to kg/second.
- The electrical power shown in the watt meter was measured by including the circulation pumps. The circulation pump drew 100 watts of power.

•Gravitational potential energy and kinetic energy are not taken into account.

After obtaining the necessary tools and equipment for the establishment of the test system, high pressure endurance tests of the system were carried out and the detection phase of the leaks in the system was completed. In order to remove the moisture formed in the system, the system was vacuumed and kept under vacuum. Finally, the system was made ready by gradually pressing gas, and it was matched with the software of the Danfoss devices used in the system and installed on the computer used for measurement. The obtained results were recorded on the computer and Store View Desktop for Danfoss branded devices and EES engineering software programs were used for energy and exergy analysis of the system [22].

In Figure 2, the drawing of the experimental system for which thermodynamic analysis was made is given [23].

How efficiently the energy in the system is used is determined by Equation (1) COP (heat pump performance coefficient) calculation, \dot{Q}_{gc} , \dot{W}_c and its equation is;

$$COP_{HP} = \frac{\dot{Q}_{gc}}{\dot{W}_c} \quad (1)$$

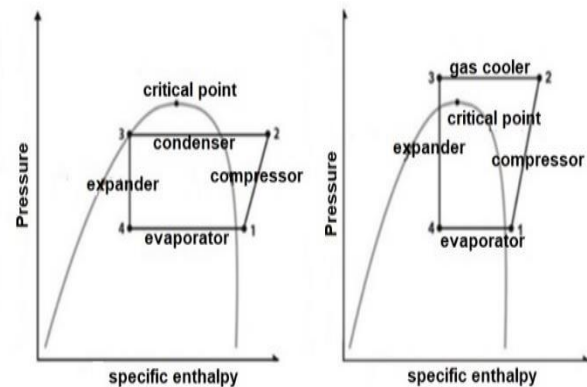


Figure 1. Subcritical and transcritical refrigeration cycle processes [11]

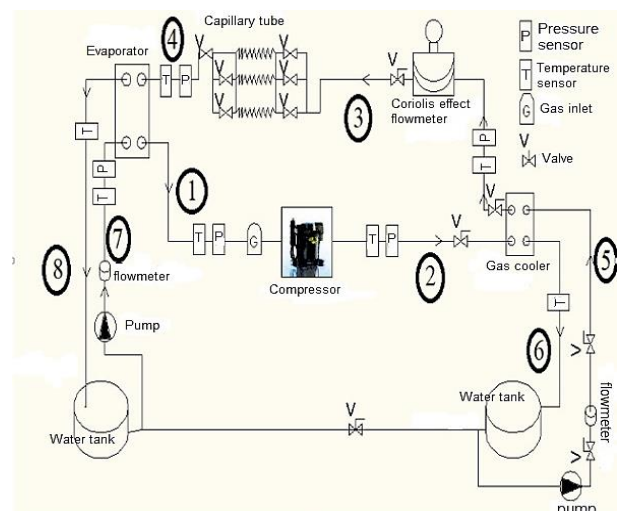


Figure 2. Experiment system with thermodynamic analysis

The temperature values in the system are indicated by T (K), the instantaneous temperature values in the evaporator and the gas cooler in Equation (2) are the temperature values found from the $T_{instantaneous\ temperature}$ ($T_{ins.temp.}$) equation. He calculated separately for carbon dioxide gas and cooling water circulating in the system. It is given in Table 1.

$$T_{ins.temp.} = \frac{h_{in} - h_{out}}{s_{in} - s_{out}} \quad (2)$$

The main purpose of exergy analysis is to use energy in the most efficient way and to see where and how losses occur on system components. Exergy analysis of pure substance;

$$ex=(h-h_0)-T_0(s-s_0) \quad (3)$$

The total exergy destruction for the components is;

$$\dot{E}x = \dot{m} * ex \quad (4)$$

Exergy destruction equation of the total system;

$$\dot{E}x_{total} = \dot{W}_c - \dot{E}x_{ev} \quad (5)$$

Or

$$\dot{E}x_{total} = \dot{E}x_c + \dot{E}x_{gc} + \dot{E}x_v + \dot{E}x_{ev} \quad (6)$$

General exergy efficiency equation;

$$\psi = \frac{\sum useful\ output\ exergy}{\sum input\ exergy} = 1 - \frac{\sum exergy\ loss}{\sum input\ exergy} \quad (7)$$

Heating exergetic efficiency;

$$\psi_{II} = \frac{\dot{E}x_{gc}}{\dot{W}_c} \quad (8)$$

General exergetic coefficient of performance equation for heating; [24]

$$EPC_{HP} = \frac{\psi_{II}}{(1-\psi_{II})} \quad (9)$$

Also, the mass-energy and exergy equations for each part are given in Table 1.

In Figure 3, the closed cycle thermodynamic equations of the system parts are presented in the form of a Table 2. Engineering Equation Solver (EES) program [25] was used for shaping. Variable values of temperature values in their drawings;

- Ambient temperature between 290 K and 305 K
- Evaporator outlet temperature between 290 K and 305 K.
- Gas cooler outlet temperature between 290 K and 305 K.

Table 1. Table representation of system parts in closed cycle thermodynamic equations

Parts	Compressor	Gas cooler	Expansion Valve	Evaporator
Mass Balance	$\dot{m}_1 = \dot{m}_2 = \dot{m}_{CO_2}$	$\dot{m}_2 = \dot{m}_3 = \dot{m}_{CO_2}$ $\dot{m}_5 = \dot{m}_6 = \dot{m}_{H_2O} g/s$	$\dot{m}_3 = \dot{m}_4 = \dot{m}_{CO_2}$	$\dot{m}_4 = \dot{m}_1 = \dot{m}_{CO_2}$ $\dot{m}_7 = \dot{m}_8 = \dot{m}_{H_2O} ev$
Energy Balance	$\dot{W}_{C=}$ $\dot{m}_{CO_2}(h_2 - h_1)$	$\dot{Q}_{gc} = \dot{m}_{CO_2}(h_3 - h_2)$ $\dot{Q}_{gs} = \dot{m}_{H_2O} c_{pH_2O} (T_6 - T_5)$	$h_3 = h_4$	$\dot{Q}_e = \dot{m}_{CO_2}(h_3 - h_2)$ $\dot{Q}_e = \dot{m}_{H_2O} c_{pH_2O} (T_7 - T_8)$
Entropy Balance	$\dot{S}_{gen,c} = \dot{m}_{CO_2}(s_2 - s_1)$	$\dot{S}_{gen,gc} = \dot{m}_{CO_2}(s_3 - s_2) + \dot{m}_{H_2O}(s_6 - s_5)$	$\dot{S}_{gen,v} = \dot{m}_{CO_2}(s_4 - s_3)$	$\dot{S}_{gen,ev} = \dot{m}_{H_2O}(s_7 - s_8) + \dot{m}_{CO_2}(s_1 - s_4)$
Exergy Balance	$\dot{E}x_{D,c} = \dot{m}_{CO_2}(ex_1 - ex_2) + \dot{W}_c$	$\dot{E}x_{D,gc} = \dot{m}_{CO_2}(ex_2 - ex_3) + \dot{m}_{H_2O}(ex_5 - ex_6)$	$\dot{E}x_{D,v} = \dot{m}_{CO_2}(ex_3 - ex_4)$	$\dot{E}x_{D,ev} = \dot{m}_{CO_2}(ex_4 - ex_1) + \dot{m}_{H_2O}(ex_7 - ex_8)$
Incoming Exergy	$ex_1 = (h_1 - h_0) - T_0(s_1 - s_0)$	$ex_2 = (h_2 - h_0) - T_0(s_2 - s_0)$ $ex_5 = (h_5 - h_0) - T_0(s_5 - s_0)$	$ex_3 = (h_3 - h_0) - T_0(s_3 - s_0)$	$ex_4 = (h_4 - h_0) - T_0(s_4 - s_0)$ $ex_7 = (h_7 - h_0) - T_0(s_7 - s_0)$
Outgoing Exergy	$ex_2 = (h_2 - h_0) - T_0(s_2 - s_0)$	$ex_3 = (h_3 - h_0) - T_0(s_3 - s_0)$ $ex_6 = (h_6 - h_0) - T_0(s_6 - s_0)$	$ex_4 = (h_4 - h_0) - T_0(s_4 - s_0)$	$ex_1 = (h_1 - h_0) - T_0(s_1 - s_0)$ $ex_8 = (h_8 - h_0) - T_0(s_8 - s_0)$
Exergy Efficiency	$\psi_c = \frac{\dot{m}_{CO_2}(ex_2 - ex_1)}{\dot{W}_c}$	$\psi_{gc} = \frac{\dot{m}_{H_2O}(ex_6 - ex_5)}{\dot{m}_{CO_2}(ex_2 - ex_3)}$	$\psi_v = \frac{ex_4}{ex_3}$	$\psi_{ev} = \frac{\dot{m}_{CO_2}(ex_1 - ex_4)}{\dot{m}_{H_2O}(ex_8 - ex_7)}$

4. Results and Discussion

For the first test part in Table 2 below, a capillary tube with a length of 2.40 m and a diameter of 2.00 mm was used. For the second part, the thermodynamic data obtained in the systems with a capillary tube with a length of 1.20 m and a diameter of 2.00 mm are presented. Actual powers are given in the table after deducting the compressor powers and the powers drawn by the circulation pumps (100W).



Figure 3. Pressure, mass CO2 flow and total power consumption in the test system (ISUBÜ CO2 Laboratory)

Table 2. Thermodynamic comparison in the first and second experiments

1. Experiment		2. Experiment	
Compressor power (kW)	0.719	Compressor power (kW)	0.707
Gas cooler pressure (bar)	100.0	Gas cooler pressure (bar)	100.0
Evaporator pressure (bar)	48.3	Evaporator pressure (bar)	50.8
COP _{HP}	3.72	COP _{HP}	4.01
EPC _{HP}	0.435	EPC _{HP}	0.484
EX _{total}	0.572	EX _{total}	0.537
Ψ _c	0.556	Ψ _c	0.577
Ψ _v	0.965	Ψ _v	0.967
Ψ _{gc}	0.509	Ψ _{gc}	0.613
Ψ _{ev}	0.398	Ψ _{ev}	0.353
Ψ _{II HP}	0.303	Ψ _{II HP}	0.326
m _{CO2} (Kg/sec)	0.01227	m _{CO2} (Kg/sec)	0.0135
\dot{m}_{gc} H ₂ O (Kg/sec)	0.0263	\dot{m}_{gc} H ₂ O (Kg/sec)	0.0263
\dot{m}_{ev} H ₂ O (Kg/sec)	0.0372	\dot{m}_{ev} H ₂ O (Kg/sec)	0.0372
T _{gcCO2} (K)	325.9	T _{gcCO2} (K)	325.5
T _{evCO2} (K)	286.1	T _{evCO2} (K)	288.1

In Table 2, a thermodynamic comparison of capillary tubes with the same diameter but different lengths has been made, and the change in some cases is presented at levels of thousandths. The shortening of the capillary tube brought an increase of 7.2% to the COP_{HP} value in the system, and the mass flow rate of the refrigerant increased by 9.1%.

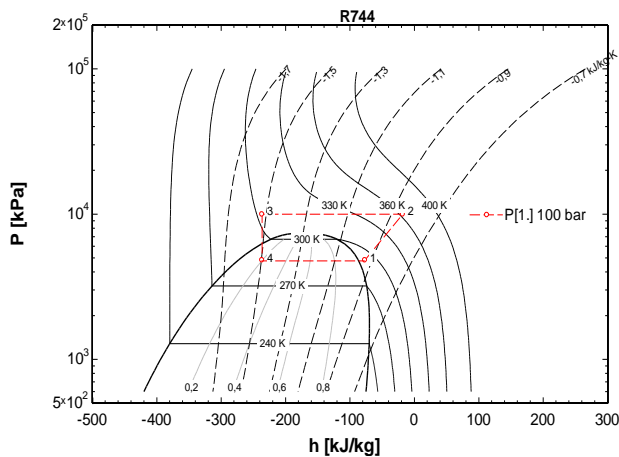


Figure 4. The change of the Ln P-h graph of the transcritical cycle with CO₂ is given (1. Capillary)

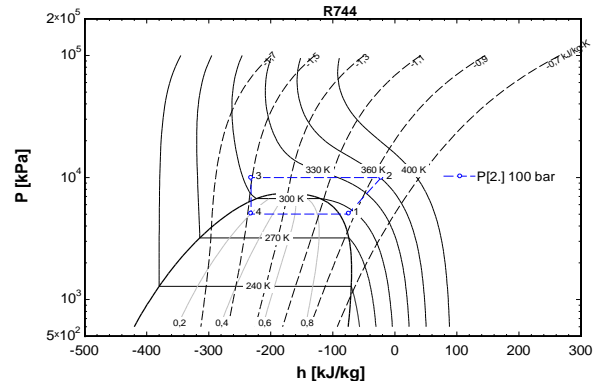


Figure 5. The variation of the Ln P-h graph of the transcritical cycle with CO₂ is given (2. Capillary)

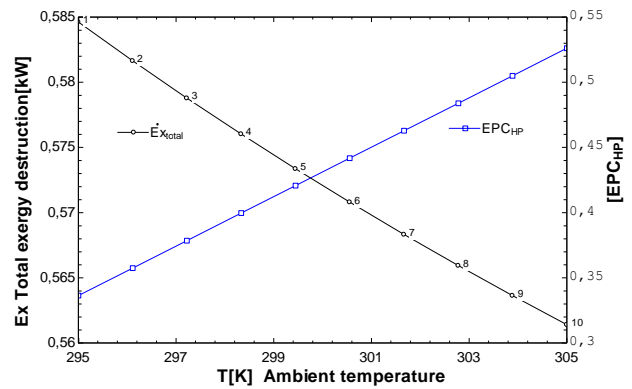


Figure 6. Change of 1. Capillary Ambient temperature in EPC_{HP} and Total exergy destruction

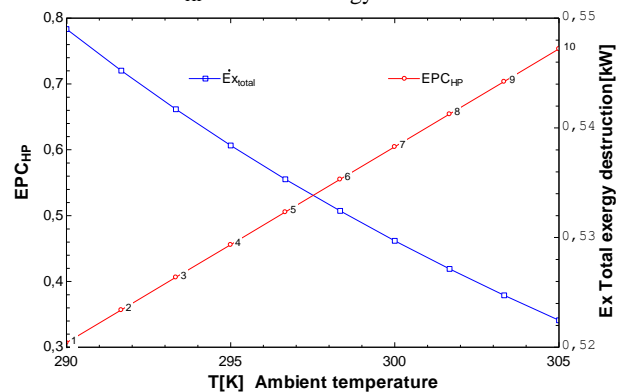


Figure 7. Change of 2. Capillary Ambient temperature in EPC_{HP} and Total exergy destruction

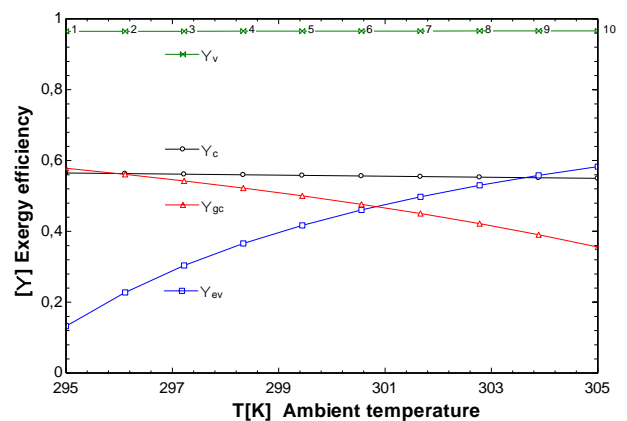


Figure 8. 1st Capillary The effect of change in ambient temperature on exergy efficiency

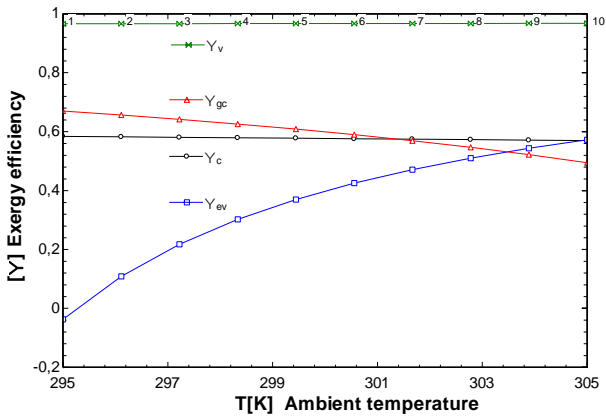


Figure 9. 2nd Capillary the effect of change in ambient temperature on exergy efficiency

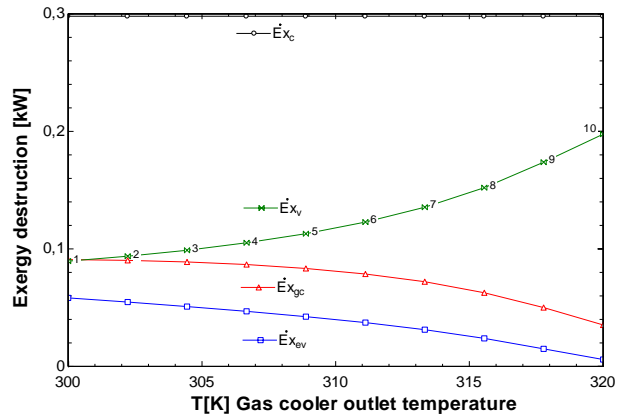


Figure 13. Change in exergy destruction with increase in 2nd capillary gas cooler outlet temperature

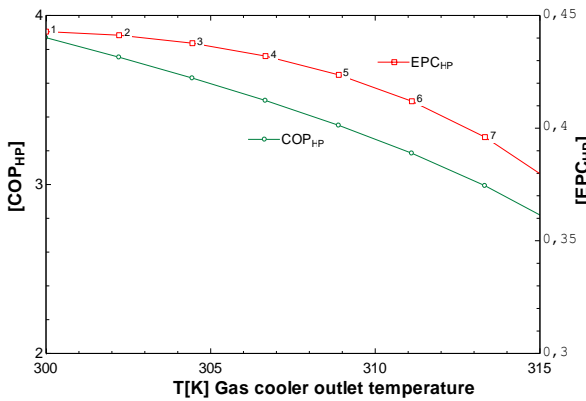


Figure 10. COP_{HP} and EPC_{HP} Heater change with the increase of 1st Capillary Gas cooler outlet temperature

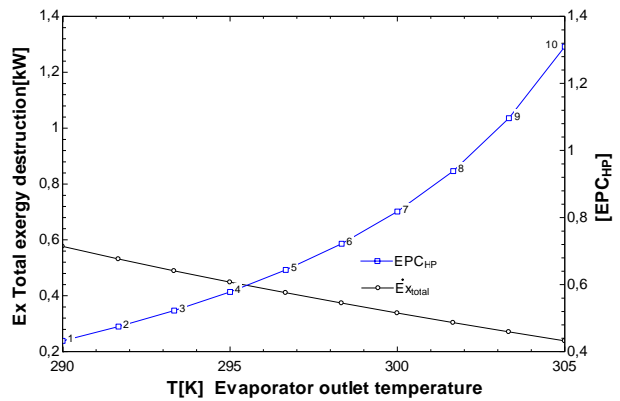


Figure 14. Change of 1st Capillary Evaporator outlet temperature in EPC_{HP} and destruction in Total exergy

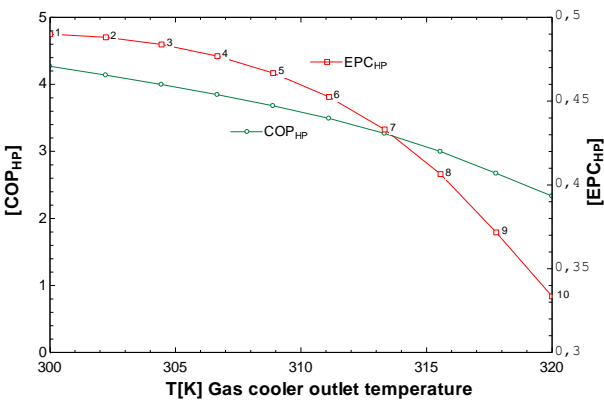


Figure 11. COP_{HP} and EPC_{HP} Heater change with the increase of 2nd Capillary Gas cooler outlet temperature

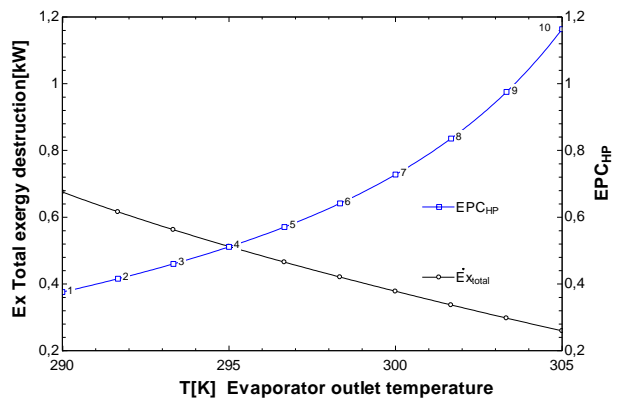


Figure 15. Change of 2nd Capillary Evaporator outlet temperature in EPC_{HP} and destruction in Total exergy

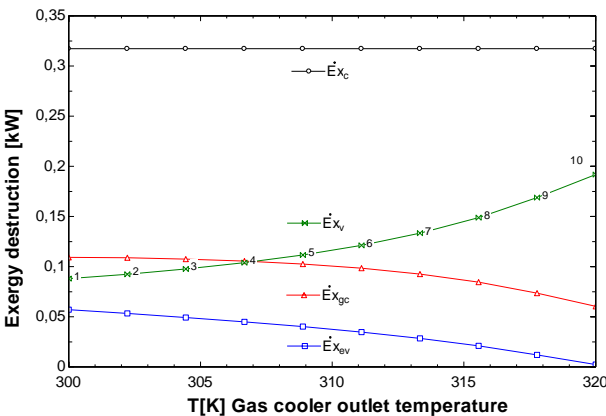


Figure 12. Change in exergy destruction with increase in 1st capillary gas cooler outlet temperature

While the increase in ambient temperature increases the EPC_{HP} value, there is a decrease in the total exergy destruction. In addition (Figure 6-7), while the increase in ambient temperature decreases the exergy efficiency of the gas cooler, it also increases the exergy efficiency of the evaporator (Figure 8-9). Increasing the gas cooler outlet temperature decreases the EPC_{HP} and COP_{HP} coefficients. As a result of the exergy destruction (Figure 10-11), the increase in the gas cooler outlet temperature, the highest compressor, valve, gas cooler and then the evaporator have been reached (Figure 12-13). The increase in the evaporator outlet temperature is seen as a factor that increases the

COP_{HP} and reduces the total exergy destruction (Figure 14-15).

5. Conclusion

In this study, a thermodynamic comparison of the water-to-water heat transfer of a single-stage heat pump system with transcritical CO_2 refrigerant and the capillary tubes of different lengths of a water-to-water cooling heat pump system operating at different operating pressures has been made. In the system, capillary pipes with a diameter of 2.00 mm and two different lengths are used. It is aimed to create the same gas cooler pressures with the two capillary pipes and to keep the cooling waters passing through the gas cooler and the evaporator at the same mass flow rate. The capillary tube in the first experiment is 2.40 m long, and 1.20 m in the second experiment. Thermodynamic analysis and comparison of the system were made. In the system with short capillary pipe (Experiment 2), it was observed that the COP_{HP} value was 7.2% higher, the mass flow rate of the refrigerant increased by 9.1% under the conditions of the short capillary pipe (according to the 1st Experiment), and on the other hand (Experiment 2) In the short capillary tube system, 1.8% less electrical power is used from the compressor power. In terms of exergetics, Exergetic coefficient of performance (EPC_{HP}) is 10%, compressor exergy efficiency (Ψ_c) is 3.6%, gas cooler exergy efficiency (Ψ_{gc}) is 16.9%, capillary tube exergy efficiency (Ψ_v) is 10%. There is a 7% increase in 0.2 and second law heating efficiency ($\Psi_{II,HP}$). In the latter case, the total exergy destruction increased by 6.5% and the evaporator exergy efficiency (Ψ_{ev}) increased by 12.7%.

General expressions that do not change for both systems;

- While the increase in ambient temperature increases the EPC_{HP} value, there is a decrease in the total exergy destruction. In addition, while the increase in ambient temperature decreases the exergy efficiency of the gas cooler, it also increases the exergy efficiency of the evaporator.

- Increasing the gas cooler outlet temperature decreases the EPC_{HP} and COP_{HP} coefficients. As a result of the exergy destruction, the increase in the gas cooler outlet temperature, the highest compressor, valve, gas cooler and then the evaporator have been reached.

- The increase in the evaporator outlet temperature is seen as a factor that increases the COP_{HP} and reduces the total exergy destruction.

There are many comments on this subject in the literature. For example, Agrawal et al., reported that it provides COP_{HP} with a shorter capillary tube length. The indicators in this study were consistent with the literature [8].

Transcritical CO_2 heat pump systems are systems that can easily release heat at high pressure. These systems are extremely important in determining the optimum

operating conditions, determining the capillary tube sizes and determining the evaporator temperature. Transcritical heat pumps require high pressure control to minimize power consumption. This control is a function of the optimal pressure, the pressure (or temperature) of the evaporating fluid, and the CO_2 gas cooler outlet temperature [10]. With the change in capillary tube length, the evaporator temperatures will be determined, as a result, determining the optimum working intervals will help the users to determine the working conditions.

Declaration

The authors declared no potential conflicts of interest with respect to the research, authorship, and/or publication of this article. The authors also declared that this article is original, was prepared in accordance with international publication and research ethics, and ethical committee permission or any special permission is not required.

Author Contributions

A. Elbir conducted an experiment, C. H. Bayrakçı provided consultancy, A. E. Özgür provided the installation of the system, Ö. Deniz developed the measuring system. A. Elbir proofread the manuscript.

Nomenclature

R744	: Carbon dioxide (CO_2)
COP	: Coefficient of Performance
EPC	: Exergetic Coefficient Of Performance
EEV	: electronic expansion valve
Ψ_{II}	: Second law exergy efficiency
T_0	: Ambient temperature (299,2K)
\dot{m}	: Mass flow rate (kg/s)
$\dot{E}x_{total}$: Total exergy destruction
s	: specific entropy
h	: Specific enthalpy
K	: temperature (Kelvin)
mm	: millimeters
HP	: heat pump
c	: compressor
ev	: evaporator
gen.	: generation
Sec	: second
P	: bar
Q	: heat (kW)
m	: meters
Ψ	: exergy efficiency
v	: valve
gc	: gas cooler
D	: destruction

References



1. Elbir, A., H. C. Bayrakçı, A. E. Özgür, and Ö. Deniz, *CO₂ Soğutucu Akışkanı İle Çalışan Transkritik Bir Isı Pompası*

- Sisteminin Farklı Basınçlarda Termodinamik Analizi*. Teknik Bilimler Dergisi, 2022. **12**(1): p. 24-32.
2. Jadhav, P. and H. Agrawal, *Comparative study on a straight and helical capillary tube for CO₂ transcritical system*. Journal of Physics: Conference Series **1451**: p. 012011, 2020.
 3. Jadhav, P. and H. Agrawal, *Flow Behavior Of Spiral Capillary Tube For CO₂ Transcritical Cycle*. Journal of Thermal Analysis and Calorimetry, 2020. **141**: p.2177–2188.
 4. Rocha, T. T. M., C. H. D. Paula, V. M. Cangussu, A. T. Maia, and R. N. D. Oliveira, *Effect of surface roughness on the mass flow rate predictions for adiabatic capillary tubes*. Energy Conversion and Management. International Journal of Refrigeration, October 2020. **118**: p. 269-278.
 5. Wang, Z., F. Wang, G. Li, M. Song, Z. Ma, H. Ren, and K. Li, *Experimental Investigation On Thermal Characteristics Of Transcritical CO₂ Heat Pump Unit Combined With Thermal Energy Storage For Residential Heating*. Elsevier Applied Thermal Engineering, 2020. **165**: p. 114505.
 6. Nebot-Andrés, L., J. Catalán-Gil, Sánchez, D. Calleja-Anta, D., R. Cabello, and R. Llopis, *Experimental determination of the optimum working conditions of a transcritical CO₂ refrigeration plant with integrated mechanical subcooling*. International Journal of Refrigeration, 2020. **113**: p.266-275.
 7. Song, Y., J. Wang, F. Cao, P. Shu, and X. Wang, *Experimental investigation on a capillary tube based transcritical CO₂ heat pump system*. Applied Thermal Engineering, 2017. **112**: p.184-189.
 8. Agrawal, N., and S. Bhattacharyya, *Adiabatic Capillary Tube flow Of Carbon Dioxide in A Transcritical Heat Pump Cycle*. International Journal of Energy Research, 2006. **31**: p.1016–1030.
 9. Wang, D., Lu, Y., and L. Tao, *Optimal combination of capillary tube geometry and refrigerant charge on a small CO₂ water-source heat pump water heater*. International Journal of Refrigeration, 2018. **88**: p.626-636.
 10. Agrawal, N., and S. Bhattacharyya, *Capillary Tube as an Expansion Device in a CO₂ (R744) Transcritical Heat Pump System*. In Handbook of Research on Advances and Applications in Refrigeration Systems and Technologies, 2015. p. 360-377.
 11. Song, Y., J. Wang, F. Cao, P. Shu, and X. Wang, *Experimental investigation on a capillary tube based transcritical CO₂ heat pump system*. Applied Thermal Engineering, 2017. **112**: p. 184-189.
 12. Agrawal, N., and S. Bhattacharyya, *Experimental investigations on adiabatic capillary tube in a transcritical CO₂ heat pump system for simultaneous water cooling and heating*. International journal of refrigeration, 2011. **34**(2): p. 476-483.
 13. Wang, D., Y. Lu, and L. Tao, *Optimal combination of capillary tube geometry and refrigerant charge on a small CO₂ water-source heat pump water heater*. International Journal of Refrigeration, 2018. **88**: p. 626-636.
 14. Date, A., O. Patil, S. A. Shet, and N. Agrawal, *Experimental studies on transcritical CO₂ heat pump system for simultaneous water cooling and heating application*. International Journal of Green Energy, 2022. **19**(2): p. 201-209.
 15. Jadhav, P., and N. Agrawal, *A comparative study of flow characteristics of adiabatic spiral and helical capillary tube in a CO₂ transcritical system*. International Journal of Ambient Energy, 2022. **43**(1): p. 4594-4601.
 16. Rocha, T. T. M., C. H. de Paula, J. J. G. Pabon, T. de Freitas Paulino, and R. N. de Oliveira, *Algebraic solution and experimental validation for adiabatic coiled capillary tubes operating in transcritical CO₂ cycle*. Applied Thermal Engineering, 2020. **181**: p. 115930.
 17. Anka, S. K., K. Mensah, S. Boahen, T. I., Ohm, Y. Cho, J. W. Choi, and J. M. Choi, *Performance optimization of an air source HVAC system for an internet data center building using the integrated COP method*. Journal of Building Engineering, 2022. **61**: p. 105308
 18. Jadhav, P., A. Sahu, and S. Ballal, *Numerical study on the straight, helical and spiral capillary tube for the CO₂ refrigerant*. Научно-технический вестник информационных технологий, механики и оптики, 2022. **22**(4): p. 804-811.
 19. Freegah, B., A. A. Hussain, and A. R. Al-Obaidi, *Comparison Study Between Theoretical Analysis And Artificial Neural Network Of The Capillary Tube*. Journal of Thermal Engineering, 2021. **7**(3): p. 690-699.
 20. El Achkar, G., B. Liu, Y. Liu, and R. Bennacer, *Enhancement of refrigeration system performance by refrigerant capillary injection in evaporator*. In Journal of Physics: Conference Series, 2021. **2116**(1): p. 012102.
 21. Danfoss. [cited: 17.01.2018]]; Available from: <http://refrigerants.danfoss.com/co2/#/>
 22. Elbir, A., *Theoretical and Experimental Investigation of a Transcritical CO₂ Heat Pump*, PhD Thesis, S.D.U. Graduate School of Natural And Applied Sciences, Isparta, 2020.
 23. Elbir, A., H. C. Bayrakçı, A. E. Özgür, and Ö. Deniz, *CO₂ Soğutmalı Transkritik Bir Isı Pompası Sisteminin Deneysel İncelenmesi*. Uluslararası Katılımlı 23. Isı Bilimi ve Tekniği Kongresi, ULIBTK 2021.
 24. Dwinanto, M. M., Suhanan, and Prajitno, *Exergy analysis of a dual-evaporator refrigeration systems*. In AIP Conference Proceedings, 2017. January, **1788**(1): p. 030011.
 25. Klein SA. *Engineering Equation Solver(EES) 2020*, F-Chart Software, Version 10.835-3D.



Research Article

A new approach to event- and model-based feature-driven software testing and comparison with similar approaches

Fevzi Belli ^{a,b} , Tugkan Tuglular ^{b,*}  and Ekinan Ufuktepe ^c 

^a University of Paderborn, Paderborn, Germany

^b Izmir Institute of Technology, Izmir, Türkiye

^c University of Missouri – Columbia, Columbia, MO, USA

ARTICLE INFO

Article history:

Received 26 June 2022

Revised 28 November 2022

Accepted 15 December 2022

Keywords:

Event sequence graphs
Feature-oriented software
development
Model-based testing

ABSTRACT

A software can be thought as a composition of features. Feature-oriented software development (FOSD) builds the development process on features. Part of the FOSD process is testing, and accordingly, it should be feature-driven. In model-based testing, test cases are systematically generated using the model. This research concentrates on event-based graphical models and utilizes event sequence graphs (ESGs). We develop a new test sequence generation algorithm for ESGs and named it short and frequent test sequences (SFT). Then we compare it with the existing test sequence generation algorithm called TSD. Moreover, we introduce two model-building approaches, namely daisy and swim lane, for ESGs and analyze their effects on feature-driven testing. For the evaluation, we use five different feature-driven software models. The evaluation results shows that both modeling approaches are advantageous in certain test objectives. For testing the software product as a whole, test sequence(s) should be generated by TSD from daisy modeled ESG. If a certain feature within the software product or its interaction with another feature is to be tested, then test sequence(s) should be generated by SFT from swim lane modeled ESG.

1. Introduction

A feature is a semantically cohesive entity of a software [1]. Feature-oriented software development (FOSD) aims for the configuration and composition of features to obtain a software [2]. FOSD enables software to be composed from features with respect to configuration. This approach enables reuse of features and managed variation of software, which is highly beneficial in case of software product families.

An important part of the FOSD process is testing. Although there are various approaches in testing, our scope in this research is model-based testing. In model-based testing, test cases are systematically generated using the model. The models are the behavioral specification of the software. This systematic approach enables tester to define test coverage criteria, which is important if only a feature is to be covered by the test case(s) instead of the whole software product.

Event sequence graphs (ESGs) are an event-based modeling approach for representing software under test (SUT) and generating tests case(s) or test sequence(s) [3]. Event sequence graphs can be obtained from finite state

machines (FSMs) by taking events and putting them into the vertices of a graph, where each walk on this graph, which is an ESG, can also be obtained by the corresponding walk on the FSM. The details can be found in [UYMS 2016]. ESGs are not the only approach that utilizes events as the core concept in modeling software. Event flow models [4] and event process chains [5] are two other examples.

Test case, or test sequence, generation can be seen as an optimization problem, where possible event sequences are tried to be covered with minimum number of test cases. For the building ESG models and for test sequence generation from them, a tool called TSD, which can be downloaded at <http://download.ivknet.de/>, was developed. The test sequence generation algorithm in TSD is optimized for end-to-end testing and feature-oriented testing was not a goal at its design time. However, there is a need for feature-oriented testing in model-based testing. We propose to use ESGs, where not only SUT but also features can be represented formally. As the first novelty of this research, we develop a new test sequence generation algorithm for ESGs and named it short and

* Corresponding author. Tel.: +90-232-7507875; Fax: +90-232-7507862.

E-mail addresses: belli@upb.de (Fevzi Belli), tugkantuglular@iyte.edu.tr (Tugkan Tuglular), eh46@missouri.edu (Ekinan Ufuktepe)

ORCID: 0000-0002-8421-3497 (Fevzi Belli), 0000-0001-6797-3913 (Tugkan Tuglular), 0000-0002-0156-4321 (Ekinan Ufuktepe)

DOI: [10.35860/iaorej.1135989](https://doi.org/10.35860/iaorej.1135989)

© 2022, The Author(s). This article is licensed under the CC BY-NC 4.0 International License (<https://creativecommons.org/licenses/by-nc/4.0/>).

frequent test sequences (SFT), which is suitable for feature-oriented testing. We compare it with the existing TSD test sequence generation algorithm.

While building ESG models to represent SUT, we observed that there could be two different model building approaches, namely daisy and swim lane, for ESGs. As the second novelty of this research, we present them and compare them to each other as well as investigate which one suits better with TSD and SFT. As a result of this research, we conclude that test sequence(s) should be generated by TSD from daisy modeled ESG if the test objective is product testing. If the test objective is feature or feature interaction testing, then test sequence(s) should be generated by SFT from swim lane modeled ESG.

The manuscript is structured as follows. After Introduction section, the methods section presents the fundamentals and explains the newly proposed SFT algorithm whereas the following section outlines and exemplifies the newly introduced daisy and swim lane model building approaches. In the results section, we present our findings and discuss them in the following section with comparison to related work. The final section concludes the paper.

2. Methods

2.1 Event Sequence Graphs

Event sequence graphs are a practical event-based behavioral modeling approach for representing software under test (SUT) and generating tests. They have a formal foundation, the formal definitions and the detailed explanations can be found in [3] and [6]. An ESG, which is a directed graph, starts with pseudo entry node vertex '[' and ends with pseudo exit vertex ']'. These pseudo vertices and their edges are not included in the vertex set and in the edge set, respectively [3]. For the ESG given in Figure 1, the vertex set V is $\{A, B, C\}$, and the edge set E is $\{(A, B), (A, C)\}$. For the ESG given in Figure 1, A could be a *Select* event, B be *Play Classical Music* event, and C be *Play Pop Music* event. So, the SUT behaves either *Select - Play Classical Music* or *Select - Play Pop Music*. Various examples can be found in [3], [6], [7], and [8].

A test sequence, or complete event sequence (CES), starts with the entry of the ESG and ends at its exit. One or more CES can be used for feature testing, but all CESs are required for product testing. We differentiate feature testing from product testing so that covering feature vertex set and edge set is sufficient for feature testing. We are not interested in interaction among the features for feature testing, whereas feature interaction is critical in product testing.

The following subsection outlines the existing test generation algorithm for ESGs, which we will compare with our newly developed test sequence generation algorithm for ESGs, which is explained in Section 3.

2.2 Existing Test Generation Algorithm for Event Sequence Graphs

One approach to generate CESs from ESG solves the Chinese Postman Problem (CPP) [7]. Solving CPP means finding the Euler cycles on the graph, i.e., starting from and returning to the same vertex by visiting each edge exactly once [8]. To achieve this, ESG is converted to a Euler graph by creating a pseudo edge from exit vertex to entry vertex [7]. Then this graph is balanced by assigning a positive degree vertex partition to a negative degree vertex partition and this assignment problem is solved by the Hungarian Matching Algorithm [9]. Further details can be found in [7] and [8]. The existing test sequence generation algorithm for ESGs is referred as TSD, since it is used by the TSD tool. In summary, this algorithm aims to cover all edges in ESG while trying to avoid using a previously passed edge. The algorithm achieves minimum number of tests.

2.3 New Test Generation Algorithm for Event Sequence Graphs

We present our new test generation algorithm for ESGs, which aims generating frequent but shorter test sequences from ESG. For generating short test sequences, the algorithm takes advantage of the well-known shortest path finding Dijkstra algorithm. Furthermore, our test generation algorithm trade upon the structure and nature of ESG. The ESG graphs can be defined as Hammock graphs [10],[11], which means that the graph has only one entry point/vertex and one exit point/vertex. The brief and general strategy of generating short and frequent test sequences is by randomly selecting one vertex (except the starting and ending vertex), then finding the shortest path from the starting vertex to the randomly selected vertex and finding the shortest path from the randomly selected vertex to the exit vertex. Finally, the two paths are connected from the randomly selected vertex, which represents the test sequence.

In Algorithm 1, we have given the formal algorithm to generate frequent and short test sequences from ESGs. The algorithm receives the ESG as an input to the algorithm and returns a test suite as an output. The generated test suite ensures that there is a 100% event-pair (edge) coverage. However, before generating the test cases for the test suite, the algorithm goes through a graph construction phase. The Dijkstra algorithm [12] finds the shortest path based on the vertices (events). Dijkstra algorithm has many applications in graph theoretic problems such as route planning [13] and path planning [14]. In graph theory, edges can be represented as vertices, which transforms the original graph into a new graph such as given in Figure 1. Once the graph is transformed graph, it will be beneficial in several ways; (1) enabling to perform the Dijkstra algorithm based on the event-pairs from the original graph, (2) allowing to select source and target event-pairs for finding shortest path, (3)

simplifying and guaranteeing the 100% event-pair coverage.

After the ESG is transformed, we provide the transformed ESG as an input to Algorithm 1 shown Figure 2. However, we recall that the entry node to the original ESG is vertex “[”, and the exit vertex is “]”. Therefore, in the transformed graph of ESG, it is likely to have multiple options of starting vertices and multiple options of exit vertices. The naive approach would be randomly selecting among the multiple starting vertices and multiple exit vertices. However, random selection has the risks of selecting a longer path, which violates the main objective of generating short test sequences. To eliminate the possibility of generating longer test sequences, while we have the chance to generate a shorter path, we reconstruct the graph by inserting one *pseudo starting vertex* (v_s), and one *pseudo exit vertex* (v_e). The v_s vertex has outgoing edges to the starting vertices from the transformed graph, and the v_e vertex has incoming edges from the exit vertices from the transformed graph, such as given in Figure 3. The graph reconstruction enables to have a Hammock graph, which will simplify test sequence generation process.

Once we have completed the graph reconstruction (inserting one pseudo starting and one exit vertex) we are able initiate the test generation process. Our test generation algorithm has an option to generate feature-oriented test sequences, or simply generate test sequences regardless of any feature information given in prior. If feature-oriented test sequences wanted to be generated, this information should be given. The required information is simply by providing which event-pairs (edges of the original ESG) are mapped to the desired feature of the variant. Then, this information is acquired by the “*getFeatureRelatedEdges()*” function in SFT algorithm for ESG. However, if no such information is provided, the function will return an empty set, and will not generate feature specific test sequences.

Now we assume that we have two edges namely, “[\rightarrow A” and “A \rightarrow B” that are related to a feature. Therefore, initially we must randomly select one edge among the feature related edges. Such as given in Figure 4, assume that the “A \rightarrow B” vertex is randomly selected. Then, we find the shortest path from v_s to “A \rightarrow B” (path P_0), and the shortest path from “A \rightarrow B” to v_e (path P_1).

- $P_0: v_s \rightarrow ([\rightarrow A) \rightarrow (A \rightarrow B)$
- $P_1: (A \rightarrow B) \rightarrow (B \rightarrow])$

After finding the paths P_0 and P_1 , we connect the two paths from the end of P_0 to the beginning of P_1 . Finally, the connected two paths represent a test sequence t , which is given below. We also notice that the generated test sequence also contains the edge “[\rightarrow A” among feature related edges. Since that “[\rightarrow A” edge is already covered in the generated test sequence we do not specifically generate another test sequence that targets the “[\rightarrow A” edge. However, other generated test sequences might cover “[\rightarrow A” or even “A \rightarrow

B”, but they will be covered by coincidence.

- $t: v_s \rightarrow ([\rightarrow A) \rightarrow (A \rightarrow B) \rightarrow (B \rightarrow])$

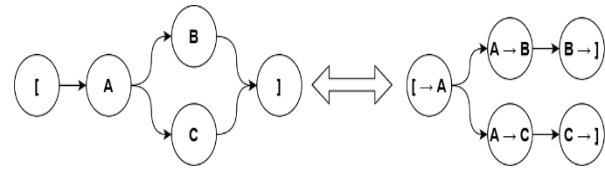


Figure 1. Graph transformation

Algorithm 1: SFT Algorithm for ESG

Input: Event Sequence Graph (ESG) G
Output: Test Suite T
 $V \leftarrow getVertices(G)$
 $E \leftarrow getEdges(G)$
// let v_0 be the entry vertex/event for G
 $v_0 \in V$, where $v_0 = “[$ ”
let v_s be a pseudo start vertex, where $v_s \in V$
let edge $e_s \leftarrow (v_s \rightarrow v_0)$, where $e_s \in E$
// let v_n be the exit/sink vertex for G
 $v_n \in V$, where $v_n = “]$ ”
let v_e be a pseudo end vertex, where $v_e \in V$
let edge $e_e \leftarrow (v_n \rightarrow v_e)$, where $e_e \in E$
 $E' \leftarrow getFeatureRelatedEdges(E)$
 $E'' \leftarrow E - E'$
while $E \neq \emptyset$ **do**
 let e_k be a randomly selected edge
 if $E' \neq \emptyset$ **then**
 // Select a random event from E'
 $e_k \leftarrow selectRandomEdge(E')$
 // remove edge from E'
 $E' \leftarrow E' - \{e_k\}$
 end
 else
 // Select a random event from E''
 $e_k \leftarrow selectRandomEdge(E'')$
 end
 // find shortest path from edge e_s to e_k
 $P_0 \leftarrow shortestPath(e_s, e_k)$
 // find shortest path from edge e_k to e_e
 $P_1 \leftarrow shortestPath(e_k, e_e)$
 // Connect paths P_0 , and P_1 to generate test sequence t
 $t \leftarrow connectPaths(P_0, P_1)$
 $T \leftarrow T \cup \{t\}$ *// Add test case t to test suite T*
 $F \leftarrow coveredEdges(t)$ *// find covered edges*
 $E \leftarrow E - F$ *// removes covered edges from set E*
end

Figure 2. SFT algorithm for ESG

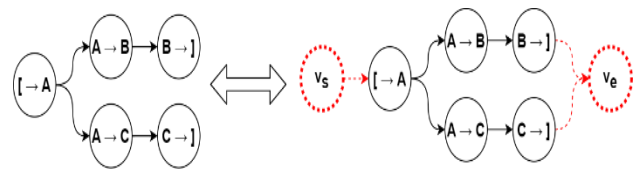


Figure 3. Inserting one *pseudo starting vertex* (v_s) and one *pseudo exit vertex* (v_e). On the left we have the transformed graph, and on the right we have reconstructed graph, which is now a Hammock Graph

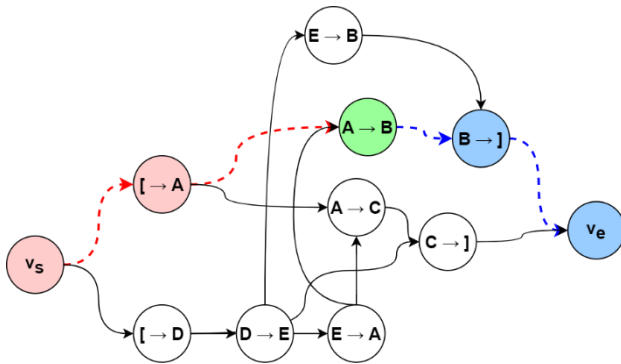


Figure 4. Running example for SFT Algorithm 1

In the next iteration, we check if there is any remaining edges that are not covered yet, and find that there are still 6 more edges that are not covered in the ESG, which are: ($[\rightarrow D)$, ($D \rightarrow E)$, ($E \rightarrow A)$, ($E \rightarrow B)$, ($A \rightarrow C)$, ($C \rightarrow]$). This means, in the next iteration the randomly selected edge will be among the remaining six edges.

This new test sequence generation algorithm for ESGs is referred as SFT, since it aims short and frequent test sequences. As opposed to TSD algorithm, its objective is not an optimized solution rather it covers all edges in ESG with short test sequences. Short test sequences have two advantages. First, they are fast and second, if there is a failure in the test sequence, other tests can still be executed.

In Algorithm 2 shown in Figure 5, we present the test minimization that is applied after Algorithm 1 composes the initial test suite. The test minimization has a straightforward approach to minimize the test suite. The SFT algorithm is likely to come up with test cases that can cover another. These types of scenarios occur if there are cycles or self-loop edges in the ESG. The number of generated tests and events are reduced by first finding the covered edges for each test cases. If the covered edges of a test are contained by another test, the contained test is removed from the test suite. Thereby, we cut down the number of tests and events to get rid of any redundancy.

2.4 Model Building Approaches for Event Sequence Graphs

We present that model building technique makes a difference in test sequence generation and in the use of the generated sequences. We utilize the bank account ESG as the running example. The terms model and ESG will be used interchangeably from this point on. Before explaining two different model building approaches, we introduce the definition of feature in ESGs.

A feature in ESG is a subgraph $F_G = (F_v, F_e)$, where F_v is the vertex set of the vertices exist in the feature and F_e is the edge set of the edges exist in the feature. Examples are given in the following two sub-sections, where daisy and swim lane model building approaches are outlined and exemplified.

Algorithm 2: Test suite minimization

```

Input: Test Suite  $T$ 
Output: Test Suite  $T'$ 
let  $T' \leftarrow \emptyset$ 
let  $C$  and  $C'$  be sets of covered edges
// Remove the test sequences that is
// covered by another test sequence
for each  $t_i$  in  $T$  do
  for each  $t_k$  in  $T$  do
    if  $t_i \neq t_k$  then
      // Gets the covered edges for test  $t_i$ 
       $C \leftarrow \text{coveredEdges}(t_i)$ 
      // Gets the covered edges for test  $t_k$ 
       $C' \leftarrow \text{coveredEdges}(t_k)$ 
      if  $C \subseteq C'$  then
        |  $T' \leftarrow T' \cup \{t_i\}$ 
      end
      else if  $C' \subset C$  then
        |  $T' \leftarrow T' \cup \{t_k\}$ 
      end
    end
  end
end
end

```

Figure 5. Test suite minimization algorithm

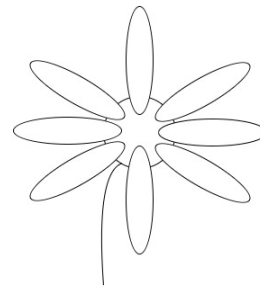


Figure 6. Daisy model

2.4.1 Daisy Model

In the daisy model, the features are attached as daisy leaves to the core of the model as given in Figure 6. The core is the main operation existing in all possible products. In the bank account ESG, it is a show menu event where all the operations of the features start and end. Therefore, each feature looks like a daisy leaf.

Figure 7 shows the bank account ESG as daisy model. An example feature as daisy leaf is *Credit* feature, of which edges are drawn in thick red. For the *Credit* feature,

F_v is {enter a credit amount, confirm credit approved, confirm credit disapproved} and

F_e is {(show menu, enter a credit amount), (enter a credit amount, confirm credit approved), (confirm credit approved, show menu), (enter a credit amount, confirm credit disapproved), (confirm credit disapproved, show menu)}.

Connection or variability point or vertex is show menu event. The features are connected through the show menu vertex.

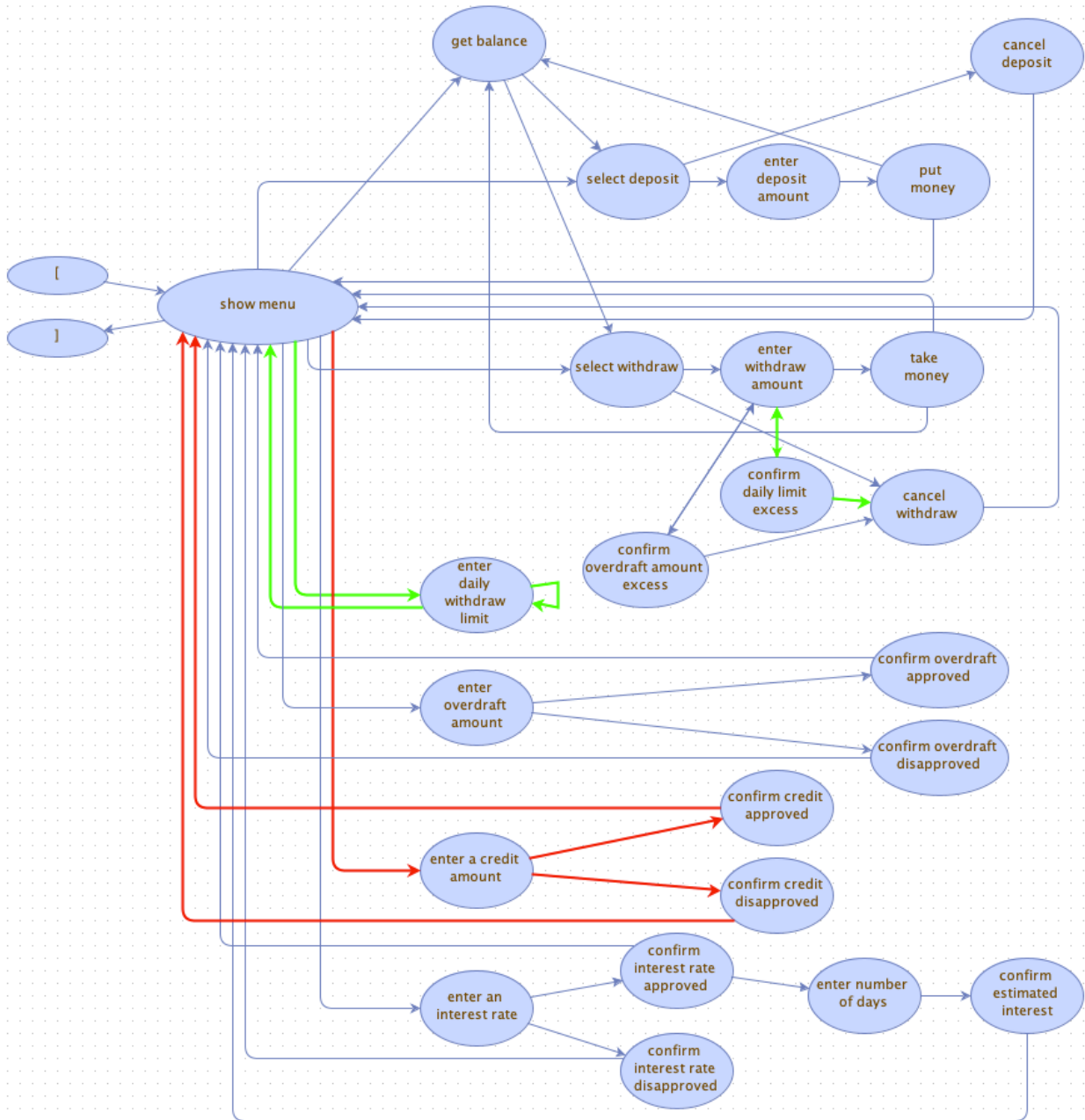


Figure 7. Bank account ESG as daisy model

A feature may interact with other features. As seen in bank account model, the DailyLimit feature, of which edges are drawn in thick green, interacts with Withdraw feature, but this does not affect the daisy leaf structure. For the features interacting with other features, special care should be taken in the process of ESG design in such a way that feature interaction is loosely coupled so that addition and removal of features do not affect the validity of ESG. For the DailyLimit feature,

F_v is {enter daily withdraw limit, confirm daily limit excess} and

F_e is {(show menu, enter daily withdraw limit), (enter daily withdraw limit, enter daily withdraw limit), (enter daily withdraw limit, show menu), (enter withdraw amount, confirm daily limit excess), (confirm daily limit excess, entry

withdraw amount), (confirm daily limit excess, cancel withdraw)}.

2.4.2 Swim Lane Model

In the swim lane model, the features are not attached as daisy leaves to the core of the model. Instead, they go from start, i.e., entry vertex of ESG, to finish, i.e., exit vertex of ESG, as given in Figure 8. Figure 9 shows swim lane model of the running example. The Credit feature, of which edges are drawn in thick red, flows from its own lane without any interaction with other features. For the Credit feature,

F_v is {enter a credit amount, confirm credit approved, confirm credit disapproved} and

F_e is {([, enter a credit amount), (enter a credit amount, confirm credit approved), (confirm credit approved,)}, (enter

a credit amount, confirm credit disapproved), (confirm credit disapproved,)}).

As seen in the swim lane ESG, the connection vertex is the pseudo start event as opposed to the show menu vertex in the daisy ESG.

The *DailyLimit* feature, of which edges are drawn in thick green, interacts with *Withdraw* feature, but this does not affect the swim lane structure. The necessary caution in ESG design explained in Section 4.1 to achieve loosely coupled features should also be taken in the swim lane model building approach.

In the swim lane ESG,

F_v is {enter daily withdraw limit, confirm daily limit excess} and

F_e is {(, enter daily withdraw limit), (enter daily withdraw limit, enter daily withdraw limit), (enter daily withdraw limit,)}, (enter withdraw amount, confirm daily limit excess), (confirm daily limit excess, entry withdraw amount), (confirm daily limit excess, cancel withdraw)} for the *DailyLimit* feature.

3. Results

In this section, we show that model building approach makes a difference in test sequence generation and the use of the generated sequences. We continue to utilize the bank account ESG as the running example.

Table 1 outlines the number of test sequences generated by both algorithms for two bank account (BA) ESGs, namely daisy BA ESG and swim lane BA ESG, as well as the total number of events in these test sequences, which is considered as the length of the test suite. Table 1 shows that TSD covers daisy BA ESG with one test sequence achieving its objective of a minimum number of test sequences. On the other hand, SFT covers daisy BA ESG with 18 test sequences with an average of 5.28 events per test, achieving its objective of short test sequences.

The reason is that due to the structure of the daisy model, specific events are covered more than once in every test sequence. These specific events inevitably cover or reach other events in the ESG. Therefore, this causes to generate test sequences with events that are already covered more than once. On the other hand, due to the structure of the swim lane model, there are alternative paths that could be reached by other events that are not covered yet. Thereby, it is more likely to generate a test suite with fewer events with fewer duplicate events.

We repeat the experiments with other four models, namely email, elevator, online shopping, and smart home. Like bank account, they model feature-based software. All the model drawings used in evaluation are available at <https://github.com/esg4aspl/comparison-of-event-based-modeling-approaches/tree/master/models>. Table 2 outlines their number of features, events, and edges. The models are from various domains with different number features. They

are sorted with respect to their number of events. Although the difference between daisy model and swim lane model is zero or just one event, the modeling approach critically affects certain choices in testing, which are discussed after delineating all the facts about the experiments.

Table 3 presents test sequence generation times for all models with respect to the modeling approach. It is observed that based on average SFT works faster than TSD. In Figure 10, we show the boxplot of execution times for SFT, which includes the outliers as well. Even with the outliers, SFT either faster or almost the same as TSD’s average execution time.

Table 1 shows that TSD covers swim lane BA ESG with 15 test sequences and 49 events. Here, we see the effect of the modeling approach. In the daisy model, the features are like daisy leaves attached to the core feature, which enables loops in the ESG. Because of these loops, TSD can cover daisy BA ESG in one test sequence. However, since there are no loops in the swim lane modeling approach and features run (swim) to completion, we observe that TSD results in a minimum of 15 test sequences with an average of 3.27 events. On the other hand, SFT covers swim lane BA ESG with 18 test sequences with an average of 3.06 events. The loop property of the daisy modeling approach affects SFT in the total number of events.

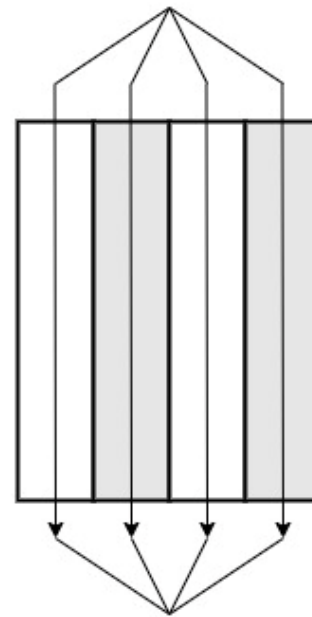


Figure 8. Swim lane model

Table 1. Bank account ESGs

Modeling Approach	TSD		SFT	
	No of test seq	No of events	No of test seq	No of events
daisy BA ESG	1	64	18	95
swim lane BA ESG	15	49	18	55

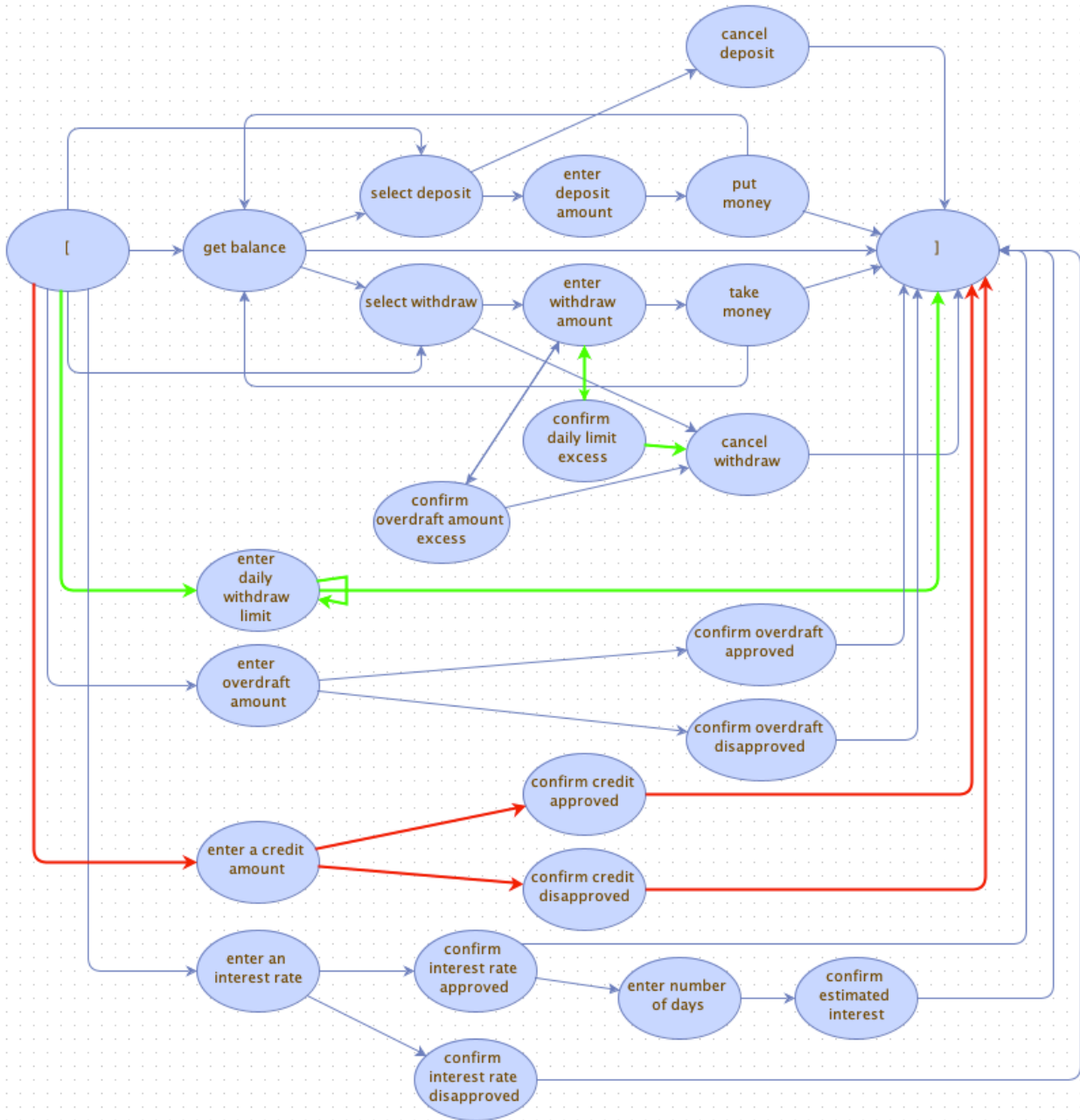


Figure 9. Bank account ESG as swim lane model

Table 2. Models under experiment

Models with No of Features	Modeling Approach	No of events	No of edges
Elevator EL (3 features)	daisy	16	26
	swim lane	15	24
Email EM (5 features)	daisy	19	38
	swim lane	18	36
Online Shopping OS (4 features)	daisy	23	37
	swim lane	23	37
Bank Account BA (9 features)	daisy	26	46
	swim lane	25	45
Smart Home SH (16 features)	daisy	41	70
	swim lane	41	70

Table 3. Test sequence generation times

Model	Modeling Approach	TSD (s)	SFT (s)
Elevator	daisy	0.095	0.082
	swim lane	0.097	0.082
Email	daisy	0.100	0.092
	swim lane	0.108	0.088
Online Shopping	daisy	0.098	0.089
	swim lane	0.099	0.890
Bank Account	daisy	0.103	0.098
	swim lane	0.106	0.095
Smart Home	daisy	0.113	0.112
	swim lane	0.120	0.106

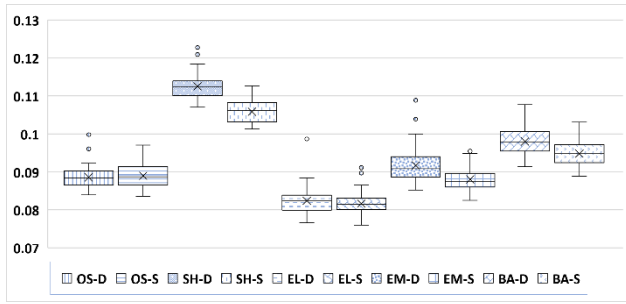


Figure 10. Boxplot of execution times for each case study

Table 4. Number of test sequences and total number of events in test sequences

Models	TSD		SFT	
	No of test seq	No of events	No of test seq	No of events
EL-D	1	43	8	78
EL-S	4	38	8	60
EM-D	1	47	16	90
EM-S	9	37	16	57
OS-D	1	53	10	81
OS-S	5	53	10	75
BA-D	1	64	17	92
BA-S	15	49	19	56
SH-D	1	83	30	170
SH-S	26	170	30	189

Table 4 presents the number of tests produced by TSD for all ten ESGs, five software modeled with two different approaches. The models are ordered on the X axis by the number of events shown in Table 2. Table 4 also presents the number of tests produced by SFT for all ten ESGs. In Table 4, we observe that the number of events for the swim lane model for SFT is less than the number of events from the daisy model. The reason is because of the algorithm of SFT and the structure of the daisy model. SFT aims to generate short test sequences, and when used on a daisy model, it generates test sequences with events and event pairs already covered.

The number of test sequences and events given in Table 4 for the SFT algorithm is rounded up to integer average values. Unlike the TSD algorithm, SFT has randomness, which may generate a different number of tests with other events. Therefore, in Figure 11 and Figure 12, respectively, we present the boxplots of the number of generated test sequences and the number of events for SFT.

4. Discussion

These experiments indicate that if the objective of testing is to test the software product as a whole, then test sequence(s) should be generated by TSD from daisy modeled ESG. If a certain feature within the software product is to be tested, then test sequence(s) should be generated by SFT from swim lane modeled ESG.

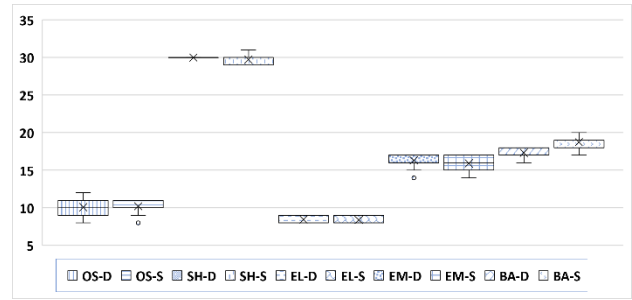


Figure 11. Boxplots of the number of generated test cases for each case study

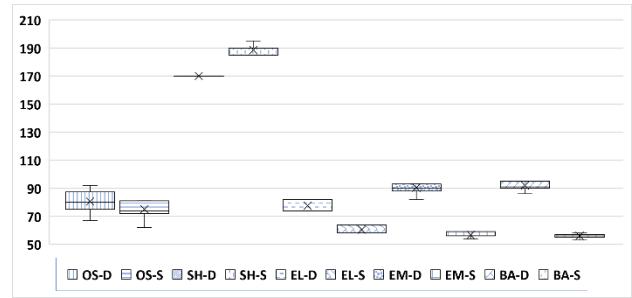


Figure 12. Boxplots of the number of events from the generated test cases for each case study

Moreover, if certain feature interactions are the goal of testing, then again test sequence(s) generated by SFT from swim lane modeled ESG should be preferred. Since both model building approaches are advantageous in certain test objectives, it would be favorable to prepare and keep ready both daisy and swim lane ESG models. This would be a tedious effort. Therefore, there should be a transformation between two models, which we plan as a future work.

4.1 Threats to Validity

We discuss the limitations of our evaluations that involves the internal and external threats to validity.

Internal Threats to Validity: The novel test generation approach SFT is based on finding the shortest paths between the start node to the selected node, and the selected node to the exit node. However, the node between the start and the exit node is selected randomly, which can lead to generating a different number of tests, and events on each run. Therefore, to evaluate if our test generation approach generates a significantly different number of tests and events, in Figure 11 and Figure 12, we show the distribution of the number generated tests and events of 50 different executions. For 10 case studies, we have observed that there are no outliers in terms of the number of events.

For the generated tests, among ten case studies, eight of them did not have any outliers. However, the remaining two case studies (OS-S and EM-D) had outliers only that generated a few numbers of test cases. We have carefully investigated the two ESG models and noticed that the two

models had cycles, including self-loops. In other words, there were edges defined in the ESG that caused feedback. During random selection, if the feedback edges are not initially selected and left for last, the SFT algorithm is likely to generate more test cases. If the feedback edges were selected earlier, it would produce fewer tests since the test sequence included the self-loop will already cover the test sequence without the self-loop. The outliers that generated fewer test cases are scenarios in which the self-loop edges were selected first compared to the other edges. Therefore, to minimize the test cases, the random selection process can assign a higher priority to self-loop edges in an ESG.

External Threats to Validity: Even though we have studied 10 case studies, there could still be different scenarios that may have not been included in this study. For instance, our study is limited to two graph models which we have defined as a daisy and swim lane. However, there could be different graph structures or types that could result in different.

4.2 Comparison with Related Work

We summarize the research on model-based testing in FOSD. Olimpiew and Gomma [15] proposed an approach for mapping the UML models, namely use case and sequence diagrams, so that functional tests are systematically produced. In Lamancha et al.'s work [16], feature scenarios are described UML sequence diagrams. Through model transformations, the sequence diagrams are converted into test cases. These approaches utilize UML models that are not formal and, therefore, error-prone compared to our proposed method.

Petry et al. [17] conducted a systematic mapping study and built a roadmap from 44 selected studies. Some of their results concerning our research are as follows: "Finite State Machines is the most used model to test SPLs" and "Behavioral-based and Scenario-based are the most used models" [17].

Lity et al. [18] utilized finite state machine models for delta-oriented testing of SPLs. Uzuncaova et al. [19] and Neto et al. [20] proposed repeated extensions through FSM deltas for delta-oriented test generation. Lochau et al. [21] proposed an integrated delta-oriented architectural test modeling and testing approach for component as well as integration testing. Their approach is component-based and aimed for integration testing. Dukaczewski et al. [22] proposed requirements-based delta-oriented SPL testing, which takes requirements into focus and uses them to define deltas.

Varshosaz et al. [23] proposed to utilize deltas for an incremental structure to formulate FSM-based test models. Devroey et al. [24] utilized featured transition systems for test generation for SPL products. Although these approaches are formal, they do not utilize a formal definition of features, and software composition is incremental with deltas. In contrast, we utilize a formal definition of features, and our composition does not require any deltas.

Belli et al. [25] mapped feature models to ESGs. This approach enabled holistic testing for the SPL and its variants. Tuglular et al. [26] introduced featured event sequence graphs, where there are distinct ESGs for each feature. They proposed a test generation technique for each product from any other smaller product, which is different than delta-oriented testing. Both research [25] and [26] used original TSD algorithm for test sequence generation and therefore are different than this research. None of the above research have introduced any model building approach.

5. Conclusion

Testing in feature-oriented software development requires validation of features alone, validation of feature interactions, and validation of the whole product. This research addresses this problem from model-based testing perspective and presents two novelties, a new test sequence generation algorithm developed considering feature and feature interaction testing and two model building approaches. An evaluation on five feature-oriented software models is performed and the results show that SFT with swim lane model building fits well to feature testing whereas TSD with daisy model building suits product testing. As seen with the examples the model building approach makes a difference in test generation. Moreover, depending on the test objective different combinations of model building approach and test generation algorithm should be used for efficient test generation in model-based testing. In the future, we are going to work on the formal definitions of the *daisy* and *swim lane* modeling techniques and algorithms for *daisy* to *swim lane* and vice versa model transformations.

Declaration

The authors declared no potential conflicts of interest with respect to the research, authorship, and/or publication of this article. The authors also declared that this article is original, was prepared in accordance with international publication and research ethics, and ethical committee permission or any special permission is not required.

Author Contributions

Tugkan Tuglular and Ekinan Ufuktepe developed the methodology and performed the evaluation. Fevzi Belli supervised and improved the study. All authors wrote and proofread the manuscript together. The authors are given in alphabetical order.

References

1. Apel, S., Batory, D., Kästner, C., Saake, G., *Feature-oriented software product lines*. 2016, USA: Springer-Verlag Berlin Heidelberg.
2. Apel, S., Kästner, C., *An overview of feature-oriented software development*. J. Object Technol, 2009. **8**(5): p. 49-84.

3. Belli, F., *Finite state testing and analysis of graphical user interfaces*. Proceedings of the 12th IEEE International Symposium on Software Reliability Engineering, 2001. Washington, DC, USA: p. 34-43.
4. Memon, A.M., *An event-flow model of GUI-based applications for testing*. Software testing, verification and reliability, 2007. **17**(3): p. 137-157
5. Amjad, A., Azam, F., Anwar, M.W., Butt, W.H., Rashid, M., *Event-driven process chain for modeling and verification of business requirements—a systematic literature review*. IEEE Access, 2018. **6**: p. 9027-9048.
6. Belli, F., Budnik, C.J., White, L., *Event based modelling, analysis and testing of user interactions: approach and case study*. Software Testing, Verification and Reliability, 2006. **16**(1): p. 3-32.
7. Belli, F., Budnik, C.J., *Minimal Spanning Set for Coverage Testing of Interactive Systems*. Proceedings of the International Colloquium on Theoretical Aspects of Computing, 2005. Springer Berlin Heidelberg: p. 220-234.
8. Belli, F., Guler, N., Linschulte, M., *Does" depth" really matter? on the role of model refinement for testing and reliability*. Proceedings of the IEEE 35th Annual Computer Software and Applications Conference (COMPSAC), 2011: p. 630-639.
9. Burkard, R., Dell'Amico, M., Martello, S., *Assignment problems: revised reprint*. 2012, SIAM.
10. Kas'yanov, V.N., *Distinguishing hammocks in a directed graph*. Proceedings of the Doklady Akademii Nauk, 1975.
11. Ferrante, J., Ottenstein, K.J., Warren, J.D., *The program dependence graph and its use in optimization*. ACM Transactions on Programming Languages and Systems, 1987. **9**(3): p. 319-349.
12. Dijkstra, E.W., *A note on two problems in connexion with graphs*. Numerische Mathematik, 1959. **1**: p. 269-271.
13. Kim, S., Jin, H., Seo, M., Har, D., *Optimal path planning of automated guided vehicle using dijkstra algorithm under dynamic conditions*. Proceedings of the 7th IEEE International Conference on Robot Intelligence Technology and Applications, 2019. p. 231-236.
14. Luo, M., Hou, X., & Yang, J., *Surface optimal path planning using an extended Dijkstra algorithm*. IEEE Access, 2020. **8**: p. 147827-147838.
15. Olimpiew, E.M., Gooma, H., *Model-based testing for applications derived from software product lines*. ACM SIGSOFT Software Engineering Notes, 2005. **30**(4): p. 1-7.
16. Lamanca, B.P., Diaz, O., Azanza, M., Polo, M., *Software product line testing: A feature oriented approach*. Proceedings of the IEEE International Conference on Industrial Technology, 2012. p. 298-305.
17. Petry, K. L., Oliveira Jr, E., Zorzo, A. F., *Model-based testing of software product lines: Mapping study and research roadmap*. Journal of Systems and Software, 2020. **167**: p. 110608.
18. Lity, S., Lochau, M., Schaefer, I., Goltz, U., *Delta-oriented model-based SPL regression testing*. Proceedings of the Third International Workshop on Product Line Approaches in Software Engineering, 2012.
19. Uzuncaova, E., Khurshid, S., Batory, D., *Incremental test generation for software product lines*. IEEE transactions on software engineering, 2010. **36**(3): p. 309-322.
20. Neto, P.A. da M.S., Machado, I. do C., Cavalcanti, Y.C., Almeida, E.S. de, Garcia, V.C., Meira, S.R. de L., *A Regression Testing Approach for Software Product Lines Architectures*. Proceedings of the Fourth Brazilian Symposium on Software Components, Architectures and Reuse, 2010. p. 41–50.
21. Lochau, M., Schaefer, I., Kamischke, J., Lity, S., *Incremental Model-Based Testing of Delta-Oriented Software Product Lines*. in Tests and Proofs, 2012. p. 67–82.
22. Dukaczewski, M., Schaefer, I., Lachmann, R., Lochau, M., *Requirements-based delta-oriented SPL testing*. Proceedings of the 4th International Workshop on Product Line Approaches in Software Engineering, 2013. p. 49-52.
23. Varshosaz, M., Beohar, H., Mousavi, M.R., *Delta-oriented FSM-based testing*. Proceedings of the International Conference on Formal Engineering Methods, 2015: p. 366-381.
24. Devroey, X., Perrouin, G., Schobbens, P.-Y., *Abstract test case generation for behavioural testing of software product lines*. Proceedings of the 18th ACM International Software Product Line Conference, Companion Volume for Workshops, Demonstrations and Tools, 2014: p. 86-93.
25. Belli, F., Tuğlular, T., Ufuktepe, E., *Heterogeneous Modeling and Testing of Software Product Lines*. Proceedings of the 21st IEEE International Conference on Software Quality, Reliability and Security Companion, 2021: p. 1079-1088.
26. Tuğlular, T., Beyazıt, M., Öztürk, D., *Featured Event Sequence Graphs for Model-Based Incremental Testing of Software Product Lines*. Proceedings of the 43rd IEEE International Conference on Computer, Software and Applications, 2019. Milwaukee, Wisconsin, USA: p. 197-202.



Research Article

Reliability estimation for drone communication by using an MLP-based model

A. F. M. Shahen Shah ^{a,*}  and Muhammet Ali Karabulut ^b 

^aElectronics and Communication Engineering, Yildiz Technical University, Istanbul, Turkey

^bElectrical and Electronics Engineering, Kafkas University, Kars, Turkey

ARTICLE INFO

Article history:

Received 14 August 2022

Revised 23 November 2022

Accepted 15 December 2022

Keywords:

ANN

Drone communication

FANETs

MLP

Reliability

ABSTRACT

Unmanned aerial vehicles (UAVs) or drones have been widely employed in both military and civilian tasks due to their reliability and low cost. UAVs ad hoc networks also acknowledged as flying ad-hoc networks (FANETs), are multi-UAV systems arranged in an ad hoc manner. In order to maintain consistent and effective communication, reliability is a prime concern in FANETs. This paper presents an analytical framework to estimate the reliability of drones' communication in FANETs. The proposed system takes into account the reliability of communications in FANETs, including channel fading. The suggested analytical investigation is used to generate a dataset, then an artificial neural network (ANN) based multi-layer perceptron (MLP) model is used to estimate the reliability of drones' communication. Moreover, to define the best MLP model with hidden layers, the correlation coefficient (R^2), mean square error (MSE), root mean square error (RMSE), and mean absolute percentage error (MAPE) are obtained. Moreover, numerical results are presented which verify analytical studies.

1. Introduction

Recent technical advancements in fields like robotics, telecommunications, and computer networks have led to the emergence of unmanned aerial vehicles (UAVs) as an alternate method of offering a variety of applications in both military and civilian domains. UAVs or drones will have a significant breakthrough in the upcoming 6G [1]. Flying ad hoc networks (FANETs) enable drone-to-drone (D2D) and drone-to-infrastructure (D2I) communication. FANETs have received numerous attention in recent years for a variety of services. UAVs must be able to interact effectively with one another and with existing networking infrastructures in order to fully benefit from their provided services. Therefore, the important concern in FANET is increasing the reliability of message dissemination [2-7]. In order to fulfill the criteria and achieve life-saving objectives, a drone must be able to transmit packets reliably in FANETs.

Deep learning (DL) has drawn a lot of interest and is frequently utilized in various disciplines to enhance the effectiveness of earlier techniques [8]. DL-based approaches can avoid the time-consuming task of identifying features and gathering private information since it automatically extracts and picks features from raw

data. In terms of resource requirements, while training a DL-Based method requires a significant amount of computational power, the majority of trained DL classifiers are small and computationally efficient. In short, DL-based approaches are appropriate for usage since they can achieve improved performance with simply raw traffic inputs and low resource needs [9].

The authors' method improves the localization mission by utilizing a decision-making approach based on a temperature-based probabilistic model developed to anticipate the distance to the forest fire in [10]. A control system for moving UAVs within a designated coverage region is provided in [11]. The motion control system, which is reliant on the distance between the drones and their signal strength, enables the drones to successfully connect and subsequently transmit data at fast speeds [12-14]. A dependable and effective cooperative MAC protocol was put up by [15] to increase communication dependability. For extremely reliable multi-hop message distribution under a variety of channel situations, [16] presented a cooperative communication strategy. In [17], a method for generating stable cluster structures was proposed for emergency message dissemination. A route finding method based on ant colony optimization is

* Corresponding author. Tel.: +90 212 383 5881.

E-mail addresses: shah@yildiz.edu.tr (A. F. M. S. Shah), mali.karabulut@kafkas.edu.tr (M. A. Karabulut)

ORCID: 0000-0002-3133-6557 (A. F. M. S. Shah), 0000-0002-2080-5485 (M. A. Karabulut)

DOI: [10.35860/iarej.1162019](https://doi.org/10.35860/iarej.1162019)

© 2022, The Author(s). This article is licensed under the CC BY-NC 4.0 International License (<https://creativecommons.org/licenses/by-nc/4.0/>).

described in [18]. A reliability parameter was also created in order to choose trustworthy links and eliminate bad connections from a route. To improve reliability, [19] proposed a routing system based on QoS and particle swarm optimization (PSO). A dependable UAV routing system was introduced in [20]. This protocol allowed dependable vehicles to communicate by halting the flow of pointless packets. [21] outlines a technique for using ANN models to find misbehavior. This technique combined feedforward and backpropagation algorithms to classify misbehavior. The neural networks (NN) and the simulated annealing clustering approach were used to choose the cluster's head in the clustering-based reliable routing system [22]. The optimum routes were assigned and traffic was managed in VANETs using the convolutional neural network (CNN) model [23]. [24] describes a resource allocation system based on deep reinforcement learning. [25] determined the optimal contention window (CW) size using PSO, differential evolution, and the artificial bee colony approach. The major goal of [26] is to outline the wireless and security challenges that arise in relation to UAV-based delivery systems, real-time multimedia streaming, and intelligent transportation systems. Such problems are addressed using ANN-based solution strategies.

With the use of machine learning, analytical models may be automated nearly fully without the need for human participation. In order to automate the evaluation of the dependability of drone communications, this article uses ANN, one of the most efficient machine learning techniques. Biological neural networks, such as those in the human brain, are imitated by ANNs, which are mathematical tools. The networks execute non-linear input-to-output mapping in the absence of comprehensive information. The neuron, sometimes referred to as a node, is the smallest information processing unit and the basis of network activity. Usually, one neuron is not enough to solve an issue. As a result, a layer is often composed of a collection of neurons. To create neural networks with various topologies, ANN neurons can be connected in a number of different ways. A neural network often functions as a "black box" that may be taught to predict the values of certain output variables given adequate input data. The most influential ANN designs are feedforward multi-layer neural networks. The fundamental neurons that make up the input layer, the hidden layer(s), and the output layer are often included in these networks. The input signal travels forward via the network layers at a time. Multi-layer perceptron (MLP) is the name of the network that was employed in this study [27–29].

Being able to benefit from offered services requires reliable packet delivery, which is one of the communication challenges in FANETs. In this paper, the reliability of drones' communication is estimated using an artificial neural network (ANN) based multi-layer

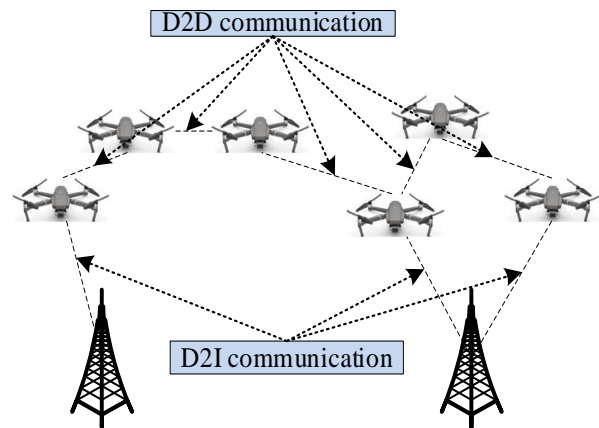


Figure 1. Structure of a basic FANETs

perceptron (MLP) model. The following are the article's primary contributions:

- A Markov model based analytical study is presented for FANET considering Nakagami-m fading.
- An algorithm is provided to calculate the reliability of drones' communication.
- Using the proposed analytical analysis, a dataset is generated and an ANN based MLP model is designed for the reliability estimation of drone communications.
- In order to support theoretical studies, numerical results are provided. Correlation coefficient (R^2), mean square error (MSE), root mean square error (RMSE), and mean absolute percentage error (MAPE) are obtained for different models and the best MLP model is defined.

2. Reliability Estimation of Drone Communication

A basic structure of FANETs is shown in Figure 1. We consider a network of N drones in which drones are deployed at random. Let $b(t)$ represent the drone's stochastic backoff time counter for the given time t . The backoff value in this Markov chain [2] is obtained uniformly from $[0, CW_0 - 1]$ at the beginning. The backoff is lowered by 1 if it is detected to be idle. When the channel detects idleness once again, it is resumed after pausing if the channel gets busy. The packet will then be transmitted if the backoff value falls to zero. If any of the remaining drones transmit at the same time slot then the collision will occur. A packet will be retransmitted until the retransmission limit. Even if there is no collision, packet transmission can be unsuccessful due to channel fading. If the transmitting drone is reliable, the channel is idle, the transmission does not fail due to channel fading, there is no contention, and there is no collision from the hidden drones, then the transmission will be successful.

If the packet is reliably sent by the transmitting drones and the communication hardware of the receiving drone is reliable, then communications between drones are reliable. The packet sent by the originating drone may be

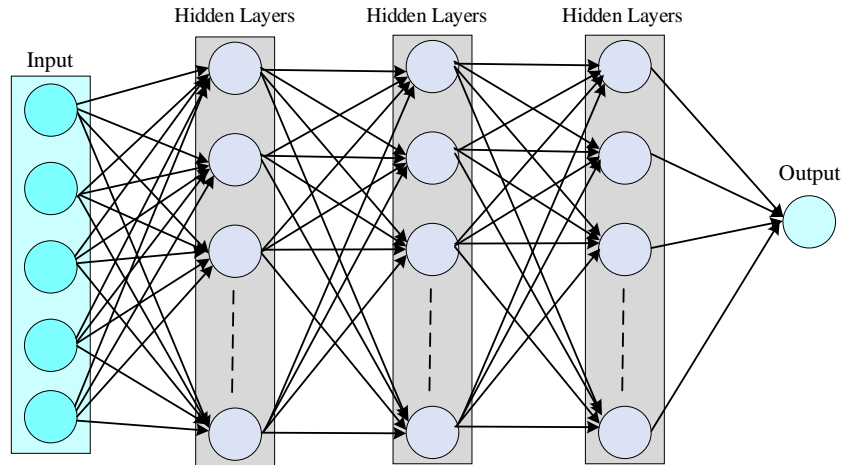


Figure 2. MLP's schematic diagram

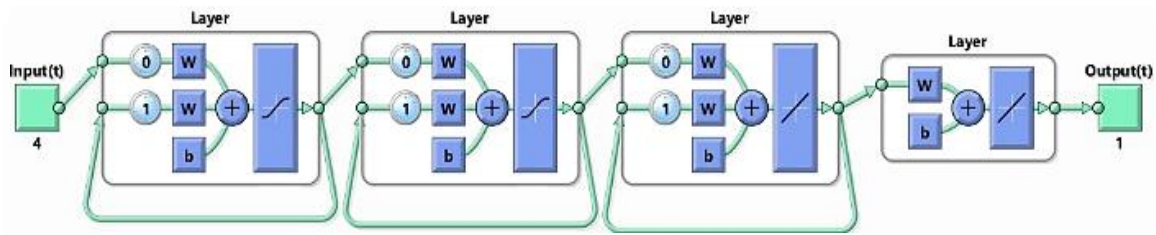


Figure 3. Structure of MLP with 3 hidden layers

retransmitted by the drones between the source and destination. Therefore, the hardware reliability of the receiving drone, the success of the transmission, and the number of transmitters are the factors that define reliable communications. Hence, the reliability of communications (*RoC*) is written as [15]

$$RoC = R(t) \times \left(1 - \prod_{i=1}^n (1 - RoT_i(t)) \right) \tag{1}$$

where *R* is UAV's communication-related hardware reliability. *RoT_i(t)* is the reliability of transmission for the *i_{th}* drone, and *n* is the redundant transmission value. *RoT* can be calculated as [15]

$$RoT(t) = R(t) \times (1 - P_b) \times (1 - P_c) \times (1 - P_f) \tag{2}$$

P_f is the probability of transmission and can be expressed as [2]

$$P_f = \frac{2}{1 + CW + m_r CW / 2} \tag{3}$$

Here, *m_r* is the maximum retransmission limit. Probability of channel busy (*P_b*) can be given as

$$P_b = 1 - (1 - P_f)^N \tag{3}$$

P_c is the probability of collision and can be given as

$$P_c = 1 - (1 - P_f)^{N-1} \tag{4}$$

P_f represents signal loss probability due to channel fading. *P_f*

on Nakagami-*m* channel fading can be expressed as

$$P_f = \frac{m^m}{\Gamma(m)} \times \int_0^{\frac{d}{TR} \alpha} z^{m-1} e^{-mz} dz \tag{6}$$

where *d*, *m*, *TR* and *α* denote the distance between two nodes, Nakagami-*m* fading parameter, transmission range, and path loss exponent, respectively. $\Gamma(\cdot)$ is also standard Gamma function.

3. Multi-Layer Perceptron

The multilayer perceptron (MLP) is built on statistical learning theories that are applicable to making a relationship among input variables and are suitable for solving nonlinear problems [31-32]. In other words, the MLP can connect input and output variables without

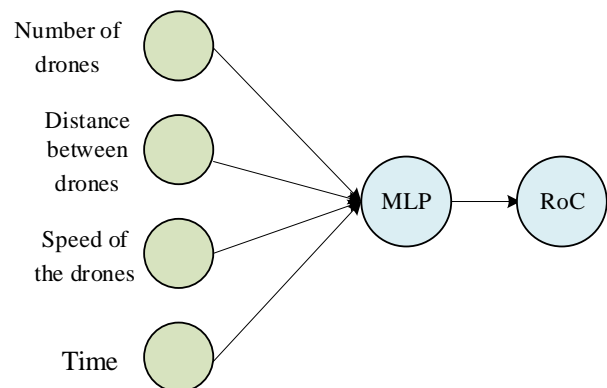


Figure 4. The proposed MLP structure.

Table 1. A dataset of the current study

	Number of drones	Distance between nodes	Speed of drones	Time	Reliability of Communication
1	5	5	10	5	0,3691
2	10	5	10	5	0,3376
3	15	10	20	10	0,1544
4	20	10	50	10	0,3530
5	25	20	30	20	0,0484
6	30	20	20	50	0,0118
7	35	30	40	30	0,0240
8	40	30	10	30	0,0055
9	45	40	50	50	0,0113
10	50	50	30	10	0,0245
11	60	60	40	40	0,0058
12	70	70	50	30	0,0069
13	80	80	70	20	0,0106
14	90	90	80	10	0,0180
15	100	100	90	10	0,0152
16	30	50	30	5	0,0709
17	40	60	40	15	0,022
18	20	20	70	50	0,0494
19	50	5	25	30	0,0689
20	10	15	50	40	0,0703
21	40	10	50	25	0,0988
22	70	25	10	45	0,0026
23	60	45	20	60	0,0026
24	25	60	45	35	0,0138
25	65	70	80	75	0,0048

Input: N, d, v, t

Output: Reliability of communication

1. for $j=1$ to n (number of redundant transmissions)
2. for $j=1$ to N (number of UAVs)
3. calculate P_b (probability of channel busy)
4. END
5. calculate $R(t)$ (reliability of UAV's communication-related hardware)
6. calculate P_l (probability of signal loss)
7. calculate RoT (reliability of transmission)
8. calculate RoC (reliability of communication)
9. END

Figure 5. The proposed structure's pseudo algorithm

requiring complex mathematical and computational methods. MLP is made up of three layers: input, hidden, and output, as displayed in Figure 2. The reliability of communications is included in the output layer. Neurons

in the hidden layers are considered for reliable communication based on the trial and error method. Figure 3 shows the MLP structure, which has three hidden layers.

Figure 4 depicts the proposed MLP structure. The neural network's inputs are made up of four parameters: number of drones (N), velocity of the drones (v), distance between drones (d), and time (t).

The main objective of this work is to estimate the reliability of drones' communication as a target parameter using an MLP algorithm. Various analyses were performed to assess the effectiveness of MLP in the estimation of reliability for drone communication. The obtained results demonstrated that MLP had a high level of ability and accuracy in predicting the intended parameters. The RMSE and MSE for each step of the process were also calculated to demonstrate the performance and applicability of this artificial intelligence approach. Based on the outcomes of this work, it is possible to conclude that MLP could be used as a useful

Table 2. Parameter values used in numerical analysis

Parameters	Values
<i>CW</i>	64
<i>m_r</i>	5
<i>TR</i>	500 m
Activation functions	ReLU + Linear
Hidden layers	1-5
Loss function	MAE
Number of epochs	50
Batch size	50
Dropout	0.4

tool in a variety of industrial processes. Table 1 contains a list of 25 different datasets.

A dataset of drone communication analyses is compiled from various sources. The database was separated into training (50%) and test (50%) sets for the development of the MLP-based models. While the training set is utilized to build models, test sets were used to evaluate and validate the models' generalization capability. Each model's performance is evaluated using statistical quantities such as coefficient of correlation (R^2), RMSE, and MAPE, as defined below;

$$RMSE = \sqrt{\frac{1}{N} \sum_{j=1}^N (P_j - C_j)^2} \tag{7}$$

$$MSE = \frac{1}{N} \sum_{j=1}^N (P_j - C_j)^2 \tag{8}$$

$$MAPE = \frac{1}{N} \sum_{j=1}^N \left| \frac{P_j - C_j}{C_j} \right| \tag{9}$$

$$R^2 = \frac{N \left(\sum_{j=1}^N P_j C_j \right) - \left(\sum_{j=1}^N P_j \right) \left(\sum_{j=1}^N C_j \right)}{\sqrt{\left(N \sum_{j=1}^N (P_j)^2 - \left(\sum_{j=1}^N P_j \right)^2 \right) \left(N \sum_{j=1}^N (C_j)^2 - \left(\sum_{j=1}^N C_j \right)^2 \right)}} \tag{10}$$

Table 3. Comparisons of correlation equations in each different scenario

Number of hidden layers	Number of neurons	R-Squared	RMSE	MSE	MAPE
1	3	0.9907	0.0481	0.0023	0.0098
3	1	0.9643	0.0537	0.0029	0.0101
5	4	0.9939	0.0409	0.0017	0.0096

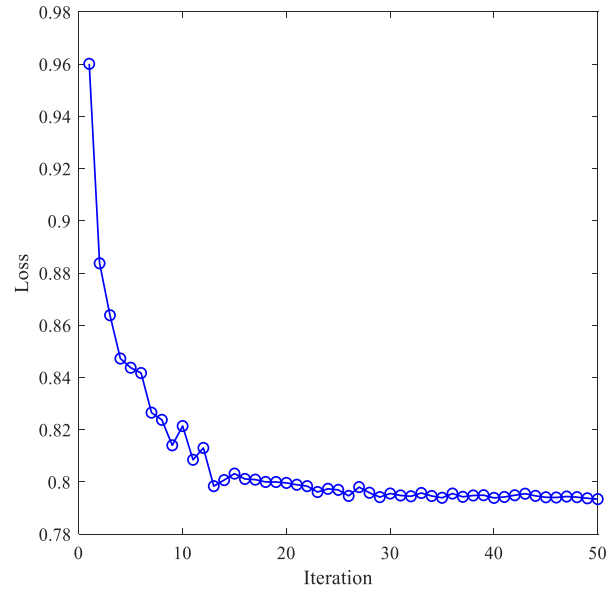


Figure 6. Loss of the MLP during training

where C is the calculated value, and P is the estimated value.

4. Numerical Results

In this section, the effect of MLP on communication reliability in FANETs is assessed. MATLAB is used to generate numerical results. Table 2 lists the parameter values used in numerical analysis.

We can learn about MLP models by observing how they perform during training. Figure 6 depicts the epoch-by-epoch loss of training data. Loss of the MLP during training is decreasing with the increase in the number of iterations.

Table 3 compares all correlation equations under various scenarios. The MLP with one and five hidden layers performs better than the MLP with three hidden layers, as seen in Table 3. Because there are three neurons in a system with one hidden layer whereas there is only one in a system with three hidden layers, the findings from one hidden layer are better than those from three hidden layers. Five hidden layers provide the highest prediction ability, as evidenced by their high correlation coefficient (0.9939), low RMSE (0.0409), MSE (0.0017), and MAPE (0.0096).

Data collection is a critical issue and an active research topic in machine learning. As far as we are aware, there is no dataset available for estimating the reliability of drone communications. The analytical reliability estimate is then used to construct a dataset. After determining the reliability of drone communications for different values of the four criteria taken into account, a dataset is created to train the specified MLP. There are 25 sets in the dataset, and the predicted reliability and the four inputs each have different values.

Due to its higher correlation coefficient and lower RMSE and MAPE compared to the other instances, the MLP with five hidden layers and four neurons in the hidden layer is found to be the best network. Additionally, the correlation coefficient rises and the error rate falls as the number of neurons increases.

5. Conclusion

Reliable packet delivery is one of the communication challenges in FANETs that must be accomplished before drone services can be used. In this study, we use an MLP-based model to estimate drone communication reliability. A dataset is created. An analytical approach based on Markov model is presented to obtain reliability related parameters. Analytical studies are verified by numerical results. The correlation coefficient, RMSE, MSE, and MAPE are obtained for different models. The MLP with five hidden layers and four neurons is demonstrated to be the best network when compared to the other models owing to its better correlation coefficient and lower MSE, RMSE, and MAPE values.

Declaration

Regarding the research, writing, and/or publishing of this paper, the authors reported that they had no potential conflicts of interest. The authors further said that no specific authorization or approval from an ethical committee was needed because this article was entirely original and created in conformity with international publication and research ethics.

Author Contributions

A. F. M. S. Shah developed the methodology, supervised and proofread the manuscript. M. A. Karabulut performed the analysis. The authors wrote the manuscript together.

References

1. A. F. M. S. Shah, *A Survey From 1G to 5G Including the Advent of 6G: Architectures, Multiple Access Techniques, and Emerging Technologie*, in Proc. of IEEE 12th Annual Computing and Communication Workshop and Conference (CCWC). 2022. Las Vegas, NV, USA: p. 1117-1123.
2. A. F. M. S. Shah, Haci Ilhan and Ufuk Tureli, *Designing and Analysis of IEEE 802.11 MAC for UAVs Ad Hoc Networks*, in Proc. of IEEE 10th Annual Ubiquitous Computing, Electronics & Mobile Communication Conference (UEMCON). 2019. New York, USA: 2019. p. 0934-0939.
3. Shah A. F. M. S. , Karabulut M. A. *Optimization of drones communication by using meta-heuristic optimization algorithms*, Sigma Journal of Engineering and Natural Sciences. 2022. **40**(1): p. 108-117.
4. Surzhik D. I., G. S. Vasilyev and O. R. Kuzichkin, *Development of UAV trajectory approximation techniques for adaptive routing in FANET networks*, 7th International Conference on Control, Decision and Information Technologies (CoDIT), 2020. p. 1226-1230.
5. Bhardwaj V. and N. Kaur, *An efficient routing protocol for FANET based on hybrid optimization algorithm*, International Conference on Intelligent Engineering and Management (ICIEM), 2020. p. 252-255.
6. AlKhatieb A., E. Felemban and A. Naseer, *Performance Evaluation of Ad-Hoc Routing Protocols in FANETs*, IEEE Wireless Communications and Networking Conference Workshops (WCNCW), 2020. p. 1-6.
7. Lakew D. S., U. Sa'ad, N. -N. Dao, W. Na and S. Cho, *Routing in Flying Ad Hoc Networks: A Comprehensive Survey*, in *IEEE Communications Surveys & Tutorials*, 2020. **22**(2): p. 1071-1120.
8. Akdemir B., Karabulut M. A. and Ilhan H., *Performance of Deep Learning Methods in DF Based Cooperative Communication Systems*, IEEE International Black Sea Conference on Communications and Networking (BlackSeaCom), 2021. p. 1-6.
9. Karabulut M. A., Shah A. F. M. S. and Ilhan H., *Performance Optimization by Using Artificial Neural Network Algorithms in VANETs*, 42nd International Conference on Telecommunications and Signal Processing (TSP), 2019. Budapest, Hungary: p. 633-636.
10. Belbachir A., J. Escareno, E. Rubio, and H. Sossa, *Preliminary results on UAV-based forest fire localization based on decisional navigation*, in Proceedings of the Workshop on Research, Education and Development of Unmanned Aerial Systems, 2015. p. 377-382.
11. Zhao Z. and T. Braun, *Topology Control and Mobility Strategy for UAV Ad-hoc Networks: A Survey*, in Proceedings of the ERCIM eMobility and MobiSense Workshop, 2013. p. 1-6.
12. Gu W., Valavanis K.P., Rutherford, M.J. et al. *UAV Model-based Flight Control with Artificial Neural Networks: A Survey*. J Intell Robot Syst, 2020. **100**: p. 1469-1491.
13. Sanna G., S. Godio and G. Guglieri, *Neural Network Based Algorithm for Multi-UAV Coverage Path Planning*, International Conference on Unmanned Aircraft Systems (ICUAS), 2021. p. 1210-1217.
14. Liu H., K. Fan and B. He, *Acoustic Source Localization for Anti-UAV Based on Machine Learning in Wireless Sensor Networks*, 15th IEEE Conference on Industrial Electronics and Applications (ICIEA), 2020. p. 1142-1147.
15. Bahramnejad S., Movahhedinia N. *A reliability estimation framework for cognitive radio V2V communications and an ANN-based model for automating estimations*, Computing, 2022. **104**: p. 1923-1947.
16. Benrhaiem W, Senhaji HA. *Bayesian networks-based reliable broadcast in vehicular networks*, Veh Commun, 2020. 21: p. 1-13.
17. Hassija V. et al., *Fast, Reliable, and Secure Drone Communication: A Comprehensive Survey*, in *IEEE*

- Communications Surveys & Tutorials, 2021. **23**(4): p. 2802-2832.
18. Faisal SM, Zaidi T. *Implementation of ACO in VANETs with detection of faulty node*, Indian J Sci Technol 2021. **14**(19): p. 1598–1614.
 19. G. Sun, D. Qin, T. Lan and L. Ma, *Research on Clustering Routing Protocol Based on Improved PSO in FANET*, in IEEE Sensors Journal, 2021. **21**(23): p. 27168-27185.
 20. Bhandari S., X. Wang and R. Lee, *Mobility and Location-Aware Stable Clustering Scheme for UAV Networks*, in IEEE Access, 2020. 8: p. 106364-106372.
 21. Ghaleb FA, Zainal A, Rassam MA, Mohammed F. *An effective misbehavior detection model using artificial neural network for vehicular ad hoc network applications*, IEEE Conference on Application, Information and Network Security, 2017. p. 13–18.
 22. Bagherlou H, Ghaffari A. *A routing protocol for vehicular ad hoc networks using simulated annealing algorithm and neural networks*, J Supercomput, 2018. **74**: p. 2528–2552.
 23. Jindal A, Aujla GS, Kumar N, Chaudhary R, Obaidat MS, You I. *SeDaTiVe: SDN-enabled deep learning architecture for network traffic control in vehicular cyber-physical systems*, IEEE Netw, 2018. **32**(6): p. 66–73.
 24. Gismalla M. S. M. et al., *Survey on Device to Device (D2D) Communication for 5GB/6G Networks: Concept, Applications, Challenges, and Future Directions*, in IEEE Access, 2022. **10**: pp. 30792-30821.
 25. Karabulut M A, Shahan S A F M, Ilhan H. *Performance optimization by using artificial neural network algorithms in VANETs*, International Conference on Telecommunications and Signal Processing, 2019. p. 633–636.
 26. Challita, U. Ferdowsi, A. Chen, M. Saad, W. *Machine learning for wireless connectivity and security of cellular-connected UAVs*, IEEE Wirel. Commun, 2019. **26**: p. 28–35.
 27. Ren M., J. Li, Song L., Li H. and Xu T., *MLP-Based Efficient Stitching Method for UAV Images*, in IEEE Geoscience and Remote Sensing Letters, 2022. **19**: p. 1-5.
 28. Braga J. R. G., Velho H. F. C., Conte G., P. Doherty and É. H. Shiguemori. *An image matching system for autonomous UAV navigation based on neural network*, 14th International Conference on Control, Automation, Robotics and Vision (ICARCV), 2016. p. 1-6.
 29. Shan L., Miura R., Kagawa T., Ono F., H. -B. Li and Kojima F., *Machine Learning-Based Field Data Analysis and Modeling for Drone Communications*, in IEEE Access, 2019. **7**: p. 79127-79135.
 30. Munaye Y.Y., Lin H-P., Adege A.B., Tarekegn G.B. *UAV Positioning for Throughput Maximization Using Deep Learning Approaches*, Sensors. 2019; **19**(12):2775.
 31. Wang Y. *Robot algorithm based on neural network and intelligent predictive control*, Amb Intel Hum Comp, 2020. **11**: p. 6155–6166.
 32. Taud H., Mas J. *Multilayer Perceptron (MLP)*. In: Camacho Olmedo, M., Paegelow, M., Mas, JF., Escobar, F. (eds) Geomatic Approaches for Modeling Land Change Scenarios. Lecture Notes in Geoinformation and Cartography. Springer, Cham. 2018.



Research Article

Effects of advanced oxidation process on greywater treatment: an optimization study

Özlem Demir ^{a,*}  and Ezgi Sühel Aktaş ^b 

^aHarran University, Faculty of Engineering, Department of Environmental Engineering, Şanlıurfa, 63000, Turkey

^bHarran University, Graduate School of Natural And Applied Science, Şanlıurfa, 63000, Turkey

ARTICLE INFO

Article history:

Received 22 March 2022

Accepted 09 September 2022

Published 15 December 2022

Keywords:

Advanced oxidation methods

Fenton process

Fe₃O₄ magnetic nanoparticle

KMnO₄

ABSTRACT

Greywater is domestic wastewater from showers and sinks and has a significant potential for the protection of water resources as it is less polluted in terms of nutrients, inorganic substances and hazardous organic substances. It is aimed to treat and reuse greywater in order to meet the rapidly increasing water demand. In this research, the treatment of greywater using the Fenton Process was studied. The efficiency of the Fenton Process was optimized using the Box-Behnken Statistical Design Software. As a result of this study, 97.88 % of Chemical Oxygen Demand removal was achieved at pH = 3, Fe²⁺ dose of 3 mM, H₂O₂ dose of 2 mM, and 37 min. The effect of Potassium Permanganate on the treatability of synthetic greywater was also investigated in the study. Results showed that 84% of the Chemical Oxygen Demand removal efficiency could be achieved using 0.1 g/L Potassium Permanganate at the end of 1 hour reaction time.

1. Introduction

In recent years, fresh water resources in the world have been gradually decreasing, and new water resources are becoming more limited and expensive. For these reasons, efforts are ongoing to find new alternatives to be able to meet the water demand. Today, new sources are investigated to decrease water demand through reusing waste water. Greywater can be used as one of these sources.

Greywater is one of the alternative sources in terms of water, especially in semi-arid or arid regions [1]. Greywater is wastewater occurring due to some systems such as bathrooms, showers, handwash, sinks, dishwashers, washing machines, and kitchen sinks [2]. Soap and detergents are the most important pollutants in greywater. However, it is generally less polluted than urban wastewater because it does not contain human feces and toilet paper [3].

Greywater can be categorized as dark greywater and light greywater. While dark greywater is the source of kitchen sinks, light greywater contains water from bathrooms, toilet sinks, bathtubs, showers, washing machines and similar sources. Dark greywater contains

disease-causing microorganisms and a large number of organic contaminants from nutrient residues, oil, and fat. In terms of organic pollutants, greywater is cleaner than other wastewater [4]. In addition, regarding organic matter and solids content, greywater can be categorized under two groups. Greywater from the kitchen contains surfactants such as detergents, as well as a high organic and solid content. On the other hand, greywater from bathrooms and sinks is defined as "low load" greywater that is poor in organic matter and solids. [5].

With 75% of the total volume, greywater constitutes the largest portion of the total domestic wastewater. It contains between 3% and 10% nitrogen and phosphorus but has a low pollution potential because it contains organic matter, which makes up 40% of the total. Greywater contains 23% of the total suspended solids in domestic wastewater. In terms of pathogens, there is almost no hygienic concern because greywater is not contaminated with toilet wastewater [6]. Greywater can be reused after the treatment because it is less polluted than other wastewater. Today, numerous processes are evaluated and implemented to treat greywater. Treated greywater can be used in many areas in homes and industry such as irrigation, washing of vehicles, fire

* Corresponding author. Tel.: +90-414-318-3000 / 3791.

E-mail addresses: odemir@harran.edu.tr (Ö. Demir), ezgisuhelaktas@harran.edu.tr (E.S. Aktaş)

ORCID: 0000-0002-0727-1845 (Ö. Demir), 0000-0001-7298-0720 (E.S. Aktaş)

DOI: [10.35860/iarej.1091551](https://doi.org/10.35860/iarej.1091551)

© 2022, The Author(s). This article is licensed under the CC BY-NC 4.0 International License (<https://creativecommons.org/licenses/by-nc/4.0/>).

response, production, toilet, and flush [7,8].

The greywater characterization and type of reuse application are crucial in order to determine the treatment process [9,10,11]. Filtration, precipitation and sedimentation, and membrane techniques are the most common physicochemical methods. Constructed wetland, rotating biological contactor (RBC), and membrane bioreactor (MBR) are the most used biological process for the treatment of greywater [10]. Although they are effective in greywater treatment, they are not successful enough in removing refractory and toxic materials. Therefore, alternative treatment methods should be investigated. Advanced oxidation processes can be suggested to solve this problem [12].

Advanced oxidation processes are one of the new applications used in water and wastewater treatment technologies and they are related to the mechanism of hydroxyl radical (OH) production emerging as a result of oxidative degradation of organics. Thanks to these processes, refractory organic compounds are converted into biodegradable compounds, and then they are mineralized into the water by giving CO₂ and inorganic anions. The dark oxidation process, homogeneous and heterogeneous photocatalytic oxidation, the Fenton and photo-Fenton processes, sonolysis, and hydrothermal and wet oxidations can be shown as examples to advanced oxidation processes [13].

Potassium Permanganate (KMnO₄) is a crystalline inorganic chemical substance that is found in solid form and consists of potassium and manganate ions with a molar mass of 158,034 g/mol, the density of 2,70 g/cm³, and melting point >240°C. Potassium Permanganate, a strong oxidizer, gives an intense pink-violet color when dissolved in water, and gradually turns brown when combined with oxidizable substances in the environment [14]. KMnO₄ is a crystalline, easy-to-use compound that dissolves up to 5% in water and is widely used to convert manganese ions to manganese dioxide (MnO₂) and is a stronger oxidant than chlorine. Unlike chlorine, the reaction of KMnO₄ with organic compounds does not cause Trihalomethane (THM) formation and causes a decrease in THMs [15]. Potassium Permanganate is an oxidizing agent used in water treatment. It oxidizes organic substances in the water and is thus removed from the water by filtration [14]. KMnO₄ is also a powerful oxidant and is used in the disinfection of water and the oxidation of toxic substances. The advantages of KMnO₄ compared to ozone and chlorine used as other oxidants are that it is non-toxic and safe to use [16]. Potassium Permanganate forms in the water industry are highly reactive [17]. KMnO₄ in water precipitates by reducing it to manganese dioxide. Reaction rates for the oxidation of its components in natural waters are relatively high and depend on temperature, pH, and concentration [14].

In the present research, the treatment of synthetic greywater by using the Fenton Process was studied. pH, Fe²⁺ dose, H₂O₂ dose, and time were determined as the parameters affecting the Fenton Process. These parameters were optimized using Box-Behnken Statistical Design Program. To the knowledge of the authors, the performance of KMnO₄ in greywater treatment is discussed for the first time in the literature in this study.

2. Material and Methods

2.1 Greywater Characteristics

In the present study, greywater was prepared synthetically and was used directly without any pretreatment method. The synthetic greywater was prepared according to the composition given in Table 1.

The effluent from the wastewater treatment plant was also prepared synthetically by adding some chemicals given in Table 2 into the tap water.

2.2 Greywater Treatment using the Fenton Process

2.2.1 Experimental Procedure and Box-Behnken Statistical Design

The performance of the Fenton Process on synthetic greywater treatment was investigated. To be able to optimize the parameters (pH, Fe²⁺, and H₂O₂ doses and reaction time), the Box-Behnken Statistical Design method was utilized.

The ranges for the variables were 0.3-3 mM for Fe²⁺, 2-20 mM for H₂O₂ and 10-60 minutes for reaction time. The Box-Behnken Statistical Design Program suggested 27 experimental runs for 4 variables. Design variables and experimental runs were given in Table 3.

Table 1. Composition of synthetic greywater [14]

Material	Quantity
Tap Water	5 L
Oil	0.05 mL
the effluent of Wastewater Treatment Plant	12 mL
Soap	3.2 g
Shampoo	4 mL

Table 2. Wastewater Treatment Plant Effluent Characterization

Chemicals	Quantity
CH ₃ COONa.3H ₂ O	19.89 mg/L
Sucrose	10.6 mg/L
NH ₄ Cl	8.1 mg/L
KH ₂ PO ₄	4 mg/L
K ₂ HPO ₄	4 mg/L
MgSO ₄ .7H ₂ O	4 mg/L

Table 3. Design variables and experimental runs

Variables	Unit	Max Value	Min Value	
pH		3	5	
Fe ²⁺	mM	0.3	3	
H ₂ O ₂	mM	2	20	
Time	Min	10	60	
Analysis No	pH	Fe ²⁺ (mM)	H ₂ O ₂ (mM)	Time (min)
1	4	3	2	35
2	3	3	11	35
3	4	1.65	11	35
4	4	0.3	2	35
5	5	1.65	11	60
6	4	1.65	11	35
7	5	1.65	11	10
8	4	1.65	2	60
9	3	1.65	2	35
10	3	1.65	11	10
11	5	1.65	20	35
12	4	1.65	20	10
13	4	1.65	20	60
14	4	0.3	20	35
15	5	0.3	11	35
16	3	0.3	11	35
17	3	1.65	11	60
18	3	1.65	20	35
19	4	3	11	10
20	4	1.65	2	10
21	4	1.65	11	35
22	5	3	11	35
23	4	3	20	35
24	4	0.3	11	60
25	4	3	11	60
26	4	0.3	11	10
27	5	1.65	2	35

For each experiment, the following procedure was followed.

- 300 mL of the synthetic greywater sample was used.
- pH was adjusted using 1 N H₂SO₄ and 1 N NaOH.
- Fe²⁺ and H₂O₂ were added based on the experimental run using FeSO₄·7H₂O and H₂O₂.
- The greywater solutions consist of Fe²⁺ and H₂O₂ doses were mixed at 150 rpm depending on the reaction time of the experimental run.
- At the end of the reaction process, the pH was adjusted to 7 and it was kept under static conditions for 1-1.5 hours to settle the formed flocs.
- The filtration of the sample was carried out using a 0.45 µm membrane filter and then 2.5 mL of the sample was used for Chemical Oxygen Demand (COD) analyses. The COD removal efficiencies were calculated by using the difference between the initial COD and COD after the Fenton Process.

2.3 Greywater Treatment Using KMnO₄

2.3.1 Experimental Procedure and Box-Behnken Statistical Design

Experimental studies were conducted using 100-600 g/L KMnO₄ to investigate the effects of KMnO₄ concentrations on the COD removal efficiency of greywater and to determine the concentration and time that provides maximum COD removal efficiency. pH was 7.56, the reaction time was varied as 30 minutes, 1 hour, and 2 hours. Different KMnO₄ doses are given in fixed times in Table 4.

300 mL of synthetic greywater sample was put in a beaker. The determined concentration of KMnO₄ was added to the sample, and the solution was mixed at 200 rpm for 3 minutes, then the mixing speed was decreased. At the end of the reaction process, it was waited for one hour for the floc formation via precipitation. Afterward, the centrifuge process of the treated water was performed at 3000 rpm for 5 minutes. Then, the water was filtered with a 0.45 µm membrane filter and analyzed for COD.

2.4 Analytic Methods

All COD analyzes were performed based on the standards of the Closed Reflux Method [18]. pH measurement of the samples was carried out using a Hach pH meter.

3. Results and Discussion

3.1 Greywater Characteristics

In the experiments, greywater was prepared synthetically and kept in the refrigerator. The results of the characterization studies of the synthetic greywater sample were given in Table 5.

Table 4. Different KMnO₄ doses at fixed times

Analysis	KMnO ₄ (mg/L)
1	100
2	200
3	300
4	400
5	500
6	600

Table 5. Graywater characteristics

Parameters	Values
pH	7.56
Temperature (°C)	18.5
Conductivity (µS/cm)	398
Alkalinity (CaCO ₃ /L)	210
Turbidity (NTU)	2121.6
Total Phosphorus (TP) (mg/L)	0.046
Total Nitrogen (TN) (mg/L)	0.048

3.2 Fenton Process Results

3.2.1 Results of the Box-Behnken Statistical Design

The results of the COD analyses were adopted to Box-Behnken Statistical Design Program as given in Table 6.

ANOVA table provided by Box-Behnken Statistical Design Program was given in Table 7. The chart shows that the model was statistically “significant” according to the experiment variables and meaningful results were obtained.

In this study, p values less than 0.05 was accepted statistically significant. As seen in Table 7, Model F 24.37 shows that the model is statistically significant at 0.001 significance level (p<0.001). Here, B-Fe²⁺, C-H₂O₂, B², and C² are seen as statistically significant. The “Fit F-value” of 0.63 implies that Fit Deficiency is not significant (p>0.05) compared to pure error. R-Squared is 0.9660. There is a 74.97% “Fit F-value” chance for this size to occur due to noise. We want the lack of meaningful fit to fit the model. “Pred R²” (0.8332) is in a certain agreement with the “Adjusted R²” (0.9264).

Table 6. Experiment sets and results

Analysis No	pH	Fe ²⁺ (mM)	H ₂ O ₂ (mM)	Time (min)	Effluent CODs (mg/L)	COD Removal (%)
1	4	3	2	35	49.92	93
2	3	3	11	35	30.72	95
3	4	1.65	11	35	74.24	89
4	4	0.3	2	35	125.44	82
5	5	1.65	11	60	107.52	85
6	4	1.65	11	35	80.64	89
7	5	1.65	11	10	116.48	85
8	4	1.65	2	60	57.6	92
9	3	1.65	2	35	38.4	94
10	3	1.65	11	10	112.64	87
11	5	1.65	20	35	145.92	80
12	4	1.65	20	10	153.6	81
13	4	1.65	20	60	168.96	78
14	4	0.3	20	35	234.24	68
15	5	0.3	11	35	157.44	78
16	3	0.3	11	35	156.16	78
17	3	1.65	11	60	110.08	86
18	3	1.65	20	35	160	80
19	4	3	11	10	55.04	93
20	4	1.65	2	10	55.04	93
21	4	1.65	11	35	115.2	85
22	5	3	11	35	58.88	92
23	4	3	20	35	134.4	83
24	4	0.3	11	60	179.2	75
25	4	3	11	60	52.48	93
26	4	0.3	11	10	180.48	77
27	5	1.65	2	35	65.28	92

Table 7. ANOVA Table

Source	Sum of Squares	df	Mean Square	F Value	p-value	Prob>F
Model	1253.55	14	89.54	24.37	<0.0001	significant
A-pH	5.33	1	5.33	1.45	0.2515	
B-Fe ²⁺	690.08	1	690.08	187.85	<0.0001	
C-H ₂ O ₂	481.33	1	481.33	131.02	<0.0001	
D- Time	4.08	1	4.08	1.11	0.3125	
AB	2.25	1	2.25	0.61	0.4490	
AC	1.00	1	1.00	0.27	0.6113	
AD	0.25	1	0.25	0.068	0.7986	
BC	4.00	1	4.00	1.09	0.3173	
BD	1.00	1	1.00	0.27	0.6113	
CD	1.00	1	1.00	0.27	0.6113	
A ²	0.15	1	0.15	0.040	0.8442	
B ²	46.68	1	46.68	12.71	0.0039	
C ²	17.93	1	17.93	4.88	0.0474	
D ²	2.68	1	2.68	0.73	0.4101	
Residual	44.08	12	3.67			
Lack of Fit	33.42	10	3.34	0.63	0.7497	not significant
Pure Error	10.67	2	5.33			
Cor Total	1297.63	26				
Std. Dev.	1.92		R ²			0.9660
Mean	85.30		Adj R ²			0.9264
C.V.%	2.25		Pred R ²			0.8332
PRESS	216.48		Adeq Precision			19.483

Core Total: It expresses the variation amount in the the observations' means. **Adj (Adjusted) R²:** Shows variation that is explained by the studied model around the mean. **Pred R²:** It refers to the variation explained by the model in the new data. **Adeq Precision:** presents the comparison of the predicted value ranges at the design points with the average estimation error.

The coefficients of the Box-Behnken Statistical Design Program were given in Table 8. By putting these coefficients on their places in Equation (1), the real experimental results and predicted results were obtained and presented in Table 9. As can be seen from Table 8, actual test results and predicted values were close to each other.

Equation for Box-Behnken Statistical Design program for 4 variables are given below.

$$y = b_0 + b_1X_1 + b_2X_2 + b_3X_3 + b_4X_4 + b_{12}X_1X_2 + b_{13}X_1X_3 + b_{14}X_1X_4 + b_{23}X_2X_3 + b_{24}X_2X_4 + b_{11}X_1^2 + b_{22}X_2^2 + b_{33}X_3^2 + b_{44}X_4^2 \tag{1}$$

3.3 Optimization Results

3.3.1 Effects of Fe²⁺ and H₂O₂ doses

The graphics provided by the Box-Behnken Statistical Design Program can be utilized for the determination of the optimum Fe²⁺ and H₂O₂ doses and reaction times in terms of the highest values of COD removal efficiency.

Table 8. Equation coefficients

bo	+ 85.41424
b1	- 2.04444
b2	+ 11.77229
b3	- 0.48601
b4	+ 0.016000
b12	- 0.55556
b13	+ 0.55556
b14	+ 1.00000E-002
b23	+ 0.082305
b24	- 2.22222E-003
b11	+ 0.16667
b22	- 1.62323
b33	- 0.022634
b44	- 1.13333E-003

Table 9. Actual test results and predicted test results

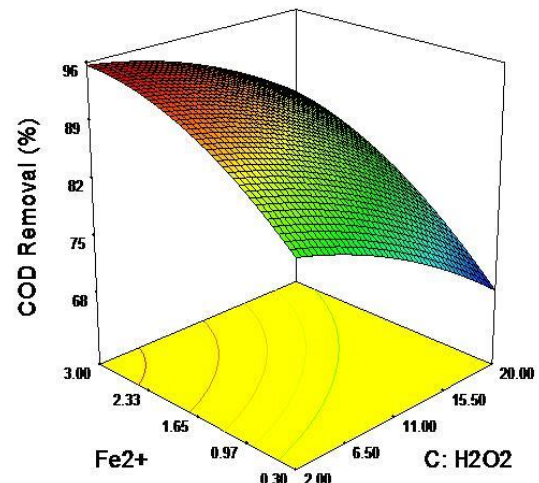
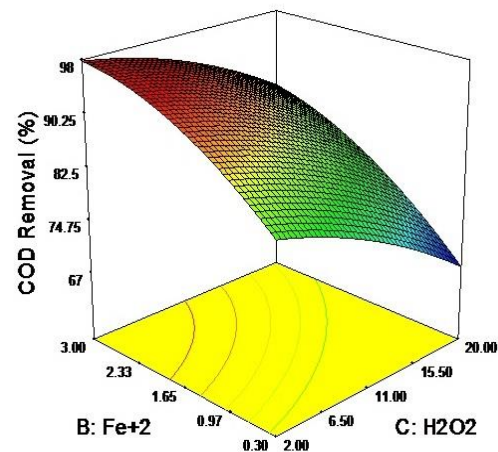
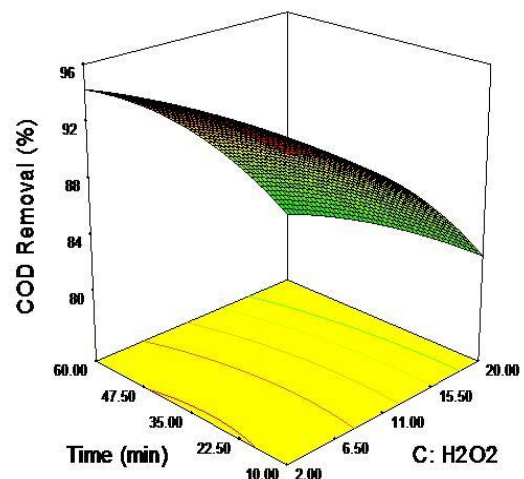
No	pH	Fe ²⁺ (mM)	H ₂ O ₂ (mM)	Time (min)	Effluent CODs (mg/L)	COD Removal (%)	Predicted COD Removal (%)
1	4	3	2	35	49.92	93	95.79
2	3	3	11	35	30.72	95	93.87
3	4	1.65	11	35	74.24	89	87.66
4	4	0.3	2	35	125.44	82	82.62
5	5	1.65	11	60	107.52	85	86.12
6	4	1.65	11	35	80.64	89	87.66
7	5	1.65	11	10	116.48	85	86.79
8	4	1.65	2	60	57.6	92	91.54
9	3	1.65	2	35	38.4	94	93.5
10	3	1.65	11	10	112.64	87	88.62
11	5	1.65	20	35	145.92	80	79.5
12	4	1.65	20	10	153.6	81	79.87
13	4	1.65	20	60	168.96	78	77.7
14	4	0.3	20	35	234.24	68	67.95
15	5	0.3	11	35	157.44	78	77.37
16	3	0.3	11	35	156.16	78	77.2
17	3	1.65	11	60	110.08	86	86.95
18	3	1.65	20	35	160	80	79.83
19	4	3	11	10	55.04	93	91.66
20	4	1.65	2	10	55.04	93	91.54
21	4	1.65	11	35	115.2	85	87.66
22	5	3	11	35	58.88	92	91.04
23	4	3	20	35	134.4	83	85.12
24	4	0.3	11	60	179.2	75	75.33
25	4	3	11	60	52.48	93	91.5
26	4	0.3	11	10	180.48	77	77.5
27	5	1.65	2	35	65.28	92	91.16

The graph of Fe²⁺ versus H₂O₂ is given in Figure 1. In this figure, time was fixed as 30 min and pH was 4. The highest COD removal efficiency was achieved with 95.68% at the dose of 2 mM H₂O₂ and 3 mM Fe²⁺.

Considering the changes in H₂O₂ versus Fe²⁺ at a fixed time of 30 minutes and pH = 3, it was observed that the highest COD removal (97.81%) was at the dose of 2 mM H₂O₂ and 3 mM Fe²⁺ (Figure 2).

3.3.2 Effects of Time

Considering the time versus H₂O₂ dose at 2 mM fixed Fe²⁺ dose and pH = 3 (Figure 3), the highest COD removal efficiency (95.21 %) was achieved with 2 mM of H₂O₂ dose at a time of 30 minutes.

Figure 1. Fe²⁺ versus H₂O₂ at pH = 4, time= 30 minFigure 2. Fe²⁺ versus H₂O₂ at pH = 3, time= 30 minFigure 3. Time versus H₂O₂ at pH = 3, Fe²⁺=2 mM

For the 2 mM fixed H_2O_2 dose and $\text{pH} = 3$, time and Fe^{2+} dose changes are given in Figure 4. The highest COD removal efficiency (97.88 %) was achieved in the experiment conducted with 3 mM Fe^{2+} dose and at 37 minutes.

Finally, considering the graphic of Fe^{2+} versus H_2O_2 at $\text{pH} = 3$ and 37 min, the maximum removal efficiency (97.88%) was observed at 2 mM of H_2O_2 dose and 3 mM of Fe^{2+} dose (Figure 5).

In a study conducted by Blanco et al. [19], Fenton oxidation and its combination with aerobic Sequencing Batch Reactor (SBR) were examined in terms of reusing textile wastewater. They optimized H_2O_2 , temperature, and $\text{Fe}(\text{II})$ concentrations as independent variables. Results showed that >99 % *E.coli* removal efficiency and 64% TOC reduction were achieved by Fenton oxidation at condition where $Y=25^\circ\text{C}$, $\text{H}_2\text{O}_2 = 1650 \text{ mg/L}$, $\text{pH} = 3$, and $\text{Fe}(\text{II}) = 216 \text{ mg/L}$. In condition where SBR was used for 1 day, TOC reduction and *E.coli* removal efficiency were determined as 92% and >99% at $\text{H}_2\text{O}_2=1582 \text{ m/L}$ and $\text{Fe}(\text{II}) = 66.5 \text{ mg/L}$, respectively [19].

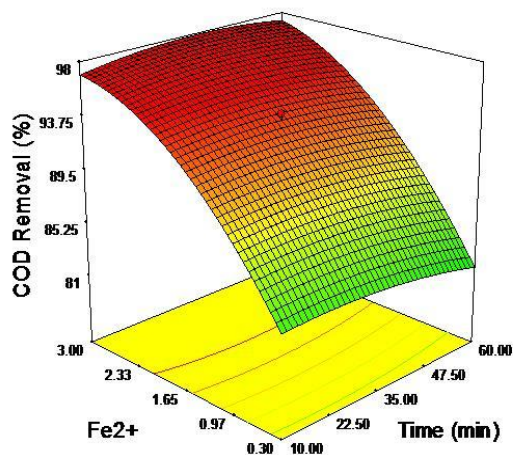


Figure 4. Time versus Fe^{2+} at $\text{pH} = 3$, $\text{H}_2\text{O}_2=2 \text{ mM}$

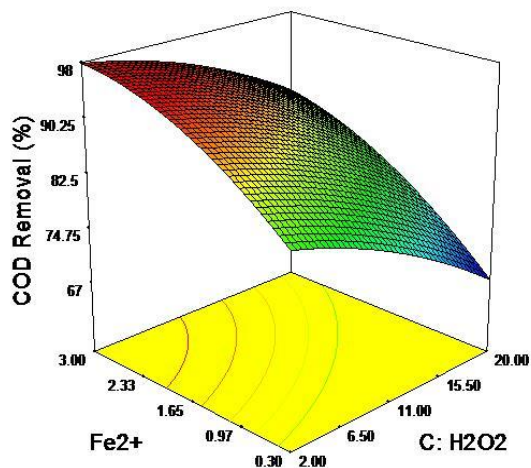


Figure 5. Fe^{2+} versus H_2O_2 at $\text{pH} = 3$, time=37 min

In the study carried out by Öztürk [10], the recovery of greywater from UV-assisted electrocoagulation was achieved. In the first study, the optimum operating conditions of the electrocoagulation process were determined as the raw water pH value 7.4 ± 0.2 , $1 \text{ g Na}_2\text{SO}_4 / \text{L}$ electrolyte addition, 3 mA/cm^2 current density, and 40 minutes process time. Under these optimum conditions, 88.1% COD and 97.2% turbidity removal efficiencies were achieved using Al electrodes, while 79.3% COD and 99.4% turbidity removal efficiencies were obtained using Fe (iron) electrodes. TS (Suspended Solids), TN, TP, and BOD_5 parameters were 62.3%, 44%, 98%, and 88.5%, respectively. In the presence of iron electrode, 80.6%, 8.5%, 98.4%, and 78.46% removal efficiencies were obtained, respectively. Tony et al. [20] achieved maximum COD removal efficiency (95%) using the Fenton process for the treatment of greywater under condition where $\text{pH} = 3$, $\text{H}_2\text{O}_2= 200 \text{ mg/L}$, and $\text{Fe}^{3+}= 40 \text{ mg/L}$. Thirugnanasambandham and Sivakumar investigated the treatability of greywater using Electro Fenton Process [21]. In their study, under conditions where current density was 10 mA/cm^2 , treatment time was 14 min, $\text{H}_2\text{O}_2/\text{Fe}^{2+}$ molar ratio was 0.70, and pH was 4, COD and TSS removal efficiencies were achieved 90% and 85%, respectively. In the study conducted by Özgüroğlu [22], the removal of COD, anionic and non-ionic surfactant parameters of greywater by the classical Fenton application was investigated. Under the optimum conditions ($\text{Fe}^{2+} = 50\text{mg/L}$, $\text{pH} = 7.4$, and $\text{H}_2\text{O}_2= 50\text{mg/L}$) determined through the classical Fenton application, the removal efficiencies of 99.9%, 99.45%, and 75% were achieved for anionic surfactants, non-ionic surfactants, and COD, respectively [22]. Hassanshahi and Karimi-jahnsni studied the comparison and optimization of greywater treatment performance using the processes called photocatalysis, photo-Fenton, and ozone / H_2O_2 / UV. In these three processes, the highest COD removal efficiencies were achieved as 55%, 90%, and 92%, respectively. The ozone / H_2O_2 / UV process was suggested for greywater treatment with 92% and 93% removal efficiencies for COD and turbidity, respectively [23]. In another study conducted by Faggiano et al., [24], the treatment of greywater using the combination of photo-driven advanced oxidation (P-AOP) and physical foam fractionation was examined. As a result of the study, COD removal efficiencies of 63.8% and 30.2% were achieved through photo-Fenton and P-AOPs, respectively. On the other hand, in the foam fractionation processes, the removal of COD was 95.3%. When the UV-C light source was replaced with sunlight, it was observed that there was a decrease from 95.3% to 89.5% in the COD removal efficiency [24]. By using *Pseudomonas aeruginosa*, which is an indicator microorganism, Teodoro et al. [25] investigated the performance of the photo-Fenton and some other advanced oxidation processes in terms of

the treatment of greywater. The H_2O_2 concentration was vary from 25 to 150 mg/L at 10 mg/L of the Fe^{2+} concentration and the pH=3. There was no difference in treatment at high H_2O_2 concentrations. Besides, the results obtained in the H_2O_2/UV process with the concentration of 150 mg/L H_2O_2 were similar to the results obtained in the pH-adjusted system.

3.4 $KMnO_4$ Oxidation

3.4.1 Effect of $KMnO_4$ Concentration

At this stage of the study, the effect of $KMnO_4$ on the treatability of greywater was investigated. The experimental studies were carried out with a variety of $KMnO_4$ concentrations on COD removal efficiency. Effects of different $KMnO_4$ doses on COD removal efficiency in 30 minutes fixed time were summarized in table 10.

The raw greywater COD of 1376 mg/L was subjected to a reaction time of 3 minutes at 200 rpm first, and then 30 minutes at 50 rpm in a jar test. And during the experiments, a color in eggplant purple tones was observed as a result of adding $KMnO_4$ into greywater. As a result of the COD analysis performed after the period was completed, the highest removal efficiency was obtained as 71% at the concentration of 0.1 g/L.

Under experimental conditions, raw greywater COD of 1203.2 mg/L was subjected to a reaction time of 3 minutes at 200 rpm, then 1 hour at 50 rpm in a jar test. The highest COD removal efficiency (83%) was obtained at a concentration of 0.1 g/L. The effects of different $KMnO_4$ doses on COD removal efficiency in 1 hour fixed time were summarized in Table 11.

The raw greywater of COD 1459.2 mg/L was subjected to a reaction time of 3 minutes at 200 rpm and then 2 hours at 50 rpm in a jar test. The highest COD efficiency was determined as 84% at 0.1 g/L concentration. The effects of different $KMnO_4$ doses on COD removal efficiency in 2 hours fixed time were summarized in Table 12.

COD removal efficiencies achieved as a result of the treatment with the $KMnO_4$ addition at different reaction times, 0.1-0.6 g/L range, and pH value 7.48 are shown in Figure 6. Based on the figure, it can be concluded that the highest COD removal efficiency of synthetic greywater (84%) was achieved with 0.1 g/L $KMnO_4$ concentration at the end of 2 hours of reaction time. However, at a concentration of 0.1 g/L $KMnO_4$, as a result of the 1-hour treatment, a yield (83%) very close to the highest COD removal efficiency was achieved. Therefore, the optimum concentration is considered 0.1 g/L $KMnO_4$ and the most appropriate time can be accepted as 1 hour.

In addition, by using 0.1 g/L of $KMnO_4$, the maximum COD removal efficiency (83 %) was obtained at 60 min of reaction time.

Table 10. Effects of different $KMnO_4$ doses on COD removal efficiency in 30 minutes fixed time

Analysis	$KMnO_4$ (g/L)	Time(min)	Remained COD (mg/L)	COD Removal (%)
1	0.1	30	396.8	71
2	0.2	30	504.32	63
3	0.3	30	550.4	59
4	0.4	30	532.48	61
5	0.5	30	524.8	61
6	0.6	30	519.68	62

Table 11. Effects of different $KMnO_4$ doses on COD removal efficiency in 1 hour fixed time

Analysis	$KMnO_4$ (g/L)	Time (hour)	Remained COD (mg/L)	COD Removal (%)
1	0.1	1	199.68	83
2	0.2	1	299.52	75
3	0.3	1	216.32	82
4	0.4	1	209.92	82
5	0.5	1	215.04	82
6	0.6	1	254.72	78

Table 12. Effects of different $KMnO_4$ doses on COD removal efficiency in 2 hours of fixed time

Analysis	$KMnO_4$ (g/L)	Time (hour)	Remained COD (mg/L)	COD Removal (%)
1	0.1	2	230.4	84
2	0.2	2	364.8	75
3	0.3	2	748.8	48
4	0.4	2	684.8	53
5	0.5	2	646.4	55
6	0.6	2	608	58

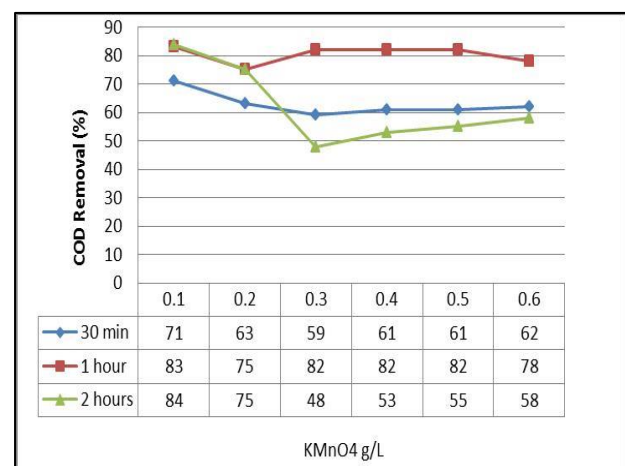


Figure 6. The effect of $KMnO_4$ on COD removal efficiency

4. Conclusion

In this study, firstly, the treatment performance of greywater using the Fenton Process, which has become attractive due to the advantages such as high efficiency, easy availability of the chemicals used, low investment cost

and short hydraulic retention time, was investigated. The Box-Behnken Statistical Design Program was applied to Fenton Process for greywater treatment to be able to reduce the number of experiments and provide an estimation of the untested experimental conditions in the light of the coefficients provided by the program. During this application, variable parameters affecting the process, pH, Fe²⁺ and H₂O₂ dose, and the effect of time were evaluated.

As a result of the study, the optimum value of pH was chosen as 3. Then, the optimum dose of Fe²⁺ was determined as 3 mM. 2Mm and time of 37 min were determined as the optimum dose of H₂O₂ and reaction time, respectively.

In addition, as a strong oxidant, KMnO₄ was used to investigate its effect on the greywater treatability. KMnO₄ concentration range was determined as 0.1-0.6 g/L and time variation was determined as 30 minutes, 1 hour, and 2 hours. At the end of the 60 min reaction time, the highest COD removal efficiency was achieved as 83% at 0.1 g/L KMnO₄ concentration. The pH of 7.48, 60 min reaction time, and 0.1 g/L KMnO₄ were accepted as optimum conditions.

As a result of the study, it can be concluded that KMnO₄ oxidation can be used as an advanced oxidation process to achieve high COD removal efficiencies in greywater treatment. However, the optimal dose of oxidant should be determined from an economical perspective. Further studies are required to better understand the effect of KMnO₄ oxidation on greywater treatment.

Declaration

The authors declared no potential conflicts of interest to the research, authorship, and/or publication of this article. The authors also declared that this article is original and was prepared in accordance with international publication and research ethics, and ethical committee permission or any special permission is not required.

Author Contributions

Ö. Demir developed the methodology. E.S. Aktaş performed the analysis. Ö. Demir supervised and improved the study. Ö. Demir and E. S. Aktaş wrote the manuscript together.

Acknowledgement

The authors would like to thank the management and staff of the GAP Renewable Energy and Energy Efficiency Center Biomass laboratory of Harran University for their support.

References

1. Oron G, Adel M, Agmon V, et al., *Greywater use in Israel and worldwide: standards and prospects*. *Water Research*, 2014. **58**: p. 92-101.
2. Santos, C., Taveira-Pinto, F., Cheng, C. Y., and Leite, D., *Development Of An Experimental System For Greywater Reuse*. *Desalination*, 2012. **285**: p. 301-305.
3. Pinto, U., Maheshwari, B. L., And Grewal, H. S., *Effects of greywater irrigation on plant growth, water use and soil properties*. *resour. Conservation and Recycling*, 2010. **54**: p. 429-435.
4. Kipoğlu C., *Kişisel bakım ürünleri ve gri atıksu numunelerinin ozon ve fotokataliz ile arıtımı, toksitite incelenmesi*. 2014, MSc thesis, Namık Kemal University: Turkey. p. 92 (in Turkish).
5. Al-Jayyousi OR. *Greywater reuse: towards sustainable water management*. *Desalination*, 2003. **156**(1-3): p. 181-192.
6. Giresunlu E. *Characterization and Analysis Of Weak Urban Grey Water*. 2015. MSc thesis, Istanbul Technical University: Turkey. p. 183.
7. Anderson J. *The Environmental benefits of water recycling and reuse*. *Water Science and Technology: Water Supply*, 2003. **3**(4): p. 1-10.
8. Angelakis A.N, Bontoux L, Lazarova V. *Challenges and prospectives for water recycling and reuse in EU countries*. *Water Science and Technology: Water Supply*. 2003; **3**(4): p. 59-68.
9. Li F, Wichmann K, Otterpohl R. *Review of the technological approaches for grey water treatment and reuses*. *Science of the Total Environment*, 2009. **407**(11): p. 3439-3449.
10. Öztürk H. *Gri suların elektrokoagülasyon ile arıtılabilirliğinin incelenmesi*. 2017. MSc thesis, Gebze Technical University: Turkey. p. 77 (in Turkish).
11. Pidou M, Memon FA, Stephenson T, Jefferson B, Jeffery P. *Greywater Recycling: A Review*. *Engineering Sustainability*, 2007. **160**: p. 119-131.
12. Birben N.C., *Application of photocatalysis for the treatment of grey water*. 2012. MSc thesis, Bogazici University: Turkey. p. 117.
13. Barışçı S., *Electrochemical ferrate (Vi) production and research of its potential use for greywater treatment*. 2017. PhD thesis, Gebze Technical University: Turkey. p. 173.
14. Aslantürk A, Çetinkaya O. *Potasyum Permanganatın (K₂MnO₄) Lepistes (Poecilia Reticulata, Peters, 1859) Üzerine Akut Toksikitesi. Süleyman Demirel Üniversitesi Eğirdir Su Ürünleri Fakültesi Dergisi*, 2014. **10**(1): p. 12-12 (in Turkish).
15. Özer S.S.Y. and Karakuş C., *Sivas 4 Eylül Barajı İçme Suyundaki Manganın Laboratuvar ve Tesis Ölçekli Giderim Verimlerinin Karşılaştırılması. Selçuk Üniversitesi Mühendislik, Bilim ve Teknoloji Dergisi*, 2011. **26**(1): p. 1-9 (in Turkish).
16. Demir, Ö., *Potasyum permanganatın çamur dezentegrasyonu üzerine etkileri ve ultrasonik ön arıtımla geliştirilmesi*. Uludağ Üniversitesi Mühendislik Fakültesi Dergisi, 2016. **21**(2): p. 189-200 (in Turkish).
17. EPA Guidance Manual, *Alternative Disinfectants and Oxidants Guidance Manual: Chapter 5 Potassium Permanganate.*, April 1999. p.328.
18. APHA, *Standard Methods for the Examination of Water and Wastewater. 21st Edition, American Public Health*

Association/American Water Works Association/Water Environment Federation, Washington DC. 2005.

19. Blanco J, Torrades F, De M, García-Montaño J., *Fenton and Biological-Fenton Coupled Processes for Textile Wastewater Treatment and Reuse. Desalination*, 2012. **286**: p. 394-399.
20. Tony M.A, Parker H.L, Clark J.H., *Treatment of Laundrette Wastewater Using Starbon And Fenton's Reagent. Journal of Environmental Science and Health, Part A*, 2016. **51**(11): p. 974-979.
21. Thirugnanasambandham K., Sivakumar V., *Optimization of Treatment of Grey Wastewater Using Electro-Fenton Technique – Modeling and Validation. Process Saf Environ Prot*, 2015. **95**: p. 60-68.
22. Özgüroğlu G. *Gri Suyun Fenton Prosesi İle Arımı*. 2019. MSc thesis, Nevşehir Hacı Bektaş Veli University: Turkey. p. 49. (in Turkish).
23. Hassanshahi N., Karimi-Jashni A., *Ecotoxicology and Environmental Safety Comparison of Photo-Fenton, O₃/H₂O₂/ UV And Photocatalytic Processes For The Treatment Of Gray Water. Ecotoxicology and environmental safety*, 2018. **161**: p. 683-690.
24. Faggiano A., Ricciardi M., Fiorentino A., Cucciniello R., Motta O., Rizzo, L., Proto A. Combination of foam fractionation and photo-Fenton like processes for greywater treatment., *Separation and Purification Technology*, 2022. **293**: 121114.
25. Teodoro, A., Boncz, M. Á., Júnior, A. M., and Paulo, P. L. *Disinfection of greywater pre-treated by constructed wetlands using photo-Fenton: influence of pH on the decay of Pseudomonas aeruginosa. Journal of Environmental Chemical Engineering*, 2014. **2**(2): p. 958-962.



Research Article

Improved endothelial cell proliferation on laminin-derived peptide conjugated nanofibrous microtubes using custom made bioreactor

Günnur Onak Pulat ^a , Asena Gülenay Tatar ^b , Yusuf Hakan Usta ^c , and Ozan Karaman^{a*} 

^aBiomedical Engineering, İzmir Katip Çelebi University, Balatçık, Çiğli, İzmir, 35620, Turkey

^bMaterials Science and Nano Engineering, Sabanci University, Orhanlı, Tuzla, İstanbul, 34956, Turkey

^cFaculty of Biology, Medical and Health Sciences, The University of Manchester, M13 9PT, the United Kingdom

ARTICLE INFO

Article history:

Received 27 June 2022

Accepted 14 October 2022

Published 15 December 2022

Keywords:

Bioreactor

Electrospinning

Peptide

Tissue Engineering

Vascular graft

ABSTRACT

Cardiovascular diseases (CVD) are currently considered as one of the major reasons for death worldwide. The blockage of minor vessels such as the coronary arteries may be linked to more severe occurrences that might be fatal. The gold standard approach involves the transplantation of secondary vessels or the use of synthetic vascular grafts. Electrospun nanofiber (NF) based grafts produced with synthetic polymers might be simply modified to resemble the original structure of vessels providing desirable physical features and potentially improving cellular behavior including cell attachment, growth, and differentiation. Although poly lactic-co-glycolic acid (PLGA), is well-known, commercially available, degradable synthetic, has good mechanical and biocompatibility properties, PLGA is inadequate in terms of cell recognition signals. To overcome the bioactivity problem of PLGA, bioactive peptides are the most extensively utilized approach for surface modification. On the other hand, seeding and cultivation of tube-like conduits are challenging due to their shapes, and dynamic seeding and culture are considered beneficial for these grafts. Herein, we attempted to enhance the Endothelial Cells (ECs) attachment and proliferation on PLGA electrospun NF-based vascular grafts by both the conjugation of laminin-derived peptide IKVAV and perfusion culture with the custom-made bioreactor system. The bioreactor and its flow and pressure were simulated and decided using COMSOL Multiphysics 5.4. Human umbilical vein endothelial cell (HUVEC) adhesion and proliferation were increased by both functionalization of PLGA graft with IKVAV and using a custom-made perfusion bioreactor for cell seeding and cultivation within 7 days (d). This tubular vascular graft could be a potential tissue-engineered scaffold for the restoration of the venous system.

1. Introduction

Cardiovascular disease (CVD) is one of the most common reasons for mortality and disability in the world [1]. Surgical intervention using a bypass graft is a common method used to repair a damaged blood artery. Nevertheless, these vasculatures are generally inadequate in availability due to the condition of patients. Tissue-engineered grafts are an alternative to autografts due to their unlimited availability, a wide variety of material choices, and ability to be modified their properties to provide the mechanical features of natural vessels, their potential to outperform autografts in the future [2].

The use of biodegradable synthetic grafts, including poly(lactic acid), poly(glycolic acid) copolymer poly lactic-co-glycolic acid (PLGA), as a new generation of

higher efficiency vascular grafts with small diameter are being investigated [3]. Although PLGA has an adjustable degradation profile, it is easily molded into the required shape, and has good mechanical strength. Despite these benefits, scaffolds made of synthetic polymers are inadequate in terms of cell recognition signals. Surface functionalization may be required in some circumstances to increase cell adherence to the surface. Due to their efficiency in cell attachment, proliferation, adhesion, migration, growth, and differentiation, peptides are the most extensively utilized approach for surface modification [4]. The diversity of peptides aids applications to mimic the native tissues. One of the first appearing proteins of the extracellular matrix (ECM) during embryogenesis is laminin which is essential for embryo development and organogenesis; angiogenesis;

* Corresponding author. Tel.: +90 (232) 329-3535/3765; Fax: +90 (232) 325-3360

E-mail addresses: gunnur.onak@ikcu.edu.tr (G. Pulat), asenagulenayt@sabanciuniv.edu (A.G. Tatar), yusufhakan.usta@postgrad.manchester.ac.uk (Y.H. Usta), ozan.karaman@ikcu.edu.tr (O. Karaman)

ORCID: 0000-0003-0895-4768 (G.O. Pulat), 0000-0002-6841-2963 (A.G. Tatar), 0000-0003-2063-2905 (Y.H. Usta), 0000-0002-4175-4402 (O. Karaman)

DOI: [10.35860/iarej.1096616](https://doi.org/10.35860/iarej.1096616)

© 2022, The Author(s). This article is licensed under the CC BY-NC 4.0 International License (<https://creativecommons.org/licenses/by-nc/4.0/>).

cell adhesion, migration, and differentiation. The laminin-derived IKVAV peptide sequence induces capillary-like structures in endothelial cells (ECs) to encourage vascularization. It is also essential in promoting EC migration and proliferation [5].

Electrospinning is a versatile approach that allows you to quickly control the mechanical and biological features of nanofibers (NF) by changing the composition of a combination, which is not achievable with other scaffold manufacturing techniques [6]. Electrospun NF characteristics might be simply modified to imitate the natural vessel structure with desirable physical features including high porosity and a large surface area, potentially improving cellular behavior such as cell attachment, proliferation, and differentiation [7]. ECs cultivation on various electrospun NFs has previously been investigated and demonstrated the ability of the electrospinning technology to produce fibers that can be employed in natural and synthetic polymers that have been treated with various growth factors [8]. These studies show that it is possible to make a structure comparable to that of a native blood artery. PLGA electrospun NFs generally are insufficient due to their hydrophobic properties and lack of cell-recognition signals. To overcome this problem, Kim *et al.* covalently immobilized Gly-Arg-Gly-Asp-Tyr (GRGDY), a cell adhesive peptide, on PLGA and found that conjugation by surface-amine groups on PLGA NFs resulted in improved attachment of NIH 3T3 cells [9]. RGD peptide surface modification not only boosted cell adhesion but also resulted in increased proliferation.

Static and dynamic seeding and growth of cell-substrate constructs are available. A shaker, spinner flask, rotator, or perfusion device could be used for dynamic culture. Dynamic seeding and culture are considered beneficial for conduits and tube-like constructions in the literature [10, 11]. The perfusion system, on the other hand, better simulates the physiological state of blood vessels. Although there are some studies which modified electrospun NFs with peptides and showed the effect of dynamic culture and seeding on cell proliferation, separately, no study exists which demonstrated the effect of dynamic culture and seeding on ECs proliferation on IKVAV peptide conjugated electrospun PLGA tubular grafts. Herein, we attempted to improve the ECs attachment and proliferation on PLGA electrospun NF-based vascular grafts by both the conjugation of laminin-derived peptide IKVAV and perfusion culture with the custom-made bioreactor system. The effects of static and dynamic cell seeding and culturing of PLGA vascular grafts were compared on HUVEC (Human umbilical vein endothelial cell) attachment and proliferation. HUVEC attachment and proliferation were increased by both functionalization of PLGA graft with IKVAV and using custom-made perfusion bioreactor for cell seeding and cultivation. This tubular vascular graft could be a potential tissue-engineered scaffold for the regeneration of the venous system.

2. Materials and Methods

2.1 Peptide Synthesis

All chemical agents utilized to synthesize the peptide were obtained from AAPPTeC (Louisville, KY, USA). The peptide of isoleucine-lysine-valine-alanine-valine (IKVAV) was synthesized on 4-methylbenzhydrylamine (MBHA) resin (0.67 mmol/g loading capacity) [12]. The resin was added to DMF (Dimethylformamide) and swelled for 30 minutes. and rinsed with DMF two times. Then, Fmoc-protected amino acids (2 equiv.), diisopropylethylamine (DIEA; 4 equivalents), hydroxybenzotriazole (HOBt; 2 equivalents), and O-Benzotriazole-N,N,N',N'-tetramethyluronium-hexafluoro-phosphate (HBTU; 2 equivalents) added into DMF and mixed for 6 h on an orbital shaker [13]. The incidence of unreacted amine groups was tested by Ninhydrin test which is applied to the resin solution [12]. If the positive result was obtained, the resin solution was rinsed with DMF and amino acid was coupled until the result of the Kaiser test was negative. If the result is negative, the resin was rinsed with DMF (3x3ml). Then, deprotection solution was added into resin solution for the elimination of Fmoc protecting groups. After that, Kaiser Test was applied again to check that Fmoc groups were detached. When a negative result was obtained, the deprotection step was applied again until obtaining a positive result. Finally, the resin solution was rinsed with DMF and filtered. The same procedure was applied until the targeted peptide sequence was obtained. By adding 95% trifluoroacetic acid (TFA), 2.5% distilled water and 2.5% triisopropylsilane (TIPS), the peptide was cleaved from the resin and thrown into cold-diethyl ether [14]. The solution was centrifuged at 4500 rpm and the supernatant was removed [15]. Then, the peptide was obtained after freeze-drying of pellet.

2.2 Fabrication of PLGA Vascular Grafts

The 3 wt % PLGA (85:15; PURASORB PDLG 8531; Corbion Biomaterials, the Netherlands) containing electrospinning solution was prepared in 1,1,1,3,3,3-Hexafluoro-2-propanol (HFIP; Matrix Scientific; Columbia) [16]. The solution was transferred into a syringe and the syringe was placed on the syringe pump. The needle was linked to a positively charged electrode of a high voltage source. Nanofibers were ejected with 20 kV electrical potential and 1 ml/h injection rate. The ejected PLGA nanofibers were collected by a special collector designed by our group in 3 mm inner diameter to produce microtubular structures [17]. PLGA nanofiber sheets were also produced by using an aluminum rotating wheel covered with circular glass coverslips with 20 kV electrical potential, 1 ml/h injection rate, and 1200 RPM rotation speed parameters.

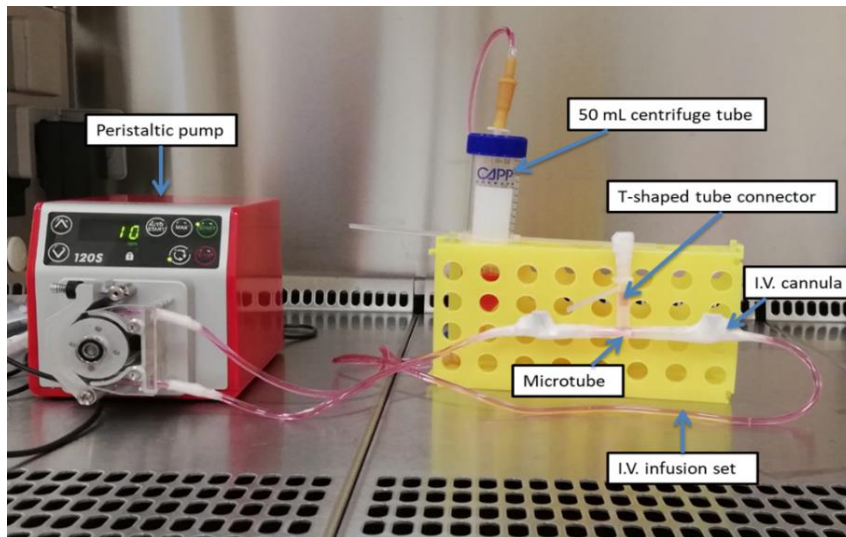


Figure 1. Perfusion Based Bioreactor System

2.3 Scanning Electron Microscopy

Scanning electron microscope (SEM; Carl Zeiss Microscopy, Germany) technique was performed for characterization of PLGA nanofibers by using with 3 kV accelerating voltage to determine the NF morphology and the wall thickness and diameter of the microtubes. The samples were coated with gold (QUORUM; Q150 RES; East Sussex; United Kingdom) at 20 mA for 60 sec and then, characterization was started [12]. The scale bars of images were measured by the software of SEM.

2.4 Peptide Conjugation of Nanofibers

Fabricated NFs were washed with deionized water. Then, they immersed in 0.1M MES (2-Morpholinoethanesulfonic acid buffer) solution with 2 mM EDC and 5 mM NHS to obtain a carboxyl-rich surface for 45 minutes at 37°C. Then, the NFs were reacted with 1 mM peptide in PBS 24 hours at 4°C.

2.5 Bioreactor Design and Simulation

Dynamic cell culture was performed using a bioreactor system developed by our group as shown in Figure 1. Microtube nanofibers were placed inside the bioreactor. All parameters were determined using COMSOL simulation, which is bioreactor flow and pressure. The system was started with a 10 RPM speed, which is approximately 4 ml/min flow rate. The custom-made bioreactor used in dynamic cell-culture was simulated COMSOL Multiphysics Simulation 5.4 to find essential parameters in terms of velocity and pressure. Table 1 summarized the input and calculated parameters for simulating the custom-made bioreactor in which the scaffold was placed.

2.6 Static and Dynamic Cell Culture

HUVECs (kindly donated from Ege University Research Group of Animal Cell Culture and Tissue Engineering Laboratory) were cultured with F12 DMEM

(Dulbecco's Modified Eagle Medium) containing 100 U/ml penicillin, 100 mg/ml streptomycin, and 10% Fetal Bovine Serum (FBS) and incubated in 5% CO₂ at 37 °C [18]. The scaffolds were sterilized with UV radiation. HUVECs (5×10^6 cells/cm²) were seeded on the planer NFs and the lumen of the microtubular nanofibers. The seeding volume and the seeding area were optimized as 150 μ l and 20 mm². The cell concentration was calculated as 6.6×10^6 cells/ml. For static seeding, 150 μ l cell suspension (6.6×10^6 cells/ml) were inserted in the lumen and incubated for 1.5 hours. Then, the microtube was placed in the bioreactor system and the culture media was perfused for 7 days. For the dynamic seeding, the microtube was placed in a bioreactor and 10 ml cell suspension (6.6×10^6 cells/ml) was perfused for 1.5 hours. Then, the basal media was inserted into the bioreactor system and cultivated for 7 days. For the static culture, the planer NFs and microtubes were inserted in the cell culture medium and statically cultured. For dynamic seeding, the cell culture media was perfused in the bioreactor system after the microtube was placed in the system. For each experimental group, the growth medium was replaced every three days.

2.7 Cell Proliferation Analysis

MTT assay ((Vybrant, Invitrogen, Grand Island, NY) was applied to both nanofiber sheets and microtubes on 1 d, 4 d, and 7 d to assess cell proliferation. 10% MTT solution was prepared with bare F12 DMEM and incubated with the cell-cultured nanofibers for two hours. Then, the MTT solution was replaced with DMSO (Sigma Aldrich, St. Louis, MO, USA) and formazan crystals was dissolved after 5 minutes. Finally, the incubated DMSO was transferred into a 48-well plate to measure optical densities. The optical densities were calculated by measuring at 570 nm with Synergy™ HTX Multi-Mode Microplate Reader (BioTek, Epoch 2). The obtained absorbance values were related with cell numbers based on a calibration curve.

Table 1. Input and calculated parameters for the custom-made bioreactor conditions using COMSOL

Input parameters		Calculated parameters	
Scaffold size		Scaffold geometry and strain	
Scaffold diameter (cm)	5	Scaffold area (mm ²)	19.63
Scaffold height (cm)	12	Tortuosity	1.05
Scaffold porosity/pore size		Equiv. particle diam. (micron)	13.04
Porosity (%)	92	Compression time (sec)	0.50
Pore diameter (micron)	100	Flow-related parameters	
Compression parameters		Reynold's number	1.10E-01
Compression frequency (Hz)	1	Scaffold permeability (m ²)	1.38E-10
Applied compression strain (%)	5	Brinkman constant	1.27E+00
Other parameters		Perfusion pore fluid velocity (mm/sec)	0.92
Bioreactor perfusion rate (ml/min)	1	Compression pore fluid velocity (mm/sec)	1.30
Medium density (gr/ltr, typical 1000)	1	Total pore fluid velocity (mm/sec)	2.23
Medium viscosity (mPas, typical 0.7)	0.8	Volumetric flow due to compression	
Bioreactor perfusion rates		Flow (mm ³ /sec)	2.36E+01
Typical low value (ml/min)	0.1	Flow (ml/min)	1.41
typical high value (ml/min)	1	Wall shear stress due to flow	
Culture medium density and viscosity		Shear stress from perfusion (Pa)	0.080
Density (gr/ltr)	1000	Shear stress from compression (Pa)	0.113
Viscosity (mPas)	0.7	Total shear stress (Pa)	0.193

2.8 Cell Morphology Analysis

Actin filaments and cell nuclei were dyed with phalloidin and DAPI (Merck Millipore, Actin Cytoskeleton and Focal Adhesion Staining Kit, Catalog No. FAK100), respectively, in accordance with manufacturer's instructions for the purpose of observing cell morphology on planar NFs [19]. First, cell-seeded NFs were washed twice in PBS before being fixed at 4 °C for 20 minutes with 4% paraformaldehyde (Sigma Aldrich, St. Louis, MO, USA). After that, samples were permeabilized for 5 minutes with 0.1% Triton X-100 in PBS and blocked for 30 minutes with 1.5% bovine serum albumin (BSA) in PBS. Then, samples were incubated with DAPI for 5 minutes and phalloidin in PBS for 1 hour at 4 °C [12]. To examine cell morphology, images of the stained samples were captured using an inverted fluorescence microscope.

2.9 Statistical Analysis

We performed the experiments with at least three repetitions. All the obtained data were statistically analyzed with two-way analysis of variance (ANOVA) (SPSS 12.0, SPSS GmbH, Germany) and the Student-Newman-Keuls method as a post hoc test. Significant differences among groups were defined at p values at least less than 0.05. (*p<0.05, **p<0.01, ***p<0.001) [20].

3. Results and Discussion

The tubular vascular graft was successfully produced and SEM imaging was used to investigate the morphology of the PLGA nanofibers and determine the diameter and wall thickness of the microtubes (Figure 2). The inner

diameter of the tubular graft was measured as 2.5 ± 0.2 mm and the thickness of the wall is 370 ± 20 nm. Since the grafts were produced by custom-made collector, the graft in various diameters might be also produced with the electrospinning setup. Integrating different scaffold fabrication methods with the development of vascular scaffolds might offer a patient-specific grafts [20]. Therefore, our strategy which allows fabricated patient-specific vascular grafts in different diameters might be used for clinical applications.

COMSOL Multiphysics was assessed to improve the quality of the custom-made bioreactor. The designed scaffold, velocity, and pressure parameter of the bioreactor were simulated and the results are shown in Table 2. Permeability and Brinkman number were estimated based on porosity and equivalent particle diameter.

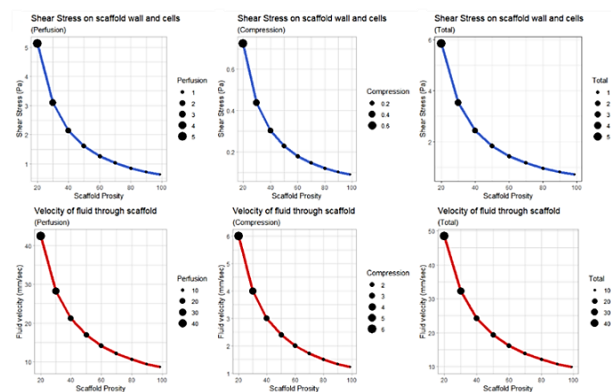


Figure 2. SEM image of PLGA vascular graft microtube produced by electrospinning with A) Higher magnification B) Lower magnification. Scale bar represents 100µm

Table 2. The simulation result of the scaffold and the custom-made bioreactor using COMSOL

Porosity (%)	Particle Diameter (μm)	Permeability (m^2)	Fluid velocity (mm/sec)				Shear stress (Pa)		
			Brinkman	Perfusion	Compression	Total	Perfusion	Compression	Total
20	600	3E-11	0.944876592	4.244132	6	10.24413	0.585724	0.828048	1.413773
30	350	4.5E-11	1.050277406	2.829421	4	6.829421	0.354393	0.501012	0.855405
40	225	6E-11	1.116333336	2.122066	3	5.122066	0.244662	0.345883	0.590546
50	150	7.5E-11	1.167020032	1.697653	2.4	4.097653	0.183015	0.258731	0.441746
60	100	9E-11	1.206426184	1.414711	2	3.414711	0.143925	0.20347	0.347395
70	64.28571	1.05E-10	1.236111092	1.212609	1.714286	2.926895	0.117024	0.165438	0.282462
80	37.5	1.2E-10	1.256873227	1.061033	1.5	2.561033	0.097391	0.137684	0.235075
90	16.66667	1.35E-10	1.269167702	0.94314	1.333333	2.276474	0.082417	0.116515	0.198932
99	1.515152	1.485E-10	1.273198891	0.8574	1.212121	2.069522	0.071665	0.101314	0.172979

The fluid velocity (mm/s) and shear stress (Pa) resulting from perfusion and compression were calculated. The graph for shear stress and velocity on scaffold wall and cell due to perfusion and compression and the total were drawn according to the parameter used in our experiment and illustrated in Figure 3. The velocity and pressure simulation result of the bioreactor in which the scaffold was placed was demonstrated in Figure 4. As a result, the simulation findings and the proposed model are condired as accurate and suitable for predicting system behavior. Validating the results with experimental data will indirectly establish the velocity and pressure as a hydrodynamic model. It is observed that there is a direct relationship between the velocity and pressure of the bioreactor and scaffold porosity. Increasing porosity of scaffold causes a decrease in total shear stress and fluid velocity.

Cell proliferation on PLGA NFs produced on glass slides after static seeding-static culture (SS-SC) and vascular grafts after static seeding-static culture (SS-SC), static seeding-dynamic culture (SC-DC), dynamic seeding-dynamic culture (DS-DC) was evaluated by MTT assay in at 1, 4, and 7 d (Figure 5). According to MTT analysis, IKVAV conjugated PLGA NFs enhanced the cell proliferation for 7d in all experimental groups. Moreover, the seeding and cultivation techniques by using perfusion-based bioreactor were developed for optimization for efficient coating of HUVECs on grafts. The proliferation was improved by dynamic seeding compared with static seeding, while dynamic culture helped to obtain better proliferation results compared to static culture. Similarly, the rotating EC seeding used in various research for many 3-D cell-material designs has favored dynamic culture [10, 21]. Çelebi-Saltık *et al.* coated polyurethane NFs with fibronectin and heparin and added NFs between media layers and the tunica intima to mechanically strengthen the grafts [22]. They cultured HUVECs on the graft using the cell sheet engineering approach with a designed bioreactor system and demonstrated that the dynamic culture system preserved the vascular graft, aided in the differentiation of primary human hematopoietic cells into thrombocytes, and exhibited anti-thrombogenic properties.

Herein, the use of the tubular vascular graft as a scaffold resulted in lower cell attachment and proliferation on a glass slide at the end of 7d compared to the planar NF scaffold. The 2D planar surface of a flat scaffold is ideal for seeding and optimal EC adhesion [23]. However, 2D planar surfaces cannot fully mimic vascular structures. Therefore, creating scaffolds that can change their morphology from 2D planar structures to 3D tubular shapes, providing 3D endothelialization may be beneficial in the design of vascular grafts. However, the cultivation of ECs on 3D tubular grafts by bioreactors may be a practical technique to facilitate 3D endothelialization. Here, we improved the proliferation of HUVECs on tubular graft with the help of dynamic seeding and dynamic culture.

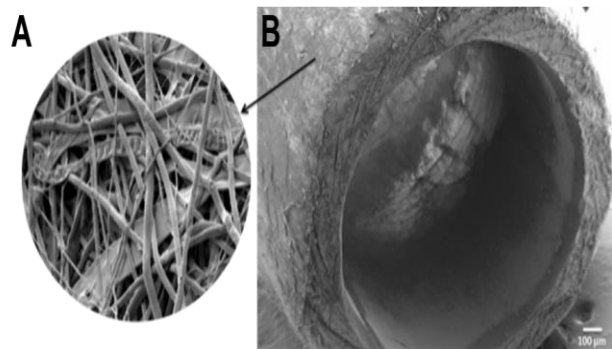


Figure 3. Quantitative results of scaffold and flow rate of the custom-made bioreactor using COMSOL Multiphysics

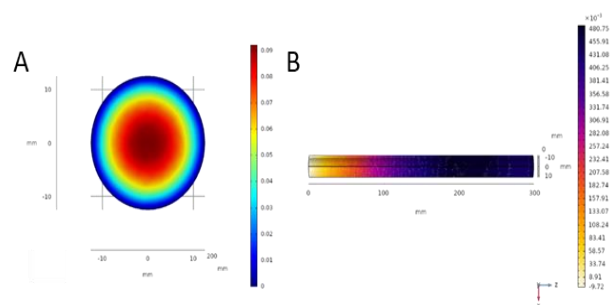


Figure 4. (A) Velocity simulation (B) Pressure simulation result of the bioreactor in which scaffold was placed using COMSOL

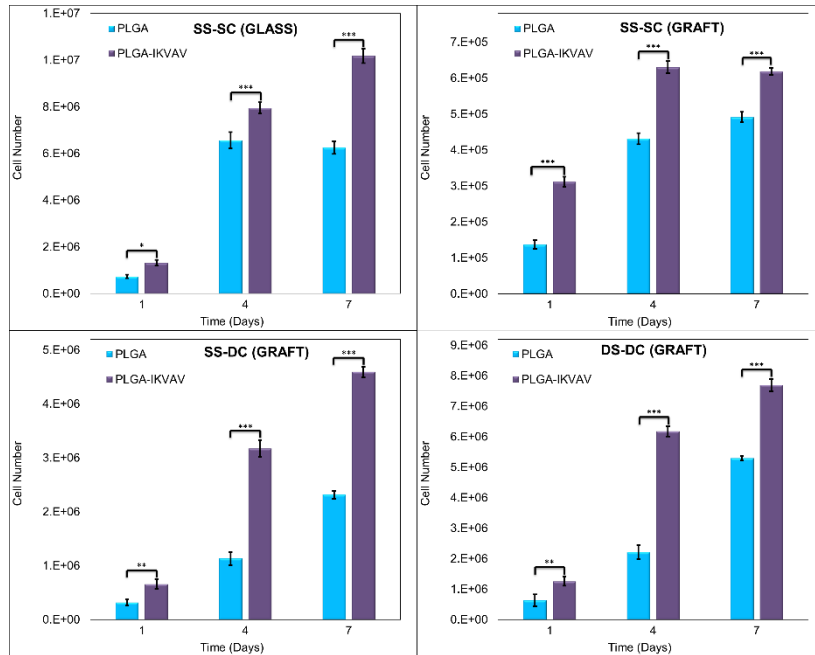


Figure 5. Cell number in vascular grafts after incubation in cell culture medium for 7 days (SS=Static Seeding, SC=Static Culture, DS=Dynamic Seeding, DC=Dynamic Culture)

The morphology HUVECs were observed after DAPI and phalloidin staining on 2D planar PLGA and IKVAV conjugated PLGA NF groups (Figure 6). A difference in the cell morphology between the groups was noticed from the images. HUVECs showed spread morphology on the PLGA-IKVAV surface, while scattered morphology was observed on PLGA. Moreover, completely elongated cell morphology was observed on PLGA-IKVAV surfaces. A higher number of nuclei per image in PLGA-IKVAV supports the MTT proliferation assay. IKVAV, a peptide derived from laminin's α -chain, has previously been shown to improve endothelial cell adhesion and tubule formation [24]. Grant *et al.* found that the IKVAV peptide enhanced EC organization, formation of the branched capillary vessel as a result of mouse angiogenesis assay as well as trials with the chick yolk sac/chorioallantois membrane [25]. Vascular ECs enhanced cell migration, attachment, and capillary network development by immobilization of IKVAV on collagen type I hydrogels [5]. IKVAV has also been demonstrated to facilitate ischemic tissue revascularization, making it of significant interest to those attempting to create microvascular networks [26].

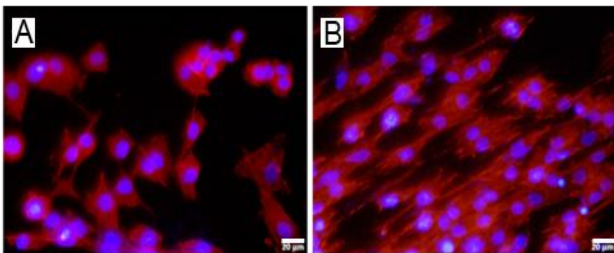


Figure 6. Morphology of human umbilical vein endothelial cell (HUVEC) on 2D planar (A) PLGA (B) IKVAV conjugated PLGA nanofiber. (Cell nuclei and cytoskeletal actin are stained with 4,6-diamidino-2-phenylindole (DAPI; blue) and phalloidin (red) (Scale bar represents 20 μ m)

4. Conclusions

Herein, we effectively exhibited improved attachment and proliferation of HUVECs on IKVAV modified PLGA tubular grafts and cultivated in a custom-made dynamic bioreactor system. The custom-made bioreactor system has been designed in such a way that any laboratory can easily install it with low-cost supplies as an alternative to expensive commercially available bioreactors. Furthermore, the design of electrospinning collector for vascular grafts is promising for the researchers to produce polymer-based electrospun grafts with different diameters. Moreover, various peptide molecules might be used to functionalize these grafts according to desired properties. This technology provides a successful technique for increasing pre-endothelialization by seeding small-diameter vascular grafts with ECs, which may dramatically reduce problems in clinical applications. Further improvement and development of this system may result in a commercially available clinical solution to improve implanted tissue-engineered vascular grafts patency.

Declaration

The author(s) declared no potential conflicts of interest with respect to the research, authorship, and/or publication of this article. The author(s) also declared that this article is original, was prepared in accordance with international publication and research ethics, and ethical committee permission or any special permission is not required.

Author Contributions

O. Karaman developed the methodology. G.O. Pulat and A.G. Tatar performed experiments. Y.H. Usta

performed the simulations. O. Karaman supervised and improved the study. All authors wrote the manuscript together.

Acknowledgment

This work supported by TÜBİTAK (The Scientific and Technological Research Council of Turkey) under 2209-A University Students Research Projects Support Program, TURKEY.

References

- Levenson, J.W., P.J. Skerrett, and J.M. Gaziano, *Reducing the global burden of cardiovascular disease: the role of risk factors*. Prev Cardiol, 2002. **5**(4): p. 188-99.
- Obiweluozor, F.O., et al., *Considerations in the Development of Small-Diameter Vascular Graft as an Alternative for Bypass and Reconstructive Surgeries: A Review*. Cardiovascular Engineering and Technology, 2020. **11**(5): p. 495-521.
- Mikos, A.G. and J.S. Temenoff, *Formation of Highly Porous Biodegradable Scaffolds for Tissue Engineering*. Electronic Journal of Biotechnology, 2000. **3**(2): p. 23-24.
- Tallawi, M., et al., *Strategies for the Chemical and Biological Functionalization of Scaffolds for Cardiac Tissue Engineering: a Review*. Journal of the Royal Society, Interface, 2015. **12**(108): p. 20150254-20150254.
- Nakamura, M., et al., *Construction of multi-functional extracellular matrix proteins that promote tube formation of endothelial cells*. Biomaterials, 2008. **29**(20): p. 2977-2986.
- Agarwal, S., J.H. Wendorff, and A. Greiner, *Use of electrospinning technique for biomedical applications*. Polymer, 2008. **49**(26): p. 5603-5621.
- Karkan, S.F., et al., *Electrospun nanofibers for the fabrication of engineered vascular grafts*. Journal of Biological Engineering, 2019. **13**(1): p. 83.
- Ku, S.H. and C.B. Park, *Human endothelial cell growth on mussel-inspired nanofiber scaffold for vascular tissue engineering*. Biomaterials, 2010. **31**(36): p. 9431-9437.
- Kim, T.G. and T.G. Park, *Biomimicking extracellular matrix: cell adhesive RGD peptide modified electrospun poly (D, L-lactic-co-glycolic acid) nanofiber mesh*. Tissue engineering, 2006. **12**(2): p. 221-233.
- Nasseri, B.A., et al., *Dynamic rotational seeding and cell culture system for vascular tube formation*. Tissue engineering, 2003. **9**(2): p. 291-299.
- Hsu, S.-h., et al., *The effect of dynamic culture conditions on endothelial cell seeding and retention on small diameter polyurethane vascular grafts*. Medical Engineering & Physics, 2005. **27**(3): p. 267-272.
- Onak, G., U.K. Ercan, and O. Karaman, *Antibacterial activity of antimicrobial peptide-conjugated nanofibrous membranes*. Biomedical Materials, 2020. **16**(1): p. 015020.
- Zhao, Q., et al., *Programmed Shape-Morphing Scaffolds Enabling Facile 3D Endothelialization*. Advanced Functional Materials, 2018. **28**: p. 1801027.
- Hamsici, S., et al., *Bioactive peptide functionalized aligned cyclodextrin nanofibers for neurite outgrowth*. Journal of Materials Chemistry B, 2017. **5**(3): p. 517-524.
- Dicker, K.T., et al., *Spatial Patterning of Molecular Cues and Vascular Cells in Fully Integrated Hydrogel Channels via Interfacial Bioorthogonal Cross-Linking*. ACS Applied Materials & Interfaces, 2019. **11**(18): p. 16402-16411.
- Onak, G. and O. Karaman, *Accelerated mineralization on nanofibers via non-thermal atmospheric plasma assisted glutamic acid templated peptide conjugation*. Regen. Biomater., 2019. **6**(4): p. 231-240.
- Usta, Y.H., et al. *Design of electrospinning collector for vascular tissue engineering applications*. in *2017 Medical Technologies National Congress (TIPTEKNO)*. 2017.
- Onak Pulat, G., et al., *Role of functionalized self-assembled peptide hydrogels in in vitro vasculogenesis*. Soft Matter, 2021. **17**(27): p. 6616-6626.
- Onak, G., et al., *Aspartic and Glutamic Acid Templated Peptides Conjugation on Plasma Modified Nanofibers for Osteogenic Differentiation of Human Mesenchymal Stem Cells: A Comparative Study*. Scientific Reports, 2018. **8**(1): p. 17620.
- Best, C., et al., *Toward a patient-specific tissue engineered vascular graft*. Journal of tissue engineering, 2018. **9**: p. 2041731418764709-2041731418764709.
- Kent, K.C., et al., *An in vitro model for human endothelial cell seeding of a small diameter vascular graft*. ASAIO transactions, 1988. **34**(3): p. 578-580.
- Çelebi-Saltik, B., M.Ö. Öteyaka, and B. Gökçinar-Yagci, *Stem cell-based small-diameter vascular grafts in dynamic culture*. Connective Tissue Research, 2021. **62**(2): p. 151-163.
- Zhao, Q., et al., *Programmed Shape-Morphing Scaffolds Enabling Facile 3D Endothelialization*. Advanced Functional Materials, 2018. **28**(29): p. 1801027.
- Ali, S., et al., *Immobilization of Cell-Adhesive Laminin Peptides in Degradable PEGDA Hydrogels Influences Endothelial Cell Tubulogenesis*. BioResearch open access, 2013. **2**(4): p. 241-249.
- Grant, D.S., et al., *Interaction of endothelial cells with a laminin A chain peptide (SIKVAV) in vitro and induction of angiogenic behavior in vivo*. J Cell Physiol, 1992. **153**(3): p. 614-25.
- Grant, D.S. and Z. Zukowska, *Revascularization of ischemic tissues with SIKVAV and neuropeptide Y (NPY)*. Angiogenesis, 2000: p. 139-154.